Study of thin metal films and oxide materials for nanoelectronics applications

Luis De Los Santos Valladares

Clare Hall

University of Cambridge

A thesis submitted at the Cavendish Laboratory for the degree of

Doctor of Philosophy

2011

To my beloved sisters
Milagros Esther and Rosa Iris.

Declaration

This dissertation is the result of my own work, unless otherwise stated, includes nothing which is the outcome of work done in collaboration. No part of this thesis has already, or is being concurrently submitted for any other qualification than the degree of Doctor of Philosophy at the University of Cambridge. This Thesis does not exceed the limit of length prescribed in the Special Regulations of the PhD thesis (60,000 words in length, including tables, footnotes, bibliography and appendices) for which I am a candidate. The length of this Thesis is approximately 45,000 words.

Acknowledgements

I am deeply grateful to my supervisor Crispin H.W. Barnes for his suggestions and discussions during my PhD studies. Also, I would like to acknowledge the deceased Prof. Tony Bland for his guidance and help during the initial states of my PhD studies.

I am thankful to the following organizations for financial support during the years of my PhD: The European Union Program ALBAN (Scholarship No. E06D101257PE), the Cambridge Overseas Trust, and the Japan Society for the Promotion of Science JSPS (Grant No. PE10027).

There are many people from the University of Cambridge who I need to thank very much. Firstly, to Dr. Luis Benito, who provided me with helpful guidance and training in photolithography. Our chats made the hard work joyful. To all the members of the Thin Film Magnetism, TFM group. To Dr. Thanos Mitrelias for suggesting many ideas during the realization of this thesis, to Drs. Adrian Ionescu, Justin Palfreyman, Justin Llandro and Thomas Hayward for their advice and help. To the secretary Mrs. Alicia Kelleher for her help with documentation. I have made many good friends in the TFM group, the most talkative people are Drs. Christoforos Moutafis, David Kupper, Hidekazu Kurebayachi, Klaus Peter Kopper and my office mates Chen Shen and Shin Liang. Furthermore, I thank my friends Drs. Robert Midgley Reeve and Joshaniel Cooper for their friendship and correcting my English. Moreover, to the ex-member of the group, now in the Nanyang Technological University of Singapore, Dr. Dongwook Lee and his wife Dr. Jiwon Seo for training me with Graphite oxide preparation and Synchrotron radiation analysis and, most important, for their friendship.

I must say thank you to the people from my College, Clare Hall. To the administrative team, specially to the Senior Tutor Bobie Wells and to the secretary Irene Hills who always were kind to help me and to ensure a nice stay in Cambridge for me. To my friends Adbu Zhogbi, Samir Rihani, Vanessa Loo, Evianne van Gijn, Phivi Antoniou, Livia Faim and all my friends from Clare Hall.

During the last year of my PhD studies, I spent many months in the Tokyo Insitute of Technology. I thank Prof. Yutaka Majima and his research team for providing me additional information and training for that period. It was also a good opportunity to learn about the Japanese culture and to make new friends: Azuma Sensei, Okabayashi Sensei, Muraki kun, Victor kun, Kano kun, Ogawa kun and all the members of the Majima group for their help and friendship. Furthermore, I want to thank my friend Dr. Seichi Suzuki from the Hitachi company for indroducing me the Japanese culture.

Finally I want to thank all my friends from Peru for their encouraging chats and emails, especially to Prof. Angel Bustamante Dominguez (University of San Marcos) for his collaboration.

Last but not least, thank you to all my relatives who always were alert at any news relating to my studies. To my aunt Olga and her husband Omar, my cousins Chino, Manito, Jose and my sisters Rosa Iris and Milagros Esther to whom this thesis is dedicated. All my love to them.

List of publications

1. *Luis De Los Santos V.*, Angel Bustamante D., Robert M. Reeve, T. Mitrelias, Richard M. Langford, Yasuo Azuma, Crispin H. W. Barnes and Yutaka Majima "Reorientation response of magnetic microspheres attached to gold electrodes under an applied magnetic field", Submitted 2011.
2. Daniel Hurtado S., *Luis De Los Santos V.*, Angel Bustamante D., Dwight Acosta N, Saiful Khondaker, Thanos Mitrelias, Crispin H. W. Barnes and Yutaka Majima "Crystallization and electrical resistivity of Cu_2O and CuO obtained by thermal oxidation of Cu thin films on SiO_2/Si substrates", Submitted 2011.
3. A. Bustamante Dominguez, *Luis De Los Santos V.*, J. Flores, Crispin H. W. Barnes and Yutaka Majima "Aging effect in CaLa $Ba[Cu_{1-x}Fe_x]_3O_{7-\delta}$ with $0 \leq x \leq 0.07$ studied by Mössbauer spectroscopy", Hyperfine Interactions 2011, DOI 10.1007/s10751-011-0371-z.
4. L. Leon Felix, A. Bustamante Dominguez, A. Osorio Anaya, G.S. Olarte, *Luis De Los Santos V.*, Crispin H. W. Barnes and Yutaka Majima "Synthesis and characterization of hollow α-Fe_2O_3 sub-micron spheres prepared by sol-gel ", Hyperfine Interactions 2011, DOI 10.1007/s10751-011-0353-1.
5. *Luis De Los Santos V.*, Lizbet Leon F., Angel Bustamante D., Thanos Mitrelias, Francois Sfigakis, Saiful I. Khondaker, Crispin H. W. Barnes and Yutaka Majima "Controlled electroplating and electromigration in nickel electrodes for nanogap formation", Nanotechnology 21 (2010) 445304.

6. *Luis De Los Santos V.*, Angel Bustamante D., Justin Llandro, Seiichi Suzuki, Thanos Mitrelias, Richard Bellido Q., Crispin H.W. Barnes and Yutaka Majima "Attaching thiolated superconductor grains on gold surfaces for nanoelectronics application", Japanese Journal of Applied Physics 49 (2010) 093102.
7. Dongwook Lee, *Luis De Los Santos V.*, Jiwon Seo, Lizbet Leon Felix, Angel Bustamante D. and C. H. W. Barnes, "The structure of graphite oxide: Investigation of its surface chemical groups", Journal of Physical Chemistry B 114 (2010) 5723-5728.
8. *Luis De Los Santos V.*, Angel Bustamante D., Lizbet Leon F., Thanos Mitrelias, Adrian Ionescu, Justiniano Quispe M., Crispin Barnes, "Crystallization and morphology of gold thin films on unpolished Si(100) substrates after furnace and flame annealing", Journal of Materials Science and Engineering ISSN1934-8959, Vol 4, No 1 (2010) 1-10.
9. *Luis De Los Santos V.*, Angel Bustamante D., Juan Gonzalez G., Juan Feijoo L., Ana Osorio A., Thanos Mitrelias, Yutaka Majima and Crispin H.W. Barnes, "Magnetic properties of the superconductor $CaLaBaCu_3O_7$", Open Superconductors Journal 2 (2010) 19-27.
10. *Luis De Los Santos V.*, Dongwook Lee, Jiwon Seo, Lizbet Leon F., Angel Bustamante D., Seiichi Suzuki, Yutaka Majima, Thanos Mitrelias, Adrian Ionescu and Crispin H.W. Barnes, "Crystallization and surface morphology of Au/SiO_2 thin films following furnace and flame annealing", Surface Science 603 (2009) 2978-2985.
11. Dongwook Lee, Jiwon Seo, G.R. Jelbert, *Luis De Los Santos V.*, J.M. Cole, Christos Panagopoulos, Crispin H. W. Barnes, "Transparent and flexible polymerized graphite oxide thin film with frequency-dependent dielectric constant", Applied Physics Letters 95 (2009) 172901.

12. *Luis De Los Santos V.* et. al, “Magnetic measurements of suspended functionalised ferromagnetic beads under DC applied fields”, Journal of Magnetism and Magnetic Materials 321 (2009) 2129-2134.

13. *Luis De Los Santos V.*, Angel Bustamante D., Juan C. Gonzalez G., Jess Flores S., Xavier Obradors, “Superconductivity in the System $\mathrm{CaLaBaCu}_{3-x}$ $(PO_4)_x O_{7-d}$ with X=0.1, 0.3, 0.5”, Journal of Physics and Chemistry of Solids 67 (2006) 605-609.

14. Angel Bustamante D.,*Luis De Los Santos V.*, Bram L. Willems, Vctor H. Barinotto C., Juan C. Gonzlez G, Xavier Obradors, “Superconductivity in the System $[\mathrm{Y}_{0.8}\mathrm{Ca}_{0.2}](\mathrm{SrBa})\mathrm{Cu}_{3-x}(\mathrm{BO}_3)_x\mathrm{O}_{7-\delta}$ with $0.1 \leq X \leq 0.5$”, Journal of Physics and Chemistry of Solids 67 (2006) 594-596.

15. Angel Bustamante D., Ana M. Osorio A., *Luis De Los Santos V.*, Hilda Carhuancho A., J.C. Gonzlez G., Geraldo Cenicchiario and Juan Augusto Feijoo L. “Synthesis of $\mathrm{YBa}_2\mathrm{Cu}_3\mathrm{O}_{7-\delta}$ using oxalate precursor and sol-gel method”, Advances in Science and Technology 47 (2006) 37-42.

16. *Luis De Los Santos V.*, D. Angel Bustamante, S. Jesus Flores, G Juan C. Gonzalez, “Preparation and characterization of the superconductor $\mathrm{CaLaBaCu}_{2.8}(\mathrm{PO}_4)_{0.2}\mathrm{O}_{6.2}$ Compound”, Physica C 408-410 (2004) 44-45.

17. Angel Bustamante D., Richard Bellido Q., *Luis De Los Santos V.*, J. C. Gonzlez, “Preparation and characterization of the superconductor $\mathrm{CaLaBaCu}_{2.8}(\mathrm{BO}_3)_{0.2}\mathrm{O}_{6.4}$ Compound”, Physica C 408-410 (2004) 884-885.

18. Victor H. Barinotto C., Bram L. Willems, Angel Bustamante D., *Luis De Los Santos V.*, Juan Gonzlez G. “Preparation and characterization of the superconductor $[\mathrm{Y}_{0.8}\mathrm{Ca}_{0.2}]\mathrm{SrBaCu}_{2.8}(\mathrm{BO}_3)_{0.2}\mathrm{O}_{6.4}$ compound”, Physica C 408-410 (2004) 58-59.

Abstract

Different types of thin metal films and oxide materials are studied for their potential application in nanoelectronics: gold and copper films, nickel nanoelectrodes, oxide nanograin superconductors, carboxyl ferromagnetic microspheres and graphene oxide flakes. The crystallization and surface morphology of gold and copper films on SiO_2/Si substrates is investigated as a function of annealing temperature. Annealing arranges the Au crystallites in the [111] direction and changes the morphology of the surface. Relaxation of the Au layer at high temperatures is responsible for the initial stages of cluster formation. These may form at disordered points on the surface and become islands when the temperature is increased. In the case of Cu/SiO_2/Si films, oxides are formed after thermal oxidation at different temperatures up to 1000 °C. The phase evolution $Cu \rightarrow Cu + Cu_2O \rightarrow Cu_2O \rightarrow Cu_2O + CuO \rightarrow CuO$ is detected. Pure Cu_2O films are obtained at 200 °C, whereas uniform CuO films without structural surface defects are obtained in the temperature range 300 - 550 °C. A resistivity phase diagram, which is obtained from the current-voltage response of the copper oxides, is presented. In the case of thin nickel films, the necessary reagents, conditions and processes required to obtain nano and atomic gaps between soft and clean nickel electrodes are described by using a conventional electrochemical cell. Current-voltage characteristics are also presented to evaluate possible applications of the nanogap electrodes in electronic nanodevices.

In addition to the metal surfaces, oxides materials such as the superconductor $LaCaBaCu_3O_7$ (La1113), carboxyl ferromagnetic microparticles and graphene oxide flakes are studied. La1113 is a high critical temperature superconductor with $\mathrm{T}_{C(onset)} = 80$ K and its structure is similar to the tetragonal YBCO. This thesis explores the attachment of La1113 nanograins on Au(111) surfaces through self-assembled monolayers of HS-C_8H_{16}-HS [octane (di)thiol] for their potential application in nanotransistors. It is found that La1113 particles (100 nm mean diameter) can be functionalized by octane (di)thiol without affecting their superconducting critical temperature ($\mathrm{T}_C = 80$ K). A design for a superconducting transistor fabricated by immobilized La1113 nanograins in between two gold electrodes which could be controlled by an external magnetic field gate is suggested. Furthermore, the mechanical reorientation of thiolated ferromagnetic microspheres bridging a pair of gold electrodes under an external magnetic field is studied. Finally, a flexible film made of graphene oxide flakes is prepared and characterized by X ray diffraction. It is achieved by the chemical oxidation of commercial graphite and the subsequent reaction with NaOH. It is found that the interlayer distance between graphene increases upon oxidation due to the formation of chemical groups and results in the delamination and flexibility of the flakes.

Contents

List of Figures

List of Tables

Chapter 1

Introduction

During the last half a century, electronic devices have shrunk every year following Moore's law (Moore, 1965), which states that the number of transistors that can be placed inexpensively on an integrated circuit approximately doubles every two years (see Figure 1.1). This trend has continued for more than fifty years (Figure 1.1 (top)) and it is predicted to continue for several more years (Figure 1.1 (bottom)). However, the costs for manufacturers follow an inverse trend which threatens the continuity of Moore's law since the costs of plants for the fabrication and testing are growing continuously. The performance-to-price ratio of chips may double every two years, but the cost of building the production plants keeps on growing quickly (for instance, Intel is spending \$ 7 billion upgrading its fabrication plants). Moreover, the fabrication becomes more complex as transistors shrink in size. The scale is staggering, but the current generation of chips is 40 nm across. It is hard to miniaturize integrated circuits below the 10 nm scale. Overall, design and research becomes more expensive with each new generation device. This observation is known as Rock's Law (or Moore's Second Law) (Ross, 2003) which states that fabrication costs follow an exponential decrease. Since increasing speed and miniaturization are the basis of electronic sector competition, there will be a high impact in the development of the information and communications technology when the limit of Moore's law is reached.

In order to continue increasing the speed, shrink the size and improve the power of electronic devices and thus to maintain the Moore's law, new materials and designs are needed. This holds for artificial materials with great potential

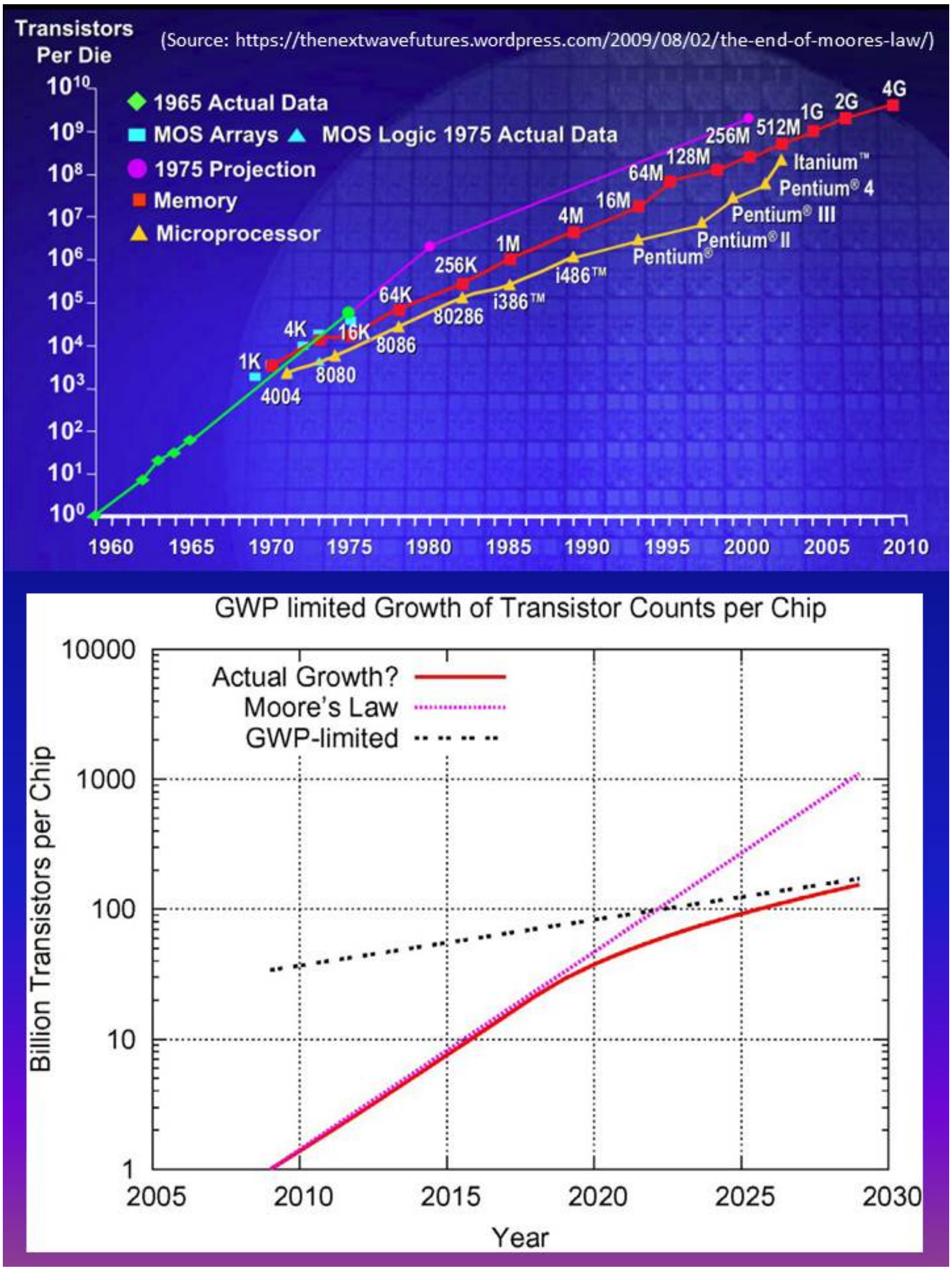

Figure 1.1: Moore's law for the last 50 years (up) and its projection up to 2030 (down). GWP: Gross World Product (economic limitations) (Rupp & Selberherr, 2011).

in novel devices. For example, materials that push the operating temperature of nanoelectronics devices to room temperature, new approaches in nanoparticles, new substrates, etc. The search for novel materials, thin metal films and oxides to replace the silicon-based nanoelectronics is currently an area of intense effort. In the next sections, both thin metal films, oxide materials and their manufacture are briefly described.

1.1 Thin metal films

In the case of thin metal films, the development of vacuum technology, new surface sensitive probes and powerful computational techniques permits a better study and provides new processes to be used in micro- and nano-electronics. Thin metal films range from fractions of a nanometer (monolayer) to several micrometers in thickness and they have many applications depending on the film construction. For example, there are abundant non-toxic materials with potential application in photovoltaic sollar cells (Alharbi *et al.*, 2011), new thin films such as silicon-oxycarbides are being investigated for ion battery applications (Shen & Raj, 2011), there is a rising interest in shape memory alloy thin films such as Fe-Pd because of the possibility to get rapid actuation response due to rapid heat dissipation (Han *et al.*, 2010) and so on.

For manufacturing, there are many techniques which allow the deposition of thin metal films onto a substrate or onto other deposited layers. The deposition techniques fall into two broad categories, depending on whether the process is primarily chemical or physical (Smith, 1995):

1.1.1 Chemical deposition

In this technique, a metal fluid precursor undergoes a chemical change at a solid surface, leaving a metal layer. The metal fluid surrounds the solid object, deposition happens on every surface, with little regard to direction. Thin metal films from chemical deposition techniques tend to be conformal, rather than directional. Chemical deposition is further categorized by the phase of the precursor:

1.1.1.1 Electroplating

Electroplating is a plating process in which metal ions in a solution are moved by an electric field to coat a surface (Schlesinger & Paunovic, 2010). The process uses an electrical current to reduce cations of a desired material from a solution and coat a conductive object with a metal. Electroplating is used for abrasion and wear resistance, corrosion protection, lubrication, aesthetic properties, etc. The process used in electroplating is called electrodeposition. It is analogous to a galvanic cell acting in reverse. The part to be plated is the cathode of the circuit while the anode is made of the metal to be plated. Both components are immersed in a solution called an electrolyte containing one or more dissolved metal salts as well as other ions that permit the flow of electricity. A power supply supplies a direct current to the anode, oxidizing the metal atoms that comprise it and allowing them to dissolve in the solution. At the cathode, the dissolved metal ions in the electrolyte solution are reduced at the interface between the solution and the cathode. The rate at which the anode is dissolved is equal to the rate at which the cathode is plated. In this manner, the ions in the electrolyte bath are continuously replenished by the anode. This technique is discussed in more detail in §2.3 and Chapter 5.

1.1.1.2 Chemical solution deposition

Chemical solution deposition (CSD) uses a liquid precursor, usually a solution of organometallic powders dissolved in an organic solvent. This is a relatively inexpensive, simple thin film process that is able to produce stoichiometrically accurate crystalline phases. This technique is also known as Sol-Gel (Sakka, 2010) because the “sol”(or solution) gradually evolves towards the formation of a gel-like diphasic system.

1.1.1.3 Chemical vapour deposition

Chemical vapour deposition (CVD) generally uses a gas-phase precursor, often a halide or hydride of the element to be deposited (Dobkin & Zuraw, 2010). In a typical CVD process, the substrate is exposed to one or more volatile precursors, which react and/or decompose on the substrate surface to produce the desired deposit. Frequently, volatile by-products are also produced, which are removed by gas flow through the reaction chamber. Plasma enhanced CVD (PECVD) uses an ionized vapour, or plasma, as a precursor.

1.1.2 Physical deposition

Physical deposition uses mechanical, electromechanical or thermodynamic means to produce the thin metal film (Smith, 1995). Since most metals can be held together by relatively high energies and chemical reactions are not used to store these energies, commercial physical deposition systems tend to require a low-pressure vapour environment to function properly. The metal to be deposited is placed in an energetic, entropic environment, so that particles of the metal escape its surface. Facing this source is a cooler surface which draws energy from these particles as they arrive, allowing them to form the solid layer. The whole system is kept in a vacuum deposition chamber, to allow the particles to travel as freely as possible. Since particles tend to follow a straight path, thin films deposited by physical means are commonly directional, rather than conformal. Examples of physical deposition include:

1.1.2.1 Thermal evaporation

Thermal evaporation uses an electric resistance heater to melt the metal and raise its vapour pressure to a useful range. This is done in high vacuum, both to allow the vapour to reach the substrate without reacting with or scattering against other gas-phase atoms in the chamber and to reduce the incorporation of impurities from the residual gas in the vacuum chamber. In this technique only metals with a much higher vapour pressure than the heating element can be deposited without contamination of the thin film. Molecular beam epitaxy is a particularly sophisticated form of thermal evaporation. In that case a high-energy beam from an electron gun boils a small spot of metal; since the heating is not uniform, a lower vapour pressure metal can be deposited. In this thesis, conventional evaporation in an EDWARDS 306 evaporator system was used to fabricate the thin metal films and the fabrication conditions for each sample will be discussed in each chapter.

1.1.2.2 Sputtering

Sputtering relies on a plasma (usually a noble gas, such as argon) to eject the metal from a “target”to deposit it onto a substrate (Wasa *et al.*, 2004). It is especially useful for metal compounds or mixtures. It is a fast technique and it also provides a good thickness control.

1.1.2.3 Pulsed laser deposition

This is a technique where a high power pulsed laser beam is focused inside a vacuum chamber to eject the metal of a target to be deposited on a substate (Eason, 2007). When the laser pulse is absorbed by the target, the energy first leads to electronic excitation and is then converted into thermal, chemical and mechanical energy resulting in evaporation, ablation, plasma formation and even exfoliation. The ejected species expand into the surrounding vacuum and are deposited on the typically hot substrate.

In this thesis, the chemical and physical deposition technique “electroplating”and the physical deposition technique “thermal evaporation”are used to fabricate different thin metal films on SiO_2/Si substrates. The morphology, crystallization and oxidation of the deposited thin metal films are studied for their potential use in nanoelectronics. Because there are many types of thin metal films which can be used in nanoelectronics, this thesis surveys the properties of three of them: gold, copper and nickel. It is not a thesis on the theory of metal surfaces but rather on some experimental characterization of these metals. SiO_2/Si was used as a substrate as it is commonly used in nanoelectronics. SiO_2 is an insulator which can be used as backside gate for nanoelectronic devices. It is easily produced by thermal oxidation of Si and it has great stability and good adherence to many metals (Benouattas *et al.*, 2000; Ferullo *et al.*, 2006; Xu *et al.*, 1993).

1.2 Oxide materials

Oxides are compounds containing oxygen atoms, usually in the oxidation state of -2. Oxides result when elements are oxidized by oxygen present in air. Since almost all elements are in contact with the atmosphere, then even materials which are considered to be pure elements often contain coatings of oxides which usually protect the material from further corrosion. In the presence of water and oxygen (or simply air), some elements such as lithium, sodium, potassium, rubidium, caesium, strontium and barium rapidly oxidize. The surface of most metals becomes oxides and hydroxides in the presence of air. Due to its electronegativity, oxygen forms chemical bonds with almost all elements to give the corresponding oxides. Nowadays, a broad range of functional properties such as piezoelectricity and ferroelectricity, high dielectric permittivity, superconductivity, colossal magnetoresistance and ferromagnetism have been found in oxide materials. Moreover, transition metal oxides are intensively studied for their complex phases, structural phase transitions, metal-insulator transitions and magnetic ordering transitions. Cuprates (such as $YBa_2Cu_3O_7$, $La_{2-x}Sr_xCuO_4$, Bi-Sr-Ca-Cu-O, etc) are high T_C superconductors (Poole *et al.*, 2007). Colossal magnetoresistance was discovered in manganites such as $LaMnO_3$ and derivates (Baldini *et al.*, 2011). Ferroelectricity and piezoelectricity in $PbZr_xTi_{1-x}O_3$ have wide applications (Popescu-Pogrion *et al.*, 2004). Graphene oxide is an attractive alternative to graphene for producing flexible electronic devices (Wei *et al.*, 2010). Manufacturing methods including doping, epitaxial superlattice growth and nanoengineering techniques make it possible to fabricate high quality nanostructures of different oxides and they are becoming an important part of many new electronic devices. Their novel properties make oxide electronics and the integration of oxides with semiconductors a promising approach to extend and accelerate information technology development. In this thesis superconductor oxide grains and graphene oxide are investigated for their use as novel components in nanoelectronic devices.

1.3 Structure of this thesis

The thesis studies some properties of thin metal films and oxide materials for their potential application in nanoelectronics. It is important to mention that no devices are presented, the study of thin metal films such as gold, copper and nickel and oxides such as $LaCaBaCu_3O_7$ and graphene oxide flakes for their potential use in nanoelectronics is discussed instead. In addition to this introductory chapter, the thesis contains eight further chapters; one of them describes the experimental techniques for the preparation and characterization of the samples, three of them discuss gold, copper and nickel thin films, another three refer to some oxide materials such as the superconductor oxide $LaCaBaCu_3O_7$, carboxil ferromagnetic microparticles and graphene oxide flakes and the last chapter presents the final conclusions and suggestions for further work. The overview structure of this thesis is presented in Figure 1.2 and briefly summarized as follow:

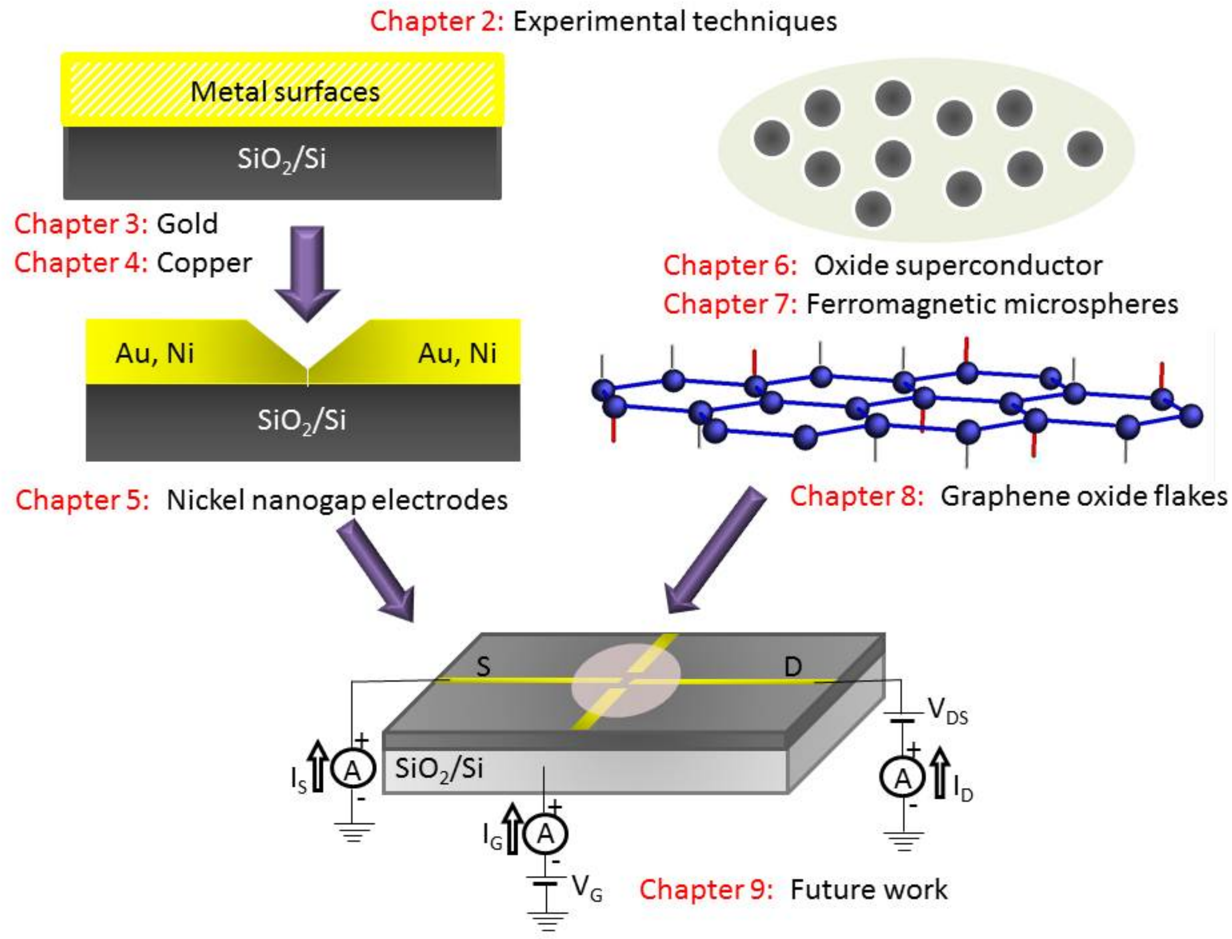

Figure 1.2: Structure of this Thesis

- **Chapter 2**: Introduces the experimental techniques used in this thesis for the fabrication and characterization of the samples.

- **Chapter 3**: Thin gold films on SiO_2 substrates were studied following annealing. It is found that thin Au films can be crystallized on SiO_2 substrates by annealing. Annealing arranges the Au crystallites in the [111] direction and changes the morphology of the surface, forming gold islands over the surface. It is suggested that a relaxation of the Au layer at high temperatures should be responsible for the initial stages of cluster formation.

- **Chapter 4**: In this chapter the crystallization and electrical resistivity of the prepared oxides in a $Cu/SiO_2/Si$ thin film by thermal oxidation are studied. The phase evolution $Cu \rightarrow Cu + Cu_2O \rightarrow Cu_2O \rightarrow Cu_2O + CuO \rightarrow CuO$ is detected during the oxidation of copper. A resistivity phase diagram, which is obtained from the current-voltage response, is also presented here.

- **Chapter 5**: In this chapter the fabrication of nickel nano-spaced electrodes by electroplating is discussed. The necessary reagents, conditions and process required to obtain nano and atomic gaps between soft and clean surfaces electrodes are described.

- **Chapter 6**: The oxide superconductor $LaCaBaCu_3O_7$ (La1113) is presented. Its functionalization and attachment to Au(111) surfaces through self-assembled monolayers (SAMs) is reported. In addition, a design for a superconducting transistor fabricated by immobilized La1113 nanograins in between two gold electrodes, which could be controlled by an external magnetic field gate, is suggested.

- **Chapter 7**: In this chapter, the mechanical reorientation of carboxil ferromagnetic microspheres bridging a pair of gold electrodes under an external magnetic field is studied. The physical reorientation of the ferromagnetic particles is sensed by I-V characterization and analyzed from the magnetic hysteresis response while suspended in a liquid solution.

- **Chapter 8**: In this chapter, the preparation and X-ray diffraction of graphene oxide flakes is reported. The preparation follows a chemical oxidation of commercial graphite and subsequent reaction with NaOH. The

X-ray diffraction reveals that the interlayer distance between graphene increases by oxidation due to the formation of chemical groups and results in the delamination and flexibility of the flakes, which can be used in nanoelectronics.

- **Chapter** 9: In this final chapter, the overall conclusions are stated and suggested further work is discussed.

Chapter 2

Experimental techniques

In this chapter some of the experimental techniques used for the fabrication and characterization of nanosized materials are described. The most employed techniques within this thesis are lithography (for the fabrication of the metal electrodes), X-ray diffraction (for crystallization studies), electroplating (for electrode nanogaps formation) and Magnetic Properties Measurement System (MPMS, for magnetic measurements). In this chapter, a general description of these techniques is presented. The following chapters contain the respective experimental sections in which details of the experimental conditions for each sample processing are described in more detail. Since there is extensive information in the literature about these techniques, a detailed theoretical description is out of the scope of this thesis. Instead, attention is focused on the procedure and general conditions followed during fabrication and characterization of the samples.

2.1 Lithography

In nanotechnology, lithography is the process of printing patterns onto a layer called a resist, using a localised interaction between the resist and an engraving micro-tool or particle beam. The lithographic technique can be classified according to the micro-tool or type of radiation used. The two types of lithography used in this work are photolithography and e^--beam lithography. Photolithography, also called "optical lithography", is a well known method used to produce a pattern by ultraviolet (UV) light. A wafer is coated with a photosensitive chemical resist and exposed to UV light through a photomask which is held against it or in close proximity. The mask has opaque and transparent parts which reproduce the relevant pattern. It is generally a quartz plate coated with a thin chromium layer in those regions where opacity is required. In contrast, e^--beam lithography scans a beam of electrons in the patterned regions of the resist. It allows better resolution than photolithography and nanometer sized features can be achieved without the use of lithography-masks. The limitation of e- beam lithography is the very long time it takes to pattern an entire wafer. After the pattern is transferred to the resist, removal of either the exposed or non-exposed regions of the resist ("developing") is required. The purpose of the lithography is to create very small structures in the resist that can subsequently be transferred to the substrate material, often by etching. For further detailed information on this stage, the reader is directed to the book published by Levinson (2010). In this work, metal micro- and nano-electrodes were fabricated on Si/SiO_2 wafers by combining traditional photolithography and e^--beam lithography. The main purpose was to obtain metal electrodes separated by micro- or nano-gaps which can be bridged with different types of particles. The electrodes then connect the particles with the measurement apparatus. The steps of the manufacturing process are now described in more detail.

2.1.1 Electrode design

Using the program Autocad, patterns for photolithography masks and e^--beam lithography were designed. The Autocad files were sent to Compugraphics Inc. for the fabrication of the chromium masks. The designs for the micro- and nano-spaced gap electrodes patterns are shown in Figures 2.1 and 2.2 respectively. In Figure 2.1, six patterns were drawn and they were uniformily distributed on the mask. Each pattern has four arrows (the electrodes) pointing at each other forming a cross. Two of them are intended to be used as source (S) and drain (D) electrodes and the other two as gate electrodes for the potential fabrication of electronic devices. The main differences between the patterns distributed on the mask are the S and D electrode tip angles and their respective gap widths. The electrode tips of the three devices located on the left column (called asymmetric) have different angles, whereas the electrode tips of the three patterns located on the right column (called symmetric) have a similar angle. The electrode tips in the vertical axes of each pattern are sharper than those of the S and D electrodes. The main purpose of this mask design is to obtain micro-gaps of variable sizes from 1μm to 2μm in which different types of microparticles will be attached. Moreover, the electrodes obtained with this photolithography mask are used to study the gap width evolution by electrodeposition as is discussed in more detail in Chapter 5. In Figure 2.2, the patterns for four devices are drawn and they are uniformily distributed on the mask. In contrast to the previous design, in which the critical characteristics are situated on the center, the critical characteristics of the new pattern (with dimensions 10 $\times$ 24 mm) are situated on the edge to give better handle during electroplating (See Chaper 5). Each pattern has three electrodes (source (S), drain (D) and gate (G)) pointing to each other. Depending on their critical characteristics, they are classified in two types: A and B. In type A, the three electrodes form an angle of 120° between them. In type B, only the S and D electrodes point to each other and the G electrode is perpendicular to them. The gap separations in all patterns is 200 nm. These patterns are intended to be used for those samples in the nanometer scale. On the bottom of Figures 2.1 and 2.2, additional patterns for a second photolithography process are found. They are called “windows”. The function of the windows is to expose circular and rectangular areas on the top of the critical characteristics and those areas in which wire connection will be necessary to be in contact with the atmosphere. The rest of the surface will be coated by a polymer to protect the electrodes and to prevent oxidation.

Figure 2.1: Design patterns for micro-gap electrodes

2.1.2 Resist coating

Resists are organic polymer solutions to be deposited on the wafers and destined to receive the radiation or the interaction used during the lithographic process.

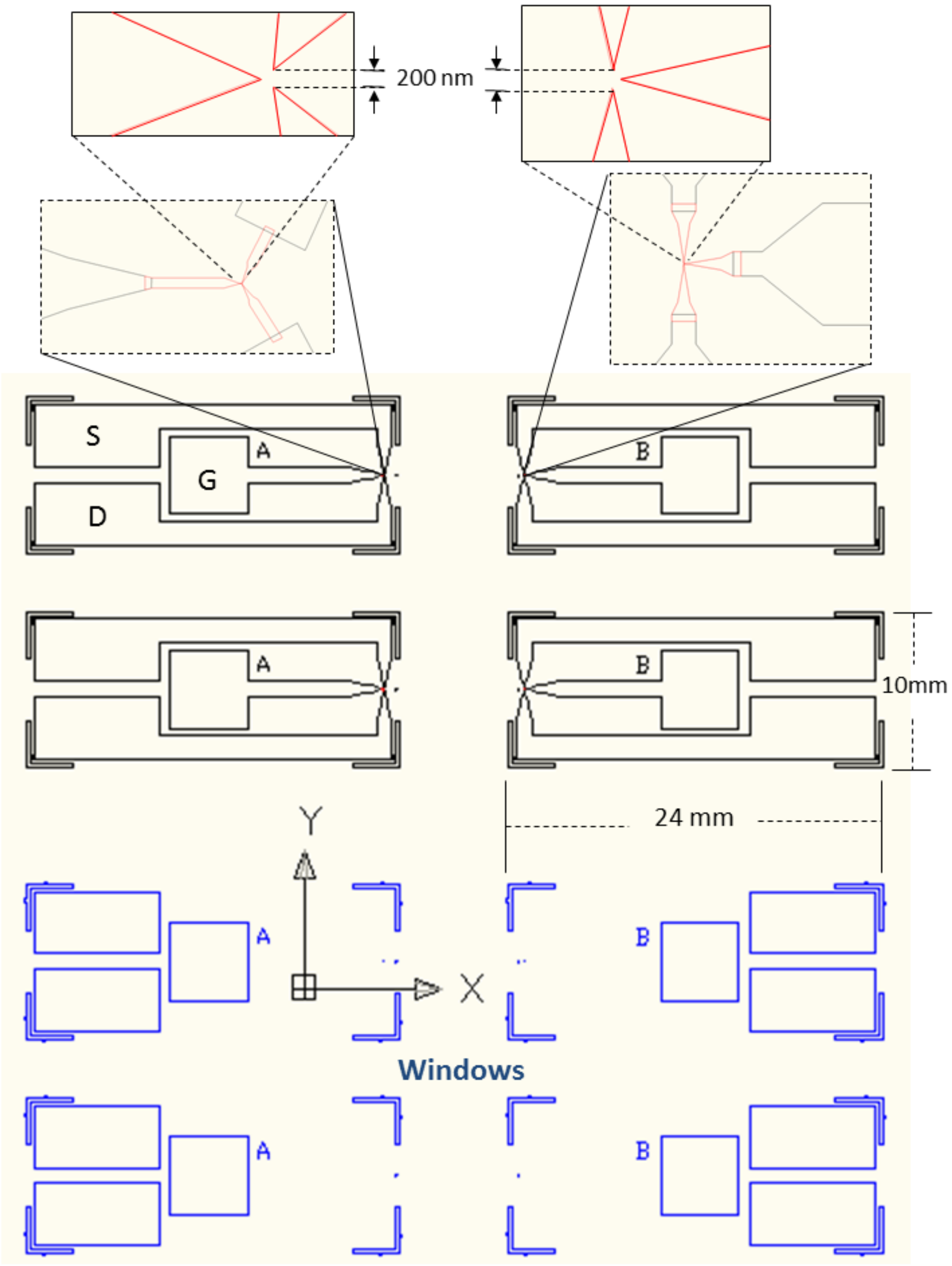

Figure 2.2: Design patterns for nano-gap electrodes

A polymer resist is typical for photolithography or e$^-$-beam lithography. Resists comprise two parts: a matrix, insensitive to the writing radiation, which fulfils the mechanical requirements of the resist, and an active component, sensitive to the radiation, which either accelerates or slows down the rate at which the resist dissolves in a solvent (the developer). There are thus two types of resists: positive resists for which exposure increases the solubility and negative resists for which exposure reduces the solubility. In this work, positive resists polymethyl methacrylate (PMMA, Microchem Inc.) and ZEP520A (diluted in ZEP-A (1:2 ratio), Zeon Corporation) were used for the photolithography and e$^-$-beam lithography respectively. Prior to coating, the Si/SiO$_2$ substrates were degreased in acetone and washed ultrasonically in isopropyl alcohol (IPA) following a standard procedure. The wafers were then spun about their axis at a high rate spin, flinging off the excess resist. For lithography, the PMMA was spun on the wafer and spun at 2000 rpm for 60 s to obtain a 600 nm thickness. For e$^-$-beam lithography, the ZEP520A + ZEP-A (1:2) was spin coated at 3000 rpm for 100 s to obtain around a 100 nm thickness. After the resist coating, soft bakes of the wafers at 180 °C for 4 min were followed to densify the resist and evaporate residual solvent.

2.1.3 Exposure

As mentioned in the last section, PMMA and ZEP520A are positive resists. They are insoluble in developers, but are made soluble by exposure to UV and e$^-$-beam radiation respectively. By exposing these resists selectively in the areas described in Figures 2.1 and 2.2, the patterns are created on the films. Many resist thicknesses and radiation doses were tried in order to achieve optimal results. In the case of the photolithography, the PMMA was exposed by a deep ultraviolet (DUV) light (240 nm wavelength) with 8.9 mW/cm^2 intensity using a mask aligner model MJB4 (SUSS Microtech). For the patterns which required e$^-$-beam lithography, two equipments were used: a LEICA VB6 UHR from the Cavendish electron beam nano-lithography facility (beam voltage 100 kV and current density 2000 Acm^{-2}), and a Jeol JBX-6000FS from the Materials and

Structures Laboratory of the Tokyo Institute of Technology (beam voltage 50 kV, beam current of 100 pA and irradiation dose of 100 μC/cm^2).

2.1.4 Developing

In this step, the exposed areas of the resists are removed with developers. Comercial developers for optical resists usually contain sodium hydroxide (NaOH). However, sodium is considered an extremely undesirable contaminant in nanoelectronic devices because it degrades the insulating properties of gate oxides. Metal-ion-free developers such as methyl ketones are now used. In this work, methyl isobutyl ketone (MIBK, Microchem Inc.) was used to remove the exposed areas of the resist with DUV. The photolithography samples were inmersed in a beaker containing MIBK diluted in IPA (1:2) for 10 min. For the e$^-$-beam lithography, amyl acetate (ZED-N50, Zeon Corporation) was used. The developed samples were then post-baked at 120 °C for 20 min. This was to make the remaining resists more durable.

2.1.5 Metal deposition

The developed patterned wafers were deposited with three different metals separately: gold, copper or nickel. For that purpose, small Au, Cu or Ni pellets (99.999% purity) were evaporated from a boat on to polished SiO_2 (80nm)/Si(100) substrates using a BOC Edwards 306 evaporator system with a base pressure of 10^{-7} mbar. The rate of evaporation was maintained at 0.1 nm/s and the thickness of the metals (40-100 nm) was measured by a quartz crystal microbalance located next to the wafers. Before evaporating gold, a thin layer of Ti (5 nm) was deposited as an adhesion promoter.

2.1.6 Lift-off

After metal deposition, the resists were no longer needed and they were removed from the substrates: hardened PMMA was disolved in acetone with the help of a hot plate at 70 °C for 4 h, whereas the ZEP520A + ZEP-A was removed with dimethylacetamide (ZMAC, Zeon Corporation).

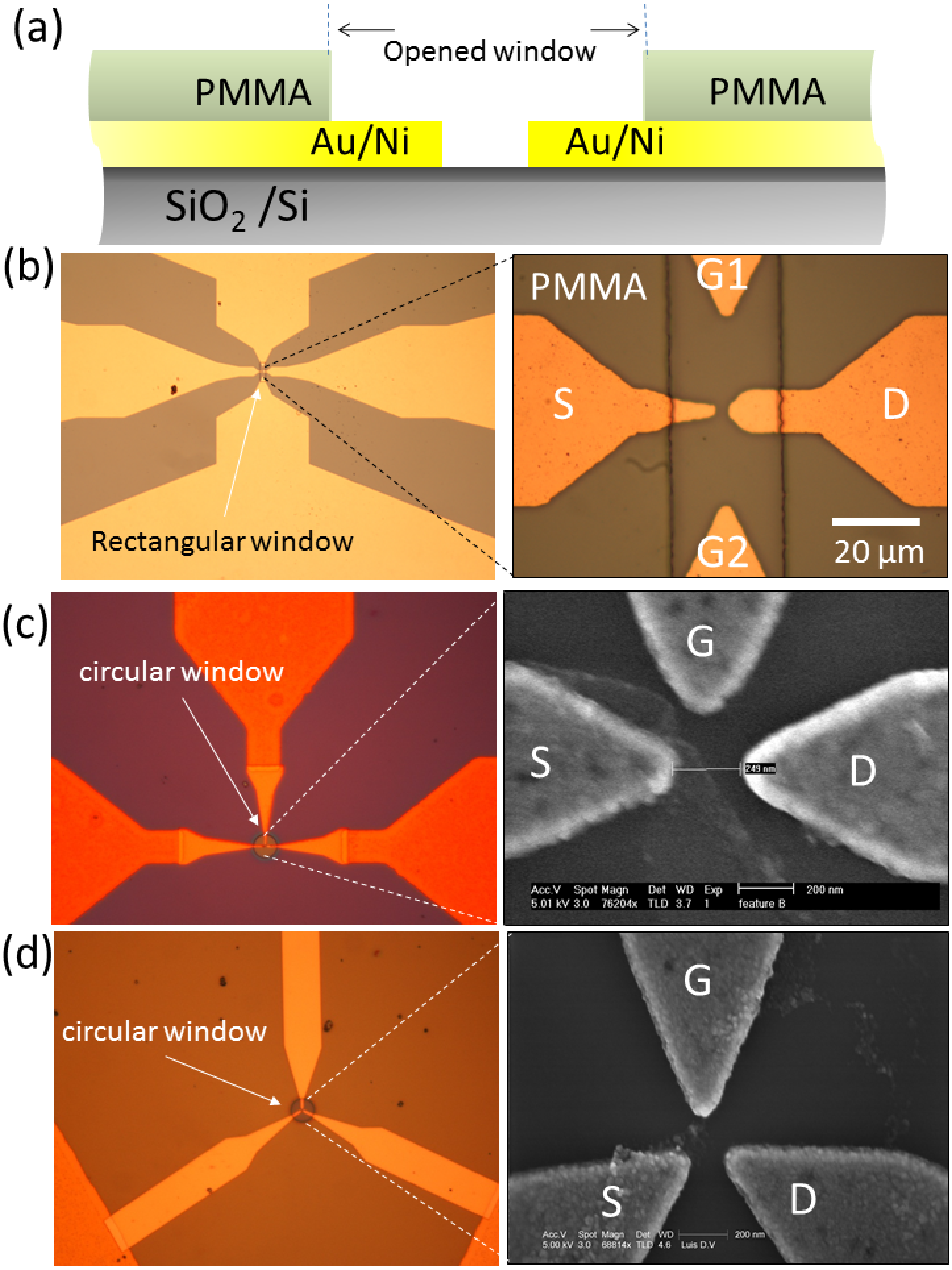

Figure 2.3: Lithographically defined metal electrodes for the present work: (a) representation of the transverse section of an arbitrary pair of electrodes, (b) electrodes obtained with the patterns shown in Figure 2.1, (c) and (d) type A and B electrodes obtained with the patterns shown in Figure 2.2.

Some of the electrodes obtained following the procedures described above are shown in Figure 2.3. A cross-section representation is shown in Figure 2.3a. SiO_2/Si is used as a substrate in this work as it is commonly used in nanoelectronics. SiO_2 is an insulator which can be used as a backside gate for nanoelectronic devices. It is easily produced by thermal oxidation of Si and it has great stability and good adherence to copper and nickel (Benouattas *et al.*, 2000; Ferullo *et al.*, 2006; Xu *et al.*, 1993). The electrodes are made of gold or nickel, depending on their application, as described in the following chapters. Copper is not used for the critical features due to its ease of oxidation as described in Chapter 4. It is used mainly in larger areas of the samples and for wire connections. A protective layer of PMMA allows easier handling of the samples and prevents oxidation and surface damage during cutting. Rectangular or circular windows are opened on the tips of the electrodes for each sample. Figure 2.3(b) shows some electrodes obtained with the patterns shown in Figure 2.1. The horizontal electrodes (S and D) are separated by a 2 μm gap. These electrodes were used for growth evolution studies of the electrodes by electrodeposition and for attaching ferromagnetic microspheres, which will be described in more detail in Chapters 5 and 7 respectively. Figures 2.3 (c) and (d) show some type A and type B electrodes obtained with the patterns shown in Figure 2.2. They are separated by approximately 200 nm and obtained mainly by e^--beam lithography. They will be used for nanogap formation as described in Chapter 5. Those samples which followed electrodeposition were connected to copper wires (125 μm diameter) by silver conductive paint and cured at 110 °C for 20 min. Alternatively, some samples were cut and bonded to chip carriers by gold wires.

2.2 X-ray diffraction - XRD

X-rays are elecromagnetic radiation with high energy and small wavelength. When it is incident on a solid material, part of the beam is diffracted (Figure 2.4a). This phenomenon happens if the atoms of the material are well arranged (crystallites) and the Bragg condition, which relates the wavelength of the X-ray with the interatomic distance and the incident angle of the incident beam, is met. If the Bragg condition is not satisfied, the nature of the diffraction is not constructive and the diffracted intensity of the beam is weak. The fundamental application of XRD is the qualitative identification of the mineral composition of crystalline samples and their unit cell parameters. A diffractometer registers the diffracted beam from a crystalline sample which is irradiated with a monochromatic X-ray such as that of the Cu Kα line. The detector is specially designed to collect the distribution of the diffracted intensity from the sample as a function of the scanning angle 2θ (see Figure 2.4b).

Considering an arrangement of atoms and the X-ray diffraction planes as shown in Figure 2.4a, according to the Bragg law, constructive interference occurs when:

$$n\lambda = 2d \sin\theta \tag{2.1}$$

where θ is the incident angle between the X-ray radiation and the sample, d is the interplanar distance which is characteristic for each crystalline sample. In general, when an X-ray is incident on a sample, it interacts with many crystallites oriented in different directions (Figure 2.4b) . The geometry of the equipment permits the detection of only the reflected X-ray with θ angle. A typical sample contains crystallites and grain boundaries, so around 80% of the signal comes from the crystallites (grain sizes $\approx 10^{-6}\text{m} = 10^{4}\text{Å}$) and 20% comes from the grain boundaries. The Bragg law allows the calculation of interplanar distances. For example, the interplanar distances of the family of planes represented in Figure 2.4c are:

$$d_{100} = a \tag{2.2}$$

$$d_{120} = a\cos\theta = a\frac{a}{\sqrt{a^2+4a^2}} = \frac{a}{\sqrt{5}} \tag{2.3}$$

From Equation 2.1:

$$\sin\theta_{100} = \frac{\lambda}{2d_{100}} = \frac{\lambda}{2a} \tag{2.4}$$

$$\sin\theta_{120} = \frac{\lambda}{2d_{120}} = \frac{\sqrt{5}\lambda}{2a} \tag{2.5}$$

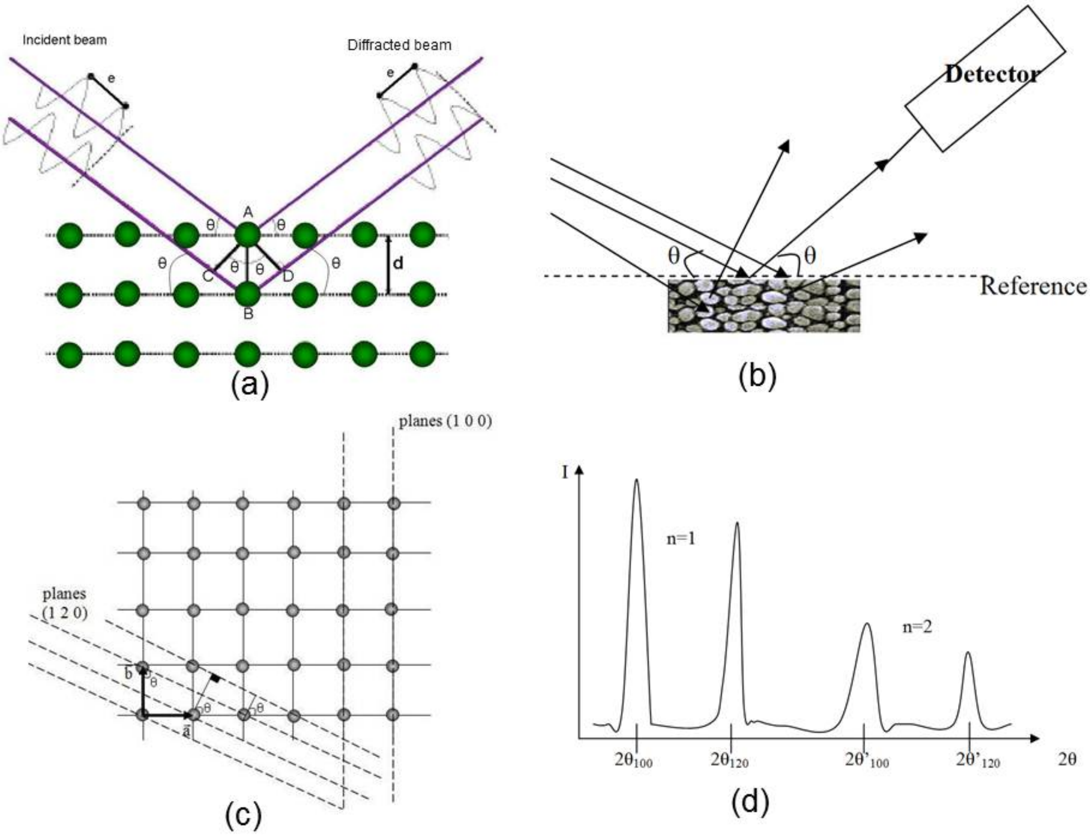

Figure 2.4: Representation of (a) an incident X-ray beam on a crystal with inter-layer distance d, (b) random oriented crystallites in a polycrystalline sample (the detector is specially designed to collect the distribution of the diffracted intensity from the sample as a function of the scanning angle 2θ) (c) family of planes in a crystalline structure in which a, b and c are the crystal parameters, and (d) an X-ray diffractogram.

Also,

$$\sin\theta_{120} > \sin\theta_{100} \tag{2.6}$$

Then, $\theta_{120} > \theta_{100}$; θ_{120} and θ_{100} are $< \pi/2$ and $d_{100} > d_{120}$

A diffractogram, such as that represented in Figure 2.4d, registers the intensity of the diffracted X-rays as a function of the scanning angle 2θ. In particular, for a family of planes hkl, the Bragg law is:

$$n\lambda = 2d_{hkl}\sin\theta^{\lambda}_{hkl} \tag{2.7}$$

where the interplanar distance d_{hkl} is characteristic of the crystallites forming the sample. θ^{λ}_{hkl} depends on the wavelength λ of the incident beam over the hkl planes.

In this thesis, the XRD measurements were performed in collaboration with Prof. Angel Bustamante (University of San Marcos, Peru), using a Rigaku diffractometer with a Bragg - Brentano geometry and using $K\alpha$-Cu wavelength radiation ($\lambda = 1.5418\mathring{A}$), 30 kV voltage, 15 mA current intensity and a nickel filter.

2.3 Electroplating

Electroplating is a well-known technique for coating surfaces with different metal films; there are plenty of literature reports about the application of this technique to relatively large-area surfaces (Schlesinger & Paunovic, 2010). By creating a potential difference between a metal surface and an auxiliary electrode inmersed in an electrolyte, oxidation and reduction (redox) reactions occur and the metal ions from the electrolyte are deposited on the electrode surfaces. The oxidation of a substance is characterized by the loss of electrons, while the reduction is distinguished by a gain of electrons. Metal displacement from the electrolyte to the metal surface is achieved by reduction. In this section we describe the electrodeposition process and the conditions used to form nanogaps between the nickel electrodes described in §2.1.

The process takes place in a standard electrochemical cell, like that represented in Figure 2.5 used in this work. The potential is controlled and measured between a reference electrode (R.E.) and a working electrode (W.E. - cathode), the sample. An auxiliary electrode (counter electrode, C.E.) is placed at the anode and the current is measured between this electrode and a cathode. During plating, voltage differences produce redox reactions in the system and result in the deposition of the metal ions (M^{Z+}) onto the sample. In general, the redox equation for a metal solution in a basic electrochemical cell is expresed by equation 2.8. At the anode, the metal ions are oxidized, becoming M^{Z+}. These ions associate with other ion components in the electrolyte and are attracted by the negative charge of the sample surface.

$$M^{Z+} + Ze^{-} \longleftrightarrow M \tag{2.8}$$

Since the electrolyte consists of metal ions in aqueous solution (aq), there is more than one reaction that can take place (Palfreyman, 2009); among them, the reaction of water should be considered:

$$2\mathrm{H_2O(l)} + 2\mathrm{e}^{-} \rightarrow \mathrm{H_2(g)} + 2\mathrm{OH^{-}(aq)} \tag{2.9}$$

which divides into two half reactions, each of which will occur at one of the electrodes, the anode and cathode respectively (Cooper, 2011):

$$2\mathrm{H_2O(l)} \rightarrow \mathrm{O_2} + 4\mathrm{H^{+}(aq)} + 4\mathrm{e}^{-} \tag{2.10}$$

$$2\mathrm{H^{+}(aq)} + 2\mathrm{e}^{-} \rightarrow \mathrm{H_2(g)} \tag{2.11}$$

At the anode, the hydrogen and oxygen are the oxidant (electron acceptor) and water is the reductant (electron donor). At the cathode, the hydrogen ions are the oxidant and gaseous hydrogen is the reductant. After a certain period of time a dynamic equilibrium results.

2.3.1 Cyclic voltametry (CV)

Cyclic voltametry (CV) is an electrochemical technique which provides information about the thermodynamics of redox processes, kinetics of heterogeneous electron-transfer reactions, coupled chemical reactions, detection of the surface

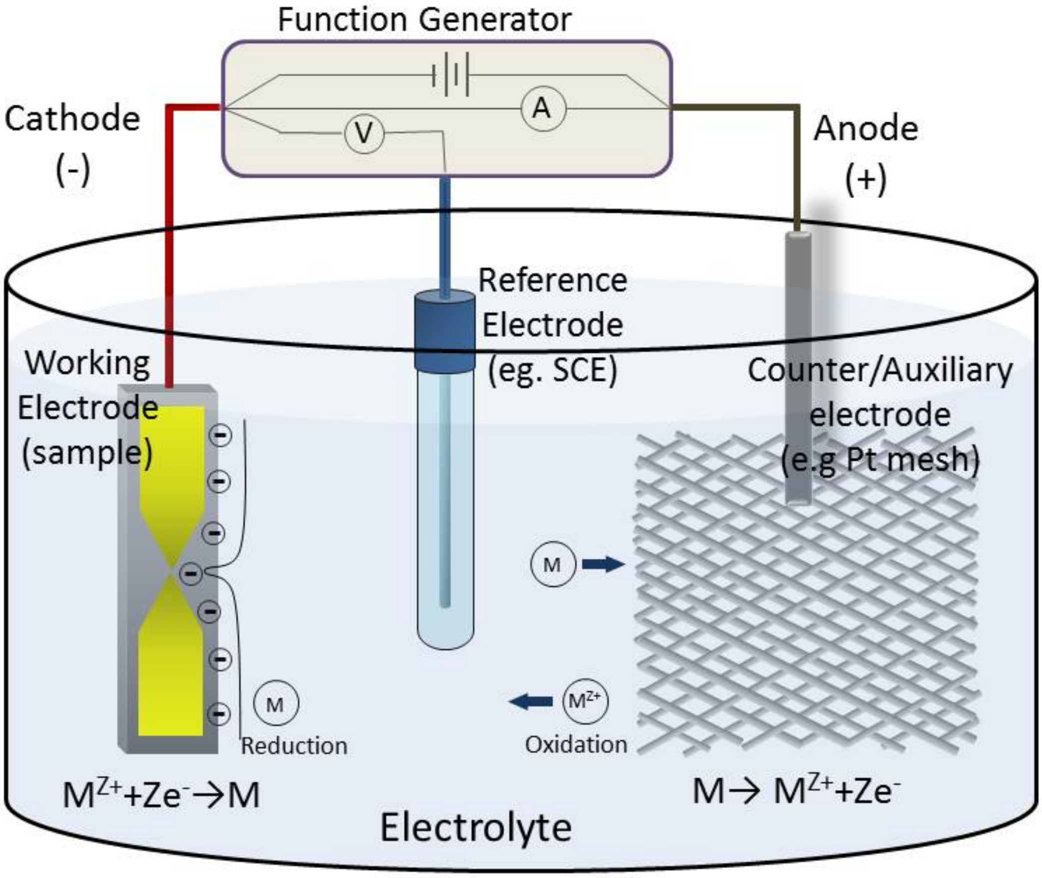

Figure 2.5: Conventional cell for electrodeposition. The sample is placed at the cathode and the voltage is referenced against a reference electrode.

processes like absorption, oxide layer information, etc. CV involves the imposition of a triangular waveform as a potential on the working electrode, like that represented in Figure 2.6, by the function generator with the simultaneous measurement of the current.

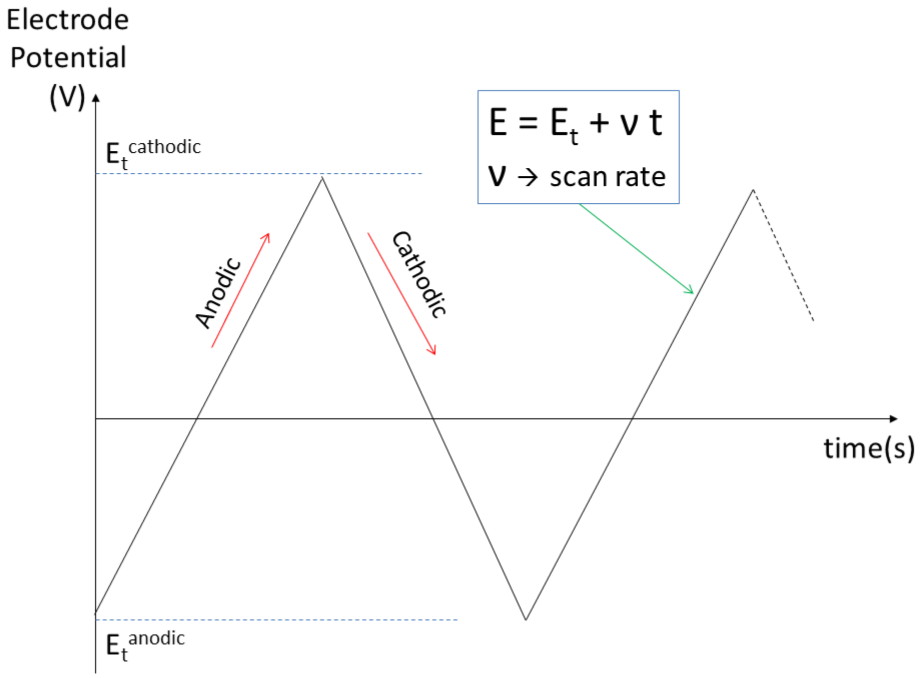

Figure 2.6: Triangular waveform of the potential as a function of time on the working electrode produced by the function generator. By convention, the positive forward voltage is called “anodic direction”, whereas the negative reverse voltage is called “cathodic direction”.

The negative and positive turn-round potentials ($E_t^{cathodic}$ and E_t^{anodic}) have the advantage that any adsorbed impurities blocking the electrode of interest can be removed either by oxidation or reduction. Moreover, reproducible behaviour in CV depends on a series of parameters such as the electrolyte purity, the electrode material, the choice of the turn-round $E_t^{cathodic}$ and E_t^{anodic} potentials and the rate of change of the potential (sweep or scan rate “v”). Typical scan rates lie between 5 mV/s and 1 V/s. For complex reactions, the sweep rate is recommended to be slow (e.g. 10 mV/s).

Considering the interface between the electrode and electrolyte as represented in Figure 2.7, two types of current appear:

$$I(t) = \underbrace{\alpha D^{1/2} v^{1/2}}_{I_{Faradic}} + \underbrace{\alpha C v}_{Capacitance-contribution} \tag{2.12}$$

where D is the diffusion coefficient, V is the scan rate and C is the capacitance.

In addition, the internal resistance of the electrolyte causes an additional drop in the potential:

$$\mathrm{V(t) = V_{app}(t) - I(t)R} \tag{2.13}$$

where V(t) is the working electrode potential, V_{app} is the applied cell voltage and I(t)R is the ohmic potential drop caused by the internal resistance of the electrolyte. If cyclic voltammograms with rapid scan rates are required (> 10 V/s), then I(t)R needs to be very small.

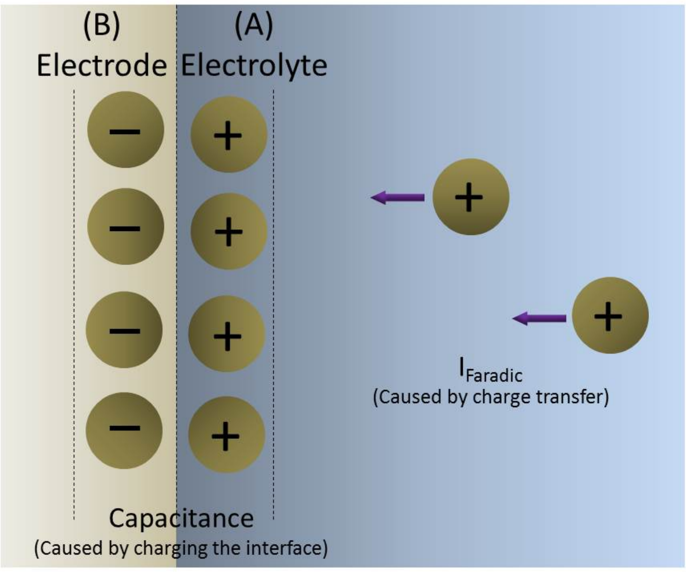

Figure 2.7: A Faradic current and capacitive layer appear at the electrode and electrolyte interface.

In order to simplify the theoretical analysis, only reduction processes are considered. At the begining of the plating process, as the potential rises, the surface concentration C_A of the reacting electrolyte falls from the bulk concentration C_0 towards C_A=0. Due to the differences between the concentrations of the electrolyte frontier (C$_A$), the electrode frontier and the rest of the solution, a gradient $(\frac{C_0-C_A}{\delta_N})$ emerges and increases as C_A decreases. Then, the flux of material from the electrolyte to the surface decreases. This mass transport is mediated by diffusion. However, δ_N also increases with time following the expression $\delta_N = \sqrt{\pi D t}$. And eventually, at higher potentials, when charge transfer is fast and the current has reached its mass-transport-limited value, increasing δ_N will cause the current to decrease again.

The above process can be better understood from the current variation as a function of the electrode potential represented in Figure 2.8 and described as follows:

- **Zone 1**. The surface concentration of A decreases while that of B increases. In this zone, the current is dominated by Faradic electron transfer and it increases exponentially: $I\alpha\frac{1}{t}$.
- **Zone 2**. As C_A tends to zero, the concentration gradient $(\frac{C_0-C_A}{\delta_N})$ and δ_N (the thickness of the difussion layer) increase with time. The flux of material from the electrolyte to the surface of the electrode starts (e.g beginning of diffusion effect). The increase of I slows following $I\alpha\frac{1}{\sqrt{\pi D t}}$.
- **Zone 3**. The surface concentration of A becomes negligible (C$_A$≈0). The influence of mass transport becomes similar to the influence of charge transfer (diffusion). The reversible potential of the redox is reached. I reaches a maximun I_P and it is described by the Randless-Sevcik equation (Hamann *et al.*, 2007):

  $$I_P = 2.69 \times 10^5 n^{3/2} D^{3/2} A C \nu^{1/2} \tag{2.14}$$

  where the constant C has units mol^{-1}V$^{1/2}$ and represents the bulk concentration in mol/cm^3, n is the number of electrons transferred, A is the area of the electrode in cm^2, D is the diffussion coefficient of the species in cm^2/s

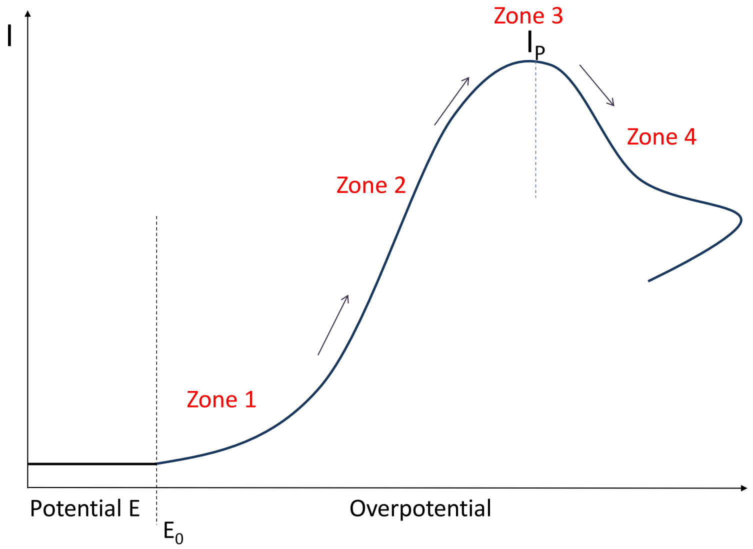

Figure 2.8: Current variation as a function of electrode potential.

and ν is the scan rate in V/s. In addition, it is empirically known that as the sweep rate increases, the peak occurs at higher potential values.

- **Zone 4**. In this zone, δ_N increases independently of the potential, causing I to decrease. Deposition continues on electrode B, dominated by mass transport (diffusion).

2.4 Magnetic measurements

The magnetic characterization of those samples for which it was required, was performed in a Direct Current - Magnetic Property Measurement System (DC-MPMS) equipped with a Superconducting Quantum Interference Device (SQUID) from the Quantum Design Company. The system consists of a superconducting coil, with a SQUID sensor, as is schematically represented in Figure 2.9. The superconducting coil creates a DC magnetic field applied to the sample inside the coil. During measurements, the sample is moved upwards and downwards in the set of coils and thus a current is induced on the coils. This current is proportional

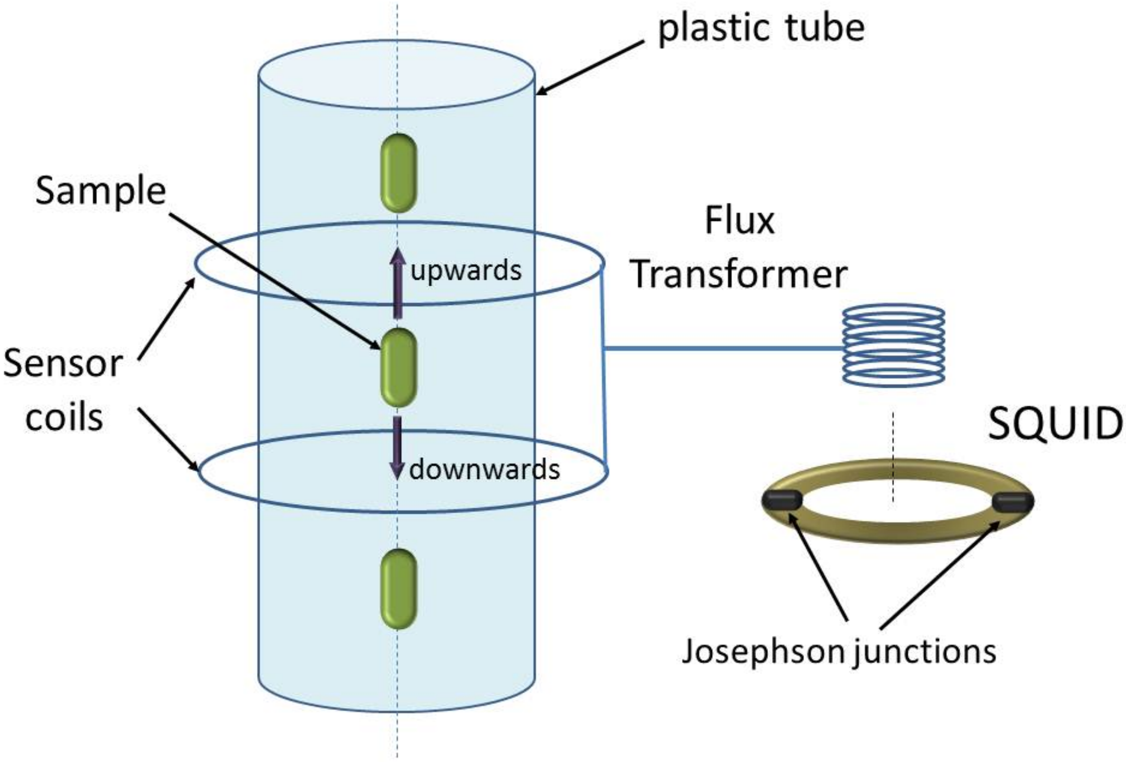

Figure 2.9: Schematic representation of a magnetic property measurement system (MPMS). Raising and lowering the sample produce a change in the magnetic flux in the sensor coils and induces a current which is transferred to a multiloop coil where it is measured by a SQUID sensor.

to the change of the magnetic flux. The signal is amplified by the SQUID sensor which is a superconducting loop containing two Josephson junctions. At each junction there will be a phase difference in the wave-functions of the different superconductors. This phase difference, $\delta\theta$, is proportional to the magnetic flux threading the whole ring, Φ, by:

$$\Delta\theta = \frac{2e}{\hbar}\oint \mathbf{A}.d\mathbf{l} = \frac{2\pi\Phi}{\Phi_0} \tag{2.15}$$

where $\Phi_0 = \frac{h}{2e} = 2 \times 10^{-7}$ gauss cm. The critical current, I_C, which is able to pass through the SQUID loop without dissipation is also dependent on the threading flux. Thus if a bias current equal to I_C is applied, then the voltage is:

$$\Delta V = \frac{R}{L} \Delta \Phi \tag{2.16}$$

where L is the self inductance of the loop.

SQUIDs are sensitive enough to measure extremely weak magnetic fields and moments as low as 5×10^{-18} T and 10^{-7} emu [1] respectively. Their noise levels are as low as 3 fT $\mathrm{Hz}^{-1/2}$ (Drung *et al.*, 2007). The system is contained in a helium cryostat so that the temperature can be controlled between 5K and room temperature (RT). To ensure enough homogeneity of magnetic field during the sample displacement, the centre was previously calculated by measuring a piece of permalloy and displacements of 3 cm were set during the sequence routine.

In Chapter 7 the magnetic hysteresis of magnetic microspheres in liquid suspension is performed. However, since the standard holder for the magnetometer consists of a simple gelatine capsule designed specially for powder or dried samples, a new holder for liquid solution was designed. The encapsulated sample is placed in a plastic tube (Figure 2.9) and then slid down into the MPMS (*i.e.* in a low pressure environment). There are two risks at this point. Firstly the capsule begins to dissolve on contact with the liquid sample. Secondly the low pressure in the SQUID equipment could induce evaporation and in this way not only are the samples lost, but also the equipment could suffer serious damage. To overcome these problems, a new sample holder was designed. It consisted of a diamagnetic truncated cone made of plastic, 13 mm long (see Figure 2.10). A drop of approximately 1 μL of suspended beads in sucrose solution with a concentration of about 1.0% w/V was added, and the ends were sealed with mounting wax. The new container was robust enough to support an external pressure of 10^{-5} mbar in a previous test performed in a thermal evaporator (BOC Edwards 306). In addition, since the density of water is too low to suspend particles over long

---

[1] The unit for magnetic moment is not a base unit in the International System of Units (SI) and it can be represented in more than one way (in A m^2 or in J T^{-1}, which are equivalent). However, for small magnetic moments values, the CGS unit emu ($= 10^{-3}$ A m^2 or J T^{-1}) is frequently used.

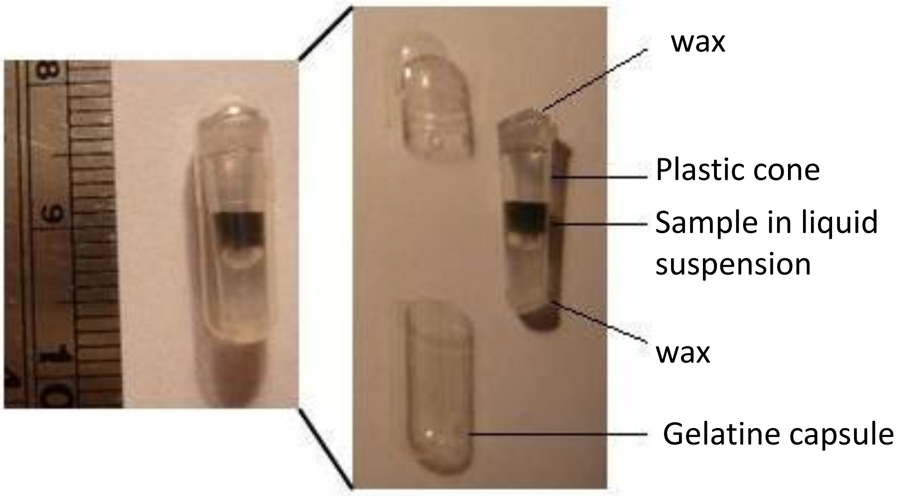

Figure 2.10: Specially designed sample holders for measuring samples in liquid suspension in a MPMS-SQUID. Note that there is no precipitation in the dark coloured solution

timescales (4 to 6 hours are required to acquire data from the magnetometer), the samples were suspended in 40% w/V sucrose solution. The liquid solution was prepared by diluting 4 g of sucrose (Sigma Ultra 99.55 GC) in 6 ml of distilled water.

Despite the fact that the behaviour of magnetic particles in fluids can be deduced by means of particle fluid-dynamics, electrophoresis and magnetophoresis theory, few experimental studies can be found in the literature. Most theoretical formulas are obtained for particles in the size range from approximately 1 μm to 1 mm because the mechanics of submicron particles are strongly influenced by random thermal (Brownian) motion and Van der Waals forces. The upper limit (10^{-3} m) is based on a reasonable working definition of what constitutes a classical particle (Fannin *et al.*, 2006; Thomas & Jones, 1995). The principal forces acting

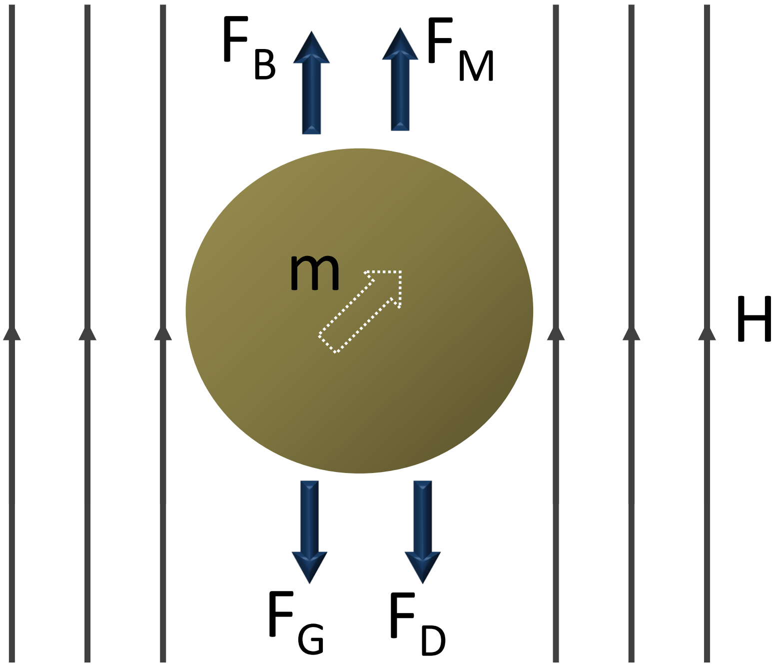

Figure 2.11: Representation of the forces acting on a microsphere in suspension and under an applied magnetic field. The MPMS takes some seconds while increasing or decreasing H. F$_M$ and F$_D$ appear during that time interval.

on a microsphere in liquid suspension and under an external magnetic field are represented in Figure 2.11. Without the magnetic field, the two main forces acting over a microsphere are the gravitational force (F$_G$) and the buoyancy force (F$_B$), which cancel each other in opposite directions at equilibrium:

$$F_G = \frac{\rho_p \pi d_p^3 g}{6} \tag{2.17}$$

$$F_B = \rho_a \frac{\pi d_p^3 g}{6} \tag{2.18}$$

where ρ_p and ρ_a are the densities of the microsphere and the fluid respectively, d_p is the diameter of the microsphere and g is the aceleration due to gravity. When the external magnetic field is applied, a force called the “magnetophoretical” force (F$_M$) appears and, according to Thomas & Jones (1995):

$$F_M = 2\pi\mu_1 r^3 \left(\frac{\mu_2 - \mu_1}{\mu_2 + 2\mu_1}\right) \nabla H^2 \tag{2.19}$$

where μ_1 and μ_2 are the magnetic permeabilities of the fluid and the microsphere, respectively. H is the external applied field and r the radius of the microsphere. In addition, a drag force F_D appears every time the particle changes position:

$$F_D = \frac{\pi d_p^3 \rho_a v^2 C_D}{8} \tag{2.20}$$

where C_D is the drag coefficient ($\approx$24/Re, where Re is the Reynolds number; since the regime for microfluids is laminar, Re < 2.0 (Hansen *et al.*, 2007)).

Measuring hysteresis loops of magnetic microspheres suspended in fluids is rarely reported in the literature. In most studies, the hysteresis loops in suspension are indirectly derived from AC susceptibility measurements (Cung *et al.*, 2004; Fannin & Charles, 1999; Fannin *et al.*, 1999; Kötzitz *et al.*, 1999; Prieto-Astalan *et al.*, 2004). The principal reason is the lack of suitable equipment for this task, although some researchers have designed their own instruments to measure susceptibility as a function of H (e.g. the toroidal technique designed by Fannin (1986)).

With this knowledge of the experimental details, we can move on to the description of the samples studied in this thesis. It starts with thin gold films in the next chapter and continues with the other materials in the subsequent chapters.

Chapter 3

Thin gold films: Crystallization and surface morphology following annealing

In this chapter, the crystallization and surface evolution study of thin Au films on SiO_2 substrates following annealing at different temperatures above the eutectic point of the Au/Si system is reported. Samples were prepared by conventional evaporation of gold in a high vacuum (10^{-7} mbar) environment on substrates at room temperature. Thermal treatments were performed by both furnace and flame annealing techniques. Thin Au films can be crystallized on SiO_2 substrates by both furnace and flame annealing. Annealing arranges the Au crystallites in the [111] direction and changes the morphology of the surface. Both slow and rapid annealing result in a good background in the XRD spectra and hence clean and complete crystallization which depends more on the temperature than on the time of annealing. The epitaxial temperature for the Au/SiO_2 system is in the range of 350 °C - 400 °C. Furnace and flame annealing also form crystallized gold islands over the Au/SiO_2 surface. Relaxation at high temperatures of the strained Au layer, obtained after deposition, should be responsible for the initial stages of cluster formation. Gold nucleation sites may be formed at disordered points on the surface and they become islands when the temperature and time of annealing increase. The growth rate of crystallites is highest around 360 °C. Above this temperature the layer melts and gold diffuses from the substrate to the nucleation sites to increase the distance between the islands and modify their shapes. Well above the eutectic temperature, the relaxed islands have hexagonally shaped borders. The mean crystallite diameters grow up to a maximum mean size of around 90 nm. The free activation energy for grain-boundary migration above 360 °C is 0.2 eV. Therefore the type of silicon substrate changes the mechanism of diffusion and growth of crystallites during annealing of the Au/Si system. Epitaxial Au(111) layers without formation of islands can be prepared by furnace annealing in the range of 300 °C - 310 °C and by flame annealing of a few seconds and up to 0.5min.

3.1 Introduction

Thin gold films are used for many applications such as in circuit boards and sensor manufacturing (Kepley *et al.*, 1985). Au is favorable because it is highly conductive and it is not easily oxidized. Nowadays there is special interest for the formation of self-assembled monolayers (SAMs) of thiolated molecules on gold surfaces; this is achieved by taking advantage of the covalent link between the sulfur of a thiol group of the molecule and the Au substrate. There are plenty of reports in the literature on this subject (Dubois & Stellacci, 2008; Harder *et al.*, 1998; Herrwerth *et al.*, 2003; Rundqvist *et al.*, 2005; Valiokas *et al.*, 1999, 2000; Vanderah *et al.*, 2000; Zolk *et al.*, 2000). To facilitate the formation of SAMs, it is desired that the molecular axis is almost perpendicular to the Au surface. In the case of alkane thiols, the bonding configuration of the gold and the molecular axis is tilted 20° - 30° off the surface normal only when the Au crystallites in the thin film are orientated in the [111] direction (Hähner *et al.*, 1992; Nuzzo *et al.*, 1989; Ulman, 1996; Ulman *et al.*, 1989).

Preparation of epitaxial Au(111) has primarily involved distinct methods such as annealing-sputtering on crystal surfaces (Gibbs *et al.*, 1988; Liew & Wang, 1990; Ocko *et al.*, 1990; Telieps *et al.*, 1990; Zei *et al.*, 1989), molecular beam epitaxy (Sellmann *et al.*, 2001) and pulsed laser deposition (Scheibe *et al.*, 1990), all of which require ultra-high-vacuum conditions (around 10^{-10} mbar). However, other easier to implement techniques also exist to achieve the [111] direction of gold surfaces such as furnace annealing (Caune *et al.*, 1991; Mancini & Rimini,

1970) and flame annealing (Hamelin *et al.*, 1990; Kolb & Schneider, 1985). In the former the heating rate is almost constant whereas in the latter the heating rate is linear or exponential.

Regarding the substrates used for Au deposition, one of the best materials is mica because it is smooth, does not require an adhesion promoter such as chromium or titanium to produce thin films with good mechanical properties (Chidsey *et al.*, 1988; Dishner *et al.*, 1998) and produces large and flat crystallites (Golan *et al.*, 1992). Based on the fact that the substrate temperature during deposition plays an important role in metal surface crystallization (Brück, 1936), it is possible to obtain a well-defined orientation above a critical temperature called the "epitaxial temperature" (which also depends on the type of substrate). Below the critical temperature crystallites are randomly oriented. For gold on mica the epitaxial temperature is around 450 °C (Pashley, 1956). Furthermore, it has been found that when evaporating gold on mica at substrate temperatures ranging from -150 °C to 400 °C, thin films exhibit an increasing grain size together with a grain flattening as the substrate temperature increases (Buchholz *et al.*, 1991). Atomically smooth plateaus ranging from 60 nm to 100 nm lateral extension were also observed on the surface (Vancea *et al.*, 1989). Flame annealing of epitaxial thin gold films obtained after heating the mica substrate at 380 °C produces grains up to 360nm in size (Dishner *et al.*, 1998). Some researchers have claimed that the imperfect cleavage of mica in air promotes regions with different defect characteristics and densities during growth (Salmeron *et al.*, 1987).

For practical electronic uses, the Si(100) substrate is preferable to mica. In studies using single-crystal Si(100) as substrates, it has been reported that rough surfaces are obtained following gold deposition. A "Hill-like" landscape was observed with an average height variation of about 16 nm (Vancea *et al.*, 1989). Large crystallites of about 500 nm in size with the [011] direction of the crystallites parallel to the [011] direction of the silicon were also reported (Mathieu *et al.*, 1988). According to Golan *et al.* (1992), evaporation of gold onto Si[100] results in non-structured thin films, and annealing at 250 °C has the effect of grain enlargement. In addition, as soon as Au-Si junctions are formed, silicon atoms can out-diffuse at room temperature (RT) to the surface of the gold layers (Bishop & Riviére, 1969). This implies an extensive interfacial reaction which breaks the covalent Si-Si bonds and provides free Si atoms. Furthermore, because Au is very reactive and miscible with Si, a multitude of Au_xSi_y compounds is produced by thermal reactions (Marchal *et al.*, 1980; Tsaur & Mayer, 1981; von Allmen *et al.*, 1980). First investigations proposed that the nucleation of gold on silicon is based upon the formation of a gold silicide layer on the surface (Buchholz *et al.*, 1991; Salmeron *et al.*, 1987). It was confirmed by Ma and Allen (Ma & Allen, 1993) that the Au/Si(100) interface deposited at 80 °C is not abrupt and contains a disordered Si-rich Au-Si alloy decorated with pure Au nanocrystallites. Recent reports suggest that silicide is already formed after depositing gold on silicon at RT and it transforms after annealing at 200 °C for 20 to 40 min (Chang *et al.*, 2004).

Obtaining epitaxial Au(111) on SiO_2 is even more useful in micro- and nano-electronics (for instance when the substrate is used as a transistor gate). However, the main drawback of this substrate is that the formation of microcrystals with the same crystallographic orientation is extremely difficult to achieve during deposition. This is because most of the surface is amorphous, containing only small amounts of fcc SiO_2 crystallites oriented in the [100] plane direction. Most post annealing studies of Au/Si thin films report annealing temperatures up to 250 °C for almost 5 min (Mancini & Rimini, 1970) and 180 min (Golan *et al.*, 1992) which are below the eutectic point of the Au-Si system which is 363 °C for a Au(80.5%):Si(19.5%) composition (this is many hundreds of degrees below the melting point of its individual pure components Au (1063 °C) and Si(1412 °C) (Massalski, 1987; R.Castanet *et al.*, 1978)). Comprehensive studies of the effect of thermal post-annealing of Au thin films over Si-based substrates for different annealing temperatures above the eutectic point of Au-Si have not been performed yet. Such studies might help to understand the crystallization and morphology evolution of this system with temperature. In this work we have studied the crystallization and surface morphology of gold growth at RT on SiO_2 substrates after ex-situ annealing: from 300 °C to 900 °C for 3 hours (by furnace annealing) and its comparison to temperatures applied for a short duration of time from 0.5 min to 5 min (by flame annealing). We have found that after annealing at temperatures higher than the eutectic point of the Au/Si system, crystallized islands of different shapes and sizes were formed on the surface of the samples by both annealing techniques. We explain the islands evolution with temperature and time of annealing by means of surface diffusion.

3.2 Experimental

Gold was evaporated on comertial polished $SiO_2(2\mu m)/Si(100)$ substrates using an Edwards 306 evaporator system with a base pressure of 10^{-7}mbar. The substrates (1×2 cm^2 areas) were cleaned with acetone, isopropyl alcohol and ultrasound following standard procedure before deposition. Small Au pellets (99.999% purity) were evaporated from a tungsten boat and substrates were located 10 cm above this source. The rate of evaporation was maintained at 0.1 nm/s and the thickness of gold was measured by a quartz crystal microbalance located next to the sample. In contrast to other reports in which substrates are heated up to 500 °C during sputtering deposition (Chang *et al.*, 2004), in the present work the substrates were intentionally kept at RT during evaporation in order to characterize only post-annealing effects on the samples. Samples consisted of 40 nm thick Au films on polished SiO2/Si surfaces (Au/SiO2). A thin layer of Ti (5 nm) was used as adhesion promoter between Au and the substrates. It was expected that this interface would also avoid the out-diffusion of Si to the Au layer.

Post-deposition thermal treatment of the samples was carried out in two ways: furnace annealing and flame annealing. The first technique consisted in annealing the sample for 3 hours in a tubular oven (LENTON LTF-PTF Model 16/610) in air flow at different temperatures up to 900 °C (Figure 3.1). The increment rate of the temperature was 1 °C/min. In order to study the effects of annealing, the maximum selected temperatures where chosen in the range of 300 °C - 900 °C and it was kept constant within 1 °C for 3 hours, after which the samples were allowed to cool down slowly (1.4 °C/min) so as to minimize any stress which might develop during cooling. Flame annealing consisted in placing a sample horizontally over the conical blue zone of a flame generated by a propane torch until the surface color of the sample changed. The thin film was then rapidly quenched by immersing it into a beaker of methanol and drying it in a stream of nitrogen. Figure 3.1(b) is a representation (not to scale) of the temperature vs. time sensed by a NiCr-Ni (type K) thermocouple positioned 2 - 3 mm from the samples during flame annealing. According to the figure, after 30 s, the heating rate changes from 14 °C/s to 0.25 °C/s. Samples were annealed for 30 s in order to avoid the initial stages of heating transmission through the substrate. In total, four samples were flame annealed for 30 s, 1 min, 2 min and 5 min, respectively. The maximum temperature they supported during flame annealing was in the range of 930 °C - 1067 °C. Here we denote the highest temperature measured by the thermocouple as the annealing temperature. The temperature fluctuation during flame annealing was around ±3 °C.

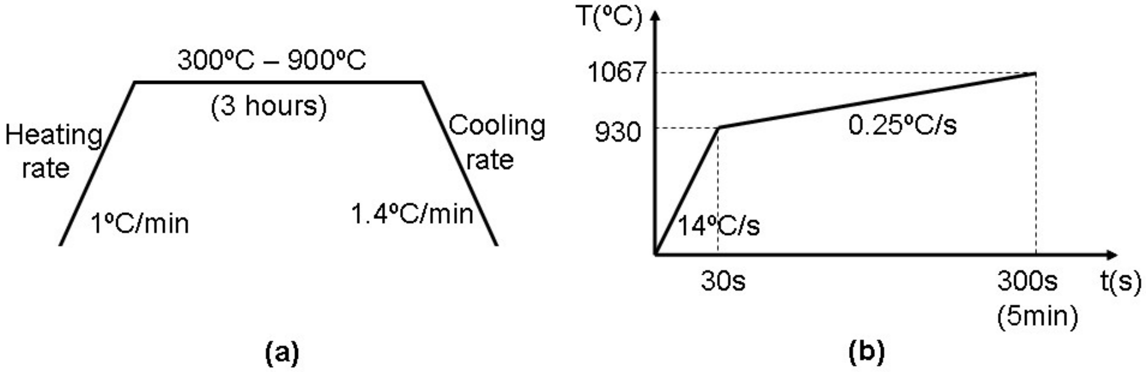

Figure 3.1: Variation of the temperatures during the heat treatment (not to scale) for (a) furnace annealing and (b) flame annealing.

Crystallization of the samples after annealing was studied by X-ray diffraction (XRD). The data were collected from 25° to 60° (0.02° step) using a powder universal diffractometer, Rigaku HGZ (Cu Kα radiation). Crystallites' mean sizes were calculated with Scherrer's formula (Cullity, 2001):

$$D = \frac{0.916\lambda}{\beta_{hkl} cos\theta_{hkl}} \tag{3.1}$$

Where λ is the wavelength of the X-rays (1.54060 Å), θ_{hkl} is the Bragg angle and β_{hkl} is the pure-diffraction line broadening (in radians), which can be easily found by measuring the full width at half maximum (FWHM) of the *hkl* reflection. Morphology analyses were done with the help of an atomic force microscope (AFM, Nanoscope Dimension 3100, Digital Instrument) in tapping-mode scans.

Scanning electron micrographs were taken only over some samples, where the morphology of the annealed thin films differed significantly from the pristine ones. The analysis was performed using a scanning electron microscope (SEM-XL30 SFEG).

3.3 Results and discussions

The XRD analysis is presented in Figure 3.2. As shown, after evaporation (raw sample) the Au layer has some crystallites oriented in the [111] direction but most of the sample is amorphous. Some peaks belonging to the Si-based substrate appear, and the main reflection of Ti (around 38.402°) is hidden in the background of the spectra and thus negligible. Gold silicides were not found as in the case of Au on Si(100) (Chang *et al.*, 2004; Valladares *et al.*, 2010a). Growth of a silicide in thin metal films over silicon substrates occurs by diffusion across the interface. The presence of an oxide layer at the interface is known to hinder the diffusion across the interface (Sekar *et al.*, 1992, 1993). Since our samples consisted of gold layers on 2 μm thick SiO_2 substrates with a thin Ti interface layer, no gold silicide was expected to be found. After furnace annealing at 300 °C for 3 hours, the (111) texture of the gold layer increases and the reflections belonging to the Si substrate are less visible (Figure 3.2(a)). After annealing the sample for 3 hours at 350 °C, which is around 10 °C below the eutectic point of the Au-Si system, the [211] reflection belonging to the substrate is not visible any more and it almost disappears in the background of the spectrum. This means that more Au grains in the sample are crystallized in the [111] direction and hence its respective reflection becomes higher in the spectra. Nevertheless, the shape of the background spectra reveals that the sample is still amorphous and that this annealing temperature is not enough to complete the crystallization. Annealing the sample over the eutectic point, at 400 °C, leads to a high (111) crystallization of the thin gold film, which means that the epitaxial temperature of Au on silicon is somewhere in the interval of 350 °C - 400 °C. Hence it is reasonable to suggest that the epitaxial temperature is in the region of 363 °C (the eutectic point). This epitaxial temperature is lower than others found for different substrates (e.g. 450 °C for gold-mica (Pashley, 1956)). Further annealing up to temperatures as high as 900 °C for the same duration produces even higher crystallization of the thin Au film and some interesting changes in the morphology are found, as will be discussed below. Eventually, at 900 °C almost all the Au is crystallized in the [111] direction with a completely flat background spectrum. As mentioned above, rapid annealing of the samples was achieved by flame annealing. Figure 3.2(b) shows that flame annealing the sample 30 s also reduces considerably the Si(211) reflection in the spectra. Nevertheless the shape of the background spectrum and the (211) reflection belonging to the Si substrate reveal that, this time, long annealing duration is not enough to complete the crystallization. Despite the fact that after 30 s the highest temperature was around 930 °C, the epitaxial temperature criterion is not followed here due to the rapid rate of heating. If the sample is annealed for 1 min, the Si(211) reflection belonging to the substrate almost disappears. Most of the Au grains in the sample are crystallized and hence the Au(111) reflection in the XRD spectra becomes bigger and sharper. Therefore, epitaxial formation of gold is visible from 1min onwards and there are only small changes if the sample is annealed up to 5 min. This is because during that period of time the temperatures vary less than 100 °C at a slow heating rate of 0.25 °C/s.

In general, from Figure 3.2 we can deduce that after both furnace and flame annealing, Au thin films on SiO_2 substrates can be crystallized despite most of the substrate being amorphous and containing only a small amount of SiO_2 crystallites. Furthermore, the differences between the cubic cell parameters are around 4.08 Å for gold (PDF No 89-3697), 4.06 Å for Ti (PDF No 88-2321) and 4.52 Å for SiO_2 crystals (PDF No 89-3609). Annealing overcomes these mismatches by arranging the Au layers in the [111] direction and changing the morphology of the surface as will be discussed next. The fact that gold, Ti and SiO_2 have cubic structures seems to be the only condition for both elements to allow epitaxial growth. Both slow and rapid annealing gives negligible background in the XRD spectra and hence clean and complete crystallization. It is concluded from here that crystallization of gold strongly depends on the temperature even if the sample is annealed rapidly. Despite the fact that flame annealing does not follow the epitaxial temperature criterion due to the heating rate, crystallization of the Au layer can be easily reached after annealing for a few seconds.

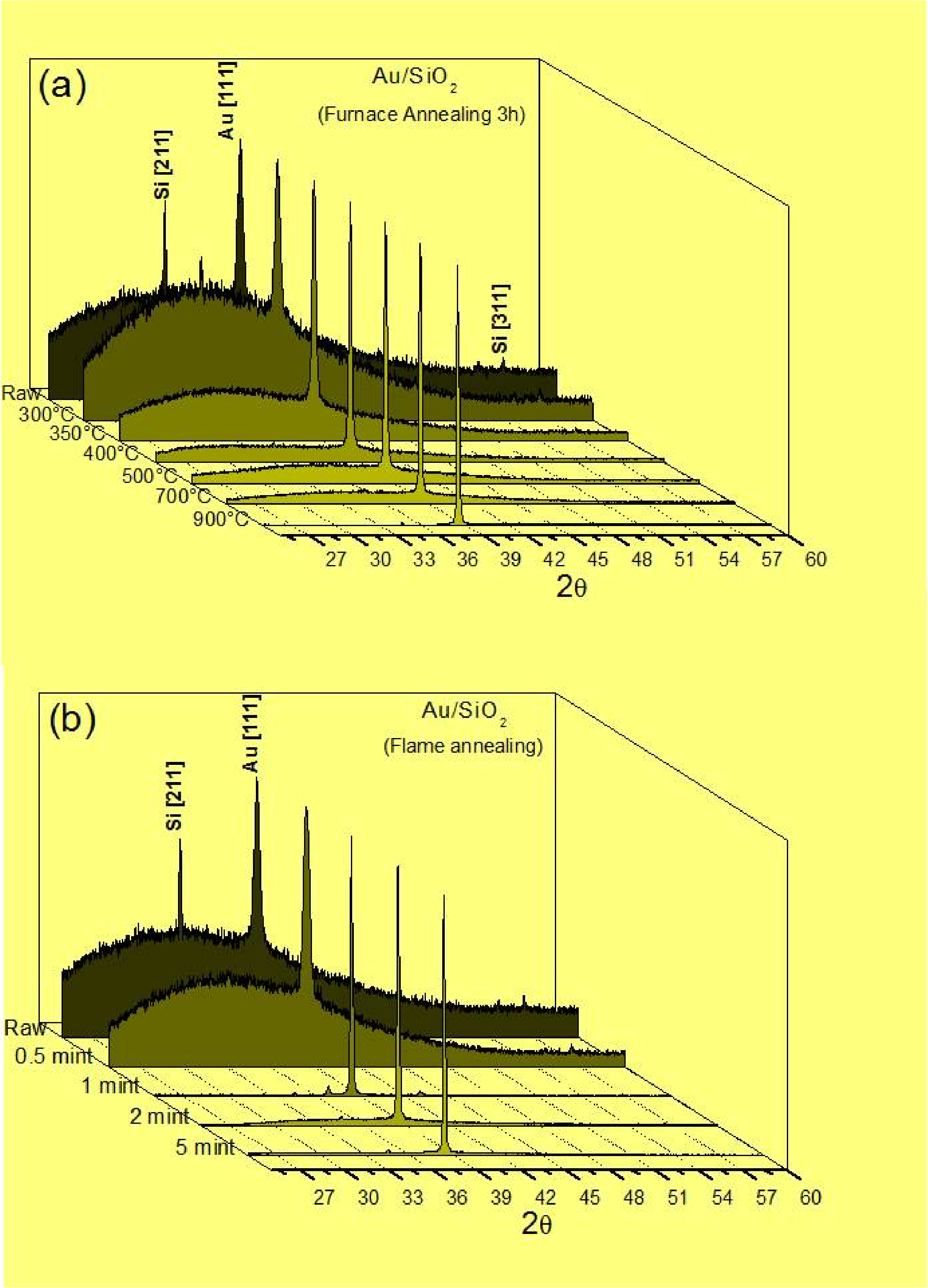

Figure 3.2: XRD analysis of Au/SiO_2 after (a) 3 hours furnace annealing and (b) flame annealing. In both figures the intensity axes are normalized.

The AFM scans of the as-deposited (raw) samples are smooth without any discernible morphological feature. Scans over areas of 100 μm^2 of Au/SiO$_2$ samples after furnace and flame annealing are presented in Figures 3.3 and 3.4, respectively. Their respective cross sections, showing the variation of the surface height along the white dashed lines, are plotted in the corresponding topographic images. As seen in Figure 3.3, after 3 hours furnace annealing at 300 °C clusters appear in some areas, while the surrounding surface is still smooth. The situation changes when the sample is annealed at 400 °C. The surface becomes rough and hillocks of gold cover almost all of the thin film. Its respective cross-section, along the white dashed line, indicates that the hillocks have different heights and vary from 50 nm to 150 nm. Annealing the sample at 500 °C under the same conditions leads to more agglomeration of gold islands without any specific shape. According to the cross-section, the height of the islands becomes almost identical (100 nm). After further annealing at 700 °C, it can be seen that the borders of the clusters are rounded, the distances between clusters increase and the borders are better distinguished. The surface image and the cross-section indicate that apparently there was gold diffusion on the surface of the sample, and the islands' average height increases to 250 nm. Annealing up to 900 °C gives a better resolution of the islands; their shape is almost the same, and although they are not equally distributed over the surface, the separation between them ranges from 0.5 μm to 3 μm. The average height this time increases up to 300 nm. Measuring one isolated island reveals that they have flat terraces. By looking at the surfaces of the samples through an optical microscope (images not shown here), the islands are golden in colour, whereas the background is grey (the typical colour of the SiO$_2$ substrate). Therefore migration from the strained gold to the islands has occurred.

Figure 3.4 shows the surface evolution of the sample after flame annealing. According to the figure, after 30 seconds of flame annealing there appear clusters randomly dispersed over the surface of the sample; the surrounding surface is still smooth. The cross-section along the white dashed line indicates that the heights of the measured clusters are similar (35 nm). The formed clusters have sharp tops. The situation changes drastically when the sample is annealed for 1 min. The surface becomes rough because almost the entire surface contains high islands.

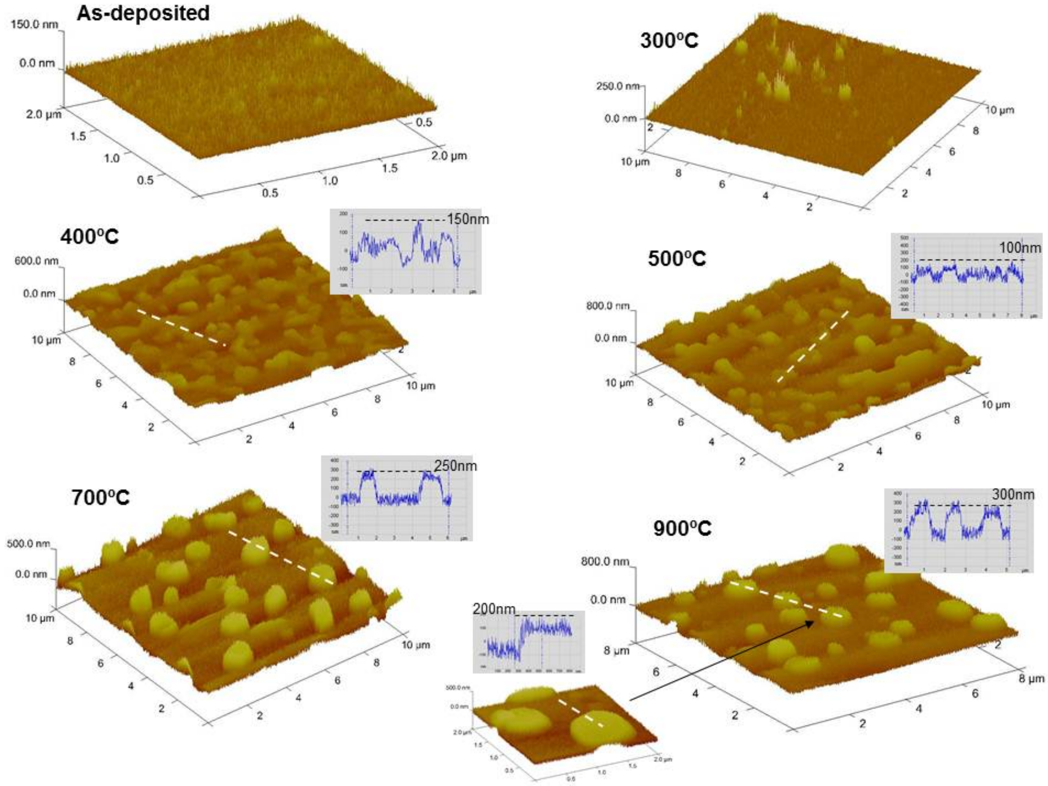

Figure 3.3: AFM analysis of Au(40nm)/SiO2 after furnace annealing.

It is reasonable to say that during the time interval between 0.5 min to 1 min more clusters appear on the surface and rapidly grow by forming the presented landscape. The respective cross-section, along the white dashed line indicates that the islands have different heights ranging from 100 nm to 150 nm and have rounded tops. Annealing the sample for 2 min leads to more agglomeration of gold islands without any specific shape. According to the cross-section, the height of the islands ranges from 100 nm to 150 nm as in the previous case, but their tops are flatter. After further annealing up to 5 min the islands grow even more and reach different heights. The cross-section indicates that some islands reach up to 300 nm height. Flat terraces up to 1 μm size were also found on the tops. The maximum islands heights reached during the different intervals shown in this figure are plotted in Figure 3.6(b) (see page 49) for different flame annealing times.

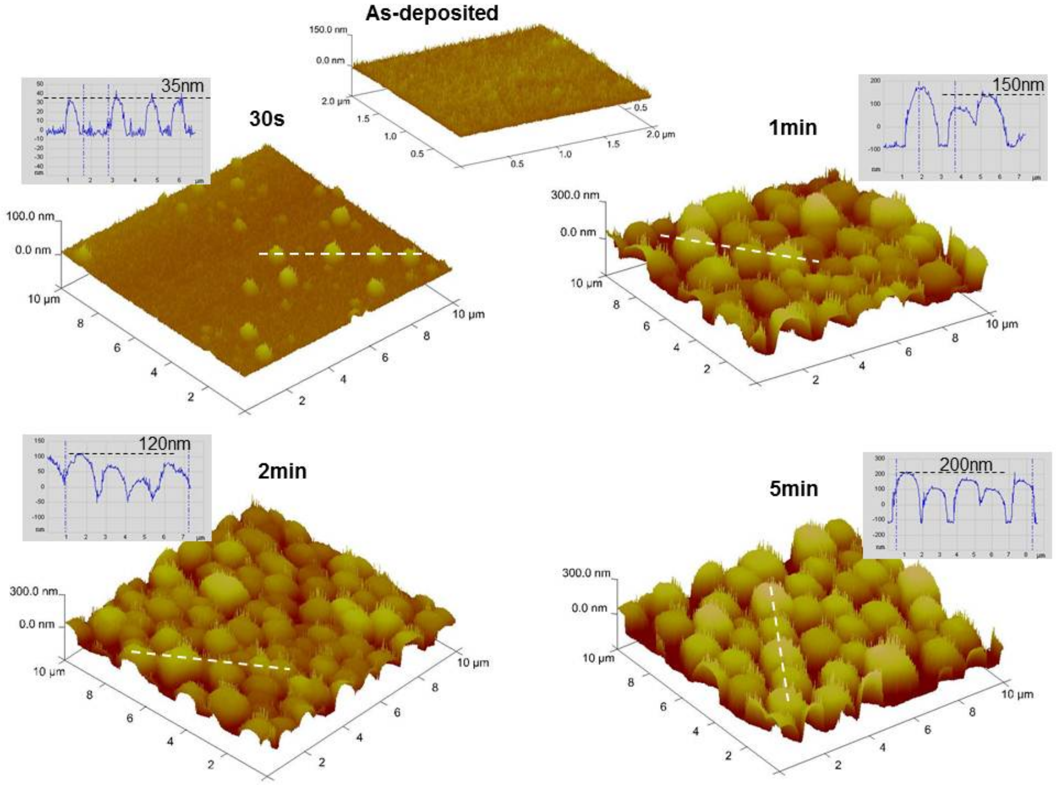

Figure 3.4: AFM analysis of the sample Au(40nm)/SiO$_2$ after flame annealing.

Distances between islands can be better distinguished in SEM images. Figure 3.5 shows some SEM micrographs of the annealed samples. Figure 3.5(a) confirms that after furnace annealing at 500 °C for 3 hours gold islands of different shapes and sizes are formed. Diameters of these islands vary from tens to thousands of nm. Islands with different shapes have also been observed after annealing Au/Si(100) samples (Chen & Chen, 1996; Valladares *et al.*, 2010a). Figure 3.5(b) shows that after furnace annealing at 900 °C they have hexagonal-shaped borders with planar terraces and they are randomly orientated over the substrate. Figures 3.5(c) and 3.5(d) correspond to samples after flame annealing for 1 min and 2 min, respectively. It can be seen that the islands are not as close together as apparent from the AFM figures; this is because the AFM scans were done in tapping mode. The hexagonal border shapes of the islands are better resolved after 2 min than after 1 min flame annealing. However they are rounder than their furnace annealing counterparts. Table 3.1 provides information about the height of the formed gold island and its roughness as measured by AFM.

Table 3.1: Height of the gold islands and roughness (rms in nm) detected by AFM.

	Furnace Annealing	
Temperature	**Height range (nm)**	**Roughness (rms in nm)**
300 °C	50 -100	8.3
400 °C	50 - 150	16.5
500 °C	100	29.4
700 °C	200 - 250	37
900 °C	300	56.5
	Flame annealing	
Time	**Height range (nm)**	**Roughness (rms in nm)**
0.5 min	35	4.3
1 min	100 - 150	6.6
2 min	100 - 150	5.4
5 min	200 - 300	3.4

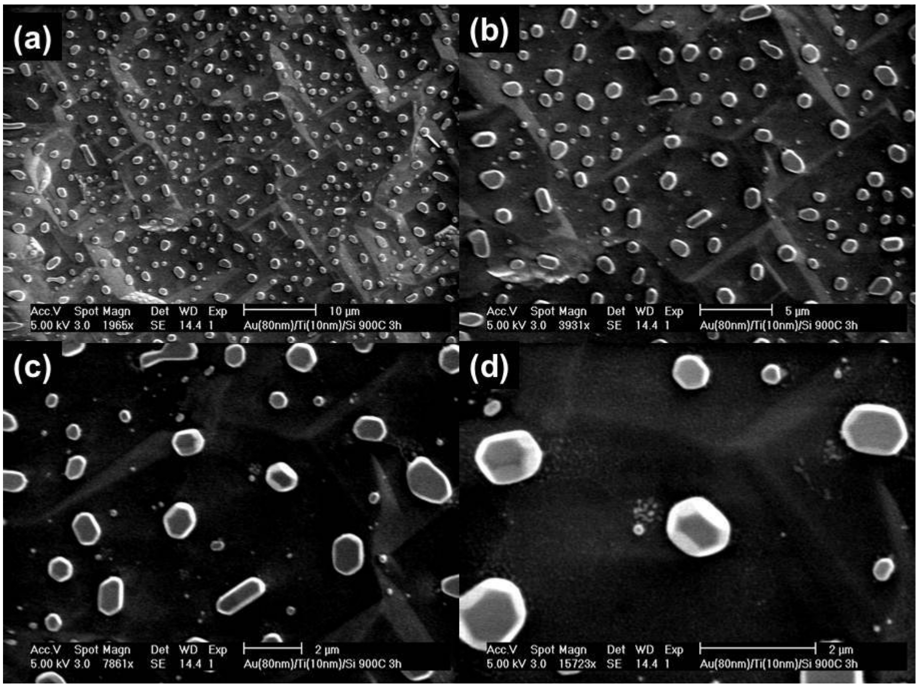

Figure 3.5: SEM micrograph of Au/SiO_2 samples after 3 hours furnace annealing at (a) 500 °C, (b) 900 °C and after flame annealing for (c) 1 min and (d) 2 min.

The initial stages of the island formation are still unclear. Some explanations relate it to the out-diffusion of Si into the Au film to increase the formation of Au_XSi_Y. The nucleation and the increasing amount of these gold silicides is because Au induces a breaking of the underlying Si bonds. During annealing, adatoms of gold agglomerate on top of these silicides and grow by forming islands (Bishop & Riviére, 1969; Chang *et al.*, 2004). However, this case is not applicable here because, as mentioned before, our samples consisted of gold layers on 2 μm thick SiO_2 substrates with a thin Ti interface layer and the formation of silicides has not been detected in the XRD. In our case, the mismatch between the cell parameters of the Au, Ti interlayer and SiO_2 produces a strained Au layer during evaporation. Strain relaxation at higher temperatures would be responsible for the initial stages of the cluster formation. Above the eutectic point the layer melts. The melting starts most likely from the grain boundaries and from the interface. Moreover, during the quenching of the sample, Au atoms should crystallize from the liquid, when the temperature reaches the liquid curve in the phase diagram. This is done by growing the existing solid gold grains. As the temperature continues to fall, more and more Au crystallizes. Eventually, when the temperature drops to the eutectic point, the liquid crystallizes with the characteristic structure of lamellae islands. Nevertheless hexagonally shaped islands are formed, if the sample is annealed well above the eutectic temperature. Probably it is caused by some relaxation which appears in the SiO_2 substrate and was not observed at lower temperatures due to the differences in the latent heat of fusion between Si (50.21 kJ/mol), Ti (14.15 kJ/mol)) and Au (12.55 kJ/mol).

The mean crystallite diameter (D) calculated by Sherrer's formula (Equation 3.1) for the raw sample and samples after furnace (DT) and flame annealing (Dt) are shown in Figure 3.6. According to the figure, the mean crystallite size of the pristine sample is around 25 nm. This is quite similar to that obtained after evaporating gold over unpolished Si(100) substrates (Valladares *et al.*, 2010a). After annealing, the crystallites grow monotonically with the rate decreasing towards higher temperatures (Figure 3.6(a)) and as the time of annealing increases (Figure 3.6(b)). Table 3.2 provides information about the mean crystallite diameter obtained from the XRD and the mean diameters of the formed islands scanned by AFM and visualized by SEM. The higher values in the AFM case are due to

Table 3.2: Mean crystallite diameters obtained by XRD and mean diameters of the islands scanned by AFM and visualized by SEM. NT indicates that measurements have not been performed and L indicates the lamellae shape of the islands.

Furnace Annealing			
Temperature (°C)	**XRD (nm)**	**AFM (μm)**	**SEM (μm)**
300	25	0.3	NT
400	68	L	L
500	73	1	L and 1
700	87	2	NT
900	88	2.5	1
Flame annealing			
Time (min)	**XRD (nm)**	**AFM (μm)**	**SEM (μm)**
0.5 min	25	0.7	NT
1 min	89	1.5	0.5
2 min	88	1.5	0.5
5 min	94	1.5	0.3

the gap distance between the cantilever and the border of the islands caused in typical AFM scans.

The mean crystallite diameter follows the empirical equations given below after furnace and flame annealing respectively:

$$D_T = 0.85 \times T^{n_T} \tag{3.2}$$

$$D_T = 64 \times t^{n_t} \tag{3.3}$$

where T is the furnace annealing temperature, t the flame annealing time, n_T the temperature exponent (≈0.7) and n_t the time exponent (≈0.3). The latest value is slightly similar to that reported by other authors for Au deposited onto Formvar substrates (Mancini & Rimini, 1970). According to them, this value suggests that the growth mechanism is grain-boundary migration.

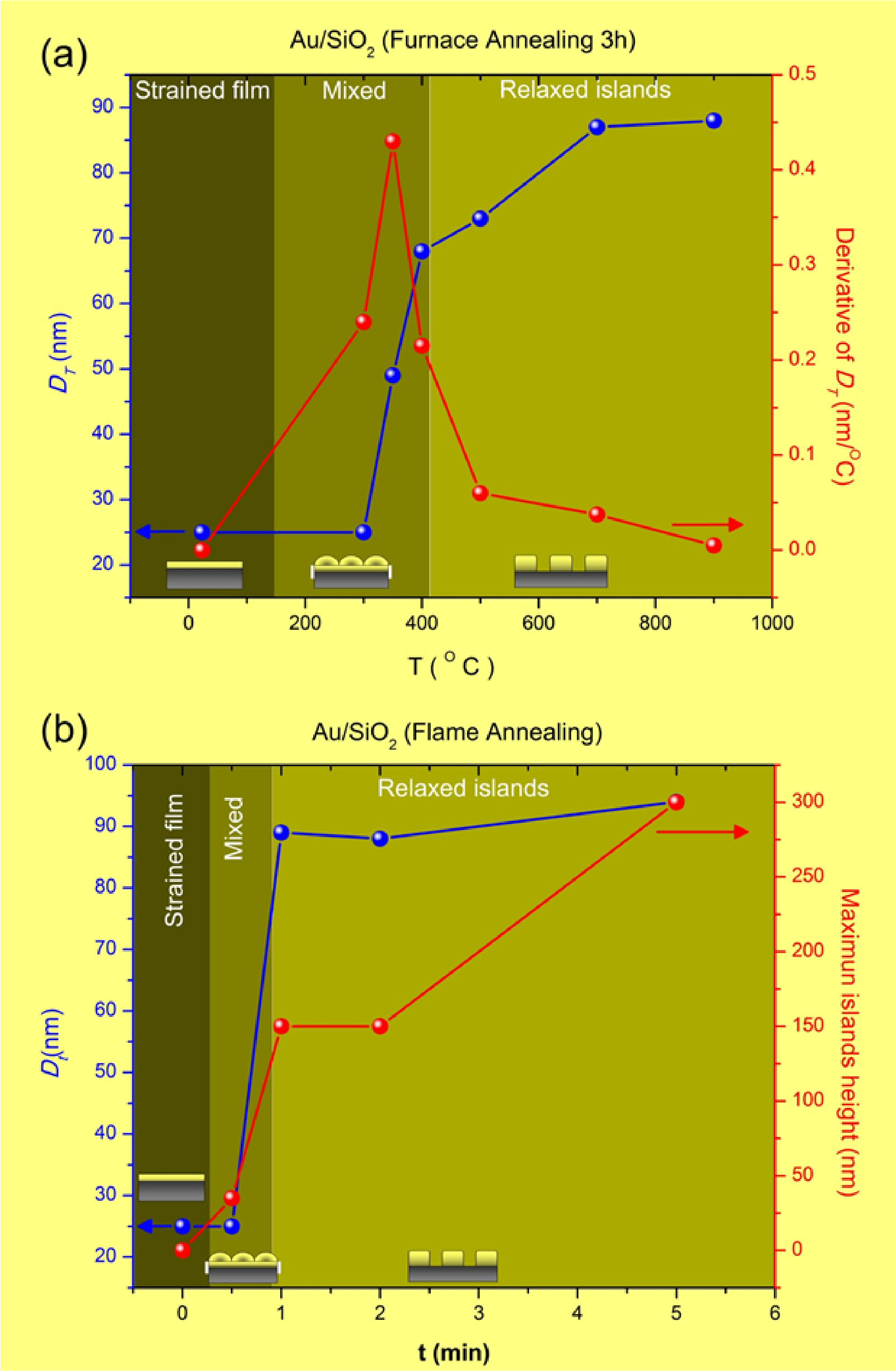

Figure 3.6: Crystallites' mean diameters of Au/SiO_2 following (a) furnace annealing and (b) flame annealing.

It is worth remembering that the principal differences between both types of annealing technique presented here are the heating (cooling) rate and the time of annealing. Furnace annealing is slower and provides more control of thermal conditions than flame annealing. Regarding the final surfaces, both types of annealing provide epitaxial gold islands with maximum mean crystallite diameters of around 90 nm. The annealing history seems to be more important for the final shape of the clusters. Because slow annealing rates are achieved by the furnace technique, the growth rate (G) can be related to the derivative of D_T (Figure 3.6(a)). From the information given by XRD, AFM and SEM, we can deduce the morphology evolution of the sample surface during annealing. Three main events can be identified, as seen in Figure 3.6. The exact point at which each event happens is difficult to determine precisely because changes occur progressively. The changes of colors between each field in the figure are rough estimates for each transition. The situation is harder to predict for the flame annealing than for the furnace annealing. Transitions during flame annealing occur abruptly due to the fast heating rates. Initially after evaporation the surface consists of a strained and amorphous Au layer which crystallizes after annealing. The slow increase of D in the early annealing stages of growth by both techniques may be due to the highly disordered initial structure (excess point defects, dislocations, lattice strain, etc.) which is present in a thin film after deposition. Gold-island nucleation sites may be formed in those disordered points facilitated by the relaxation of the strained Au layer, when the temperature and time of annealing increases. The clusters coexist with the gold layer substrate and they grow in size with the annealing temperature and time (mixed zones in the figure). The maximum inflection point of the derivative of D_T is close to the eutectic temperature of the Au/Si system (363 °C). This means that the nucleation rate is highest around this temperature. Annealing the sample at higher temperatures produces more gold that diffuses from the substrate to the clusters to form separated islands of different shapes (relaxed islands zones in the figure). Well above the eutectic temperature, the relaxed islands have hexagonally shaped borders. The activation energy corresponding to grain-boundary displacement above the eutectic temperature has been obtained by fitting the downward trend part of the derivative of D_T with the following equation (Mancini & Rimini, 1970):

$$G = G_0 \exp\left(\frac{-|Q|}{k_B T}\right) \tag{3.4}$$

where G_0 is the rate constant, $|Q|$ is the activation energy, T the absolute temperature and k_B the Boltzmann constant (8.617343×10^{-5} eV/K). This equation describes, approximately, the rate of grain-boundary displacement; G_0 is proportional to the driving force and is related to the entropy changes (Amelinckx & Dekeyser, 1969). The free energy of activation for grain-boundary migration ($|Q|$) derived here is 0.2 eV. This value is double that calculated when Au is deposited on a (100) textured silicon substrate (≈0.09 eV) (Valladares *et al.*, 2010a). Therefore the texture of the substrate changes the mechanism of diffusion and growth of crystallites during annealing of the Au/Si system.

The fact that above 360 °C the surface morphology transforms to gold islands spread over the SiO_2 substrate is a good indication for obtaining an epitaxial Au(111) layer covering the whole of the SiO_2 substrate. This could be achieved by simply annealing the sample at temperatures below 360 °C. If the furnace annealing technique as presented here is used for this purpose, suitable temperatures are in the range of 300 °C - 310 °C, just before D_T changes drastically and islands start to nucleate (Figure 3.6(a)). However it is important to remember that the total crystallization of the strained Au layer is not obtained at that temperature range (see Figure 3.2(a) in page 41). The situation is different if flame annealing is used for the same purpose. Despite being much faster and easier to perform than the previous technique, it allows less control of the temperature. An epitaxial Au(111) layer, covering almost all the surface, could be achieved by annealing the sample for a few seconds (less than 30 s in which D_t changes drastically (Figure 3.6(b)). In the furnace annealing technique the (111) crystallinity of the strained Au film increases but complete crystallization is not obtained (see Figure 3.2(b) on page 41). Recently there has been significant interest in self-assembly of organic molecules on annealed Au(111) layers (Rundqvist *et al.*, 2006).

3.4 Conclusions

Thin gold films on SiO_2 substrates can be crystallized after both furnace and flame annealing despite most of the substrate being amorphous and containing only a small amount of SiO_2 crystallites. Annealing overcomes this by arranging the Au layers in the [111] direction and by changing the morphology of the surface. Both slow and rapid annealing give good background in the XRD spectra indicating clean and complete crystallization, which depends more on the temperature than on the time of annealing. The epitaxial temperature for the Au/SiO_2 system should be around 360 °C. Annealing also forms crystalline gold islands on the Au/SiO_2 surface. The mismatch between the cell parameters produces a strained layer of Au during evaporation. Strain relaxation at higher temperatures is believed to be responsible for the initial stages of the cluster formation. Gold island nucleation sites may be formed at disordered points on the surface such as excess point defects, dislocations, lattice strain, etc.; they become islands when the temperature and time of annealing increase. The highest growth rate of crystallites is around the epitaxial temperature. Above this point, the melting starts most likely from grain boundaries and the interface. It produces more gold diffusing from the strained Au layer to the clusters to increase the distance between the islands and modify their shapes. Far above the epitaxial temperature, the relaxed islands have hexagonally shaped borders. The mean crystallite diameters grow with time and temperature of annealing following a polynomial trend. However, this trend ends when the crystallites reach a maximum mean size of around 90 nm. The free energy of activation for grain-boundary migration above the eutectic temperature is 0.2 eV. This value is nearly double the free energy calculated when Au is deposited on the (100) silicon substrate (which is $\approx$0.09 eV). Therefore the type of silicon substrate changes the mechanism of diffusion and growth of crystallites during annealing of the Au/Si system. Epitaxial Au(111) layers without formation of islands can be achieved by furnace annealing in the interval between 300 °C - 310 °C and by flame annealing for a few seconds (<0.5 min).

Chapter 4

Thin copper films: Thermal oxidation

In this chapter, the crystallization and electrical resistivity of the formed oxides in a Cu/SiO_2/Si thin film are studied after thermal oxidation by ex-situ annealing at different temperatures up to 1000 °C. Upon increasing the annealing temperature, the phase evolution $Cu \rightarrow Cu + Cu_2O \rightarrow Cu_2O \rightarrow Cu_2O + CuO \rightarrow CuO$ was detected from the XRD. Pure Cu_2O films are obtained at 200 °C, whereas uniform CuO films without structural surface defects such as terraces, kinks, porosity or cracks are obtained in the temperature range 300 - 550 °C. In both oxides, crystallization improves with annealing temperature. A resistivity phase diagram, which is obtained from the current-voltage response, is presented here. The resistivity was expected to increase linearly as a function of the annealing temperature due to evolution of oxides. However, anomalous decreases are observed at different temperature ranges, this may be related to the improvement of the crystallization and crystallite size when the temperature increases.

4.1 Introduction

Copper is used in a very broad range of electronics applications due to its good electrical conductivity, low cost and non-toxicity (Jing *et al.*, 2008). However, there are still obstacles which limit the use of copper in nano-electronics, mainly because of (i) its diffusion into commonly used silicon substrates and (ii) its ease of oxidation even under a vacuum atmosphere. In the first case, it is widely known that copper slowly diffuses in contact with Si substrates resulting in line-to-line leakages or electrical shorting of electronic devices (Nagao *et al.*, 2003). The chemical physics underlying this diffusion is currently under intense study (Wang, 1994; Willis & Lang, 2004). To slow the diffusion, SiO_2 substrates are commonly used. SiO_2 is an insulator easily produced by thermal oxidation of Si and has great stability and good adherence to copper and other noble metals (Benouattas *et al.*, 2000; Ferullo *et al.*, 2006; Xu *et al.*, 1993). Regarding oxide formation, like other noble metals, thin semiconducting oxide layers easily form on copper surfaces upon contact with air. The two principal types of oxides formed on copper films are cuprous oxide (Cu_2O, cuprite) and cupric oxide (CuO, tenorite) (Neumann *et al.*, 1984; Schramm *et al.*, 2005). Cu_2O is a p-type semiconductor with cubic crystalline structure (a = 4.27 Å) and energy gap 2.0 - 2.2 eV (Marabelli *et al.*, 1995). Nowadays thin Cu_2O films are intensively investigated due to their potential applications in spintronics (Pearton *et al.*, 2004), catalysis (Ramírez-Ortíz *et al.*, 2001) and solar cells (Fernando & Wetthasinghe, 2000; Han & Tao, 2009a). In contrast, CuO is a p-type semiconductor with monoclinic crystalline structure and cell parameters a = 4.6837 Å, b = 3.4226 Å, c = 5.1288 Å and $\beta = 99.54^{o}$. Its energy gap is in the range 1.21 - 1.51 eV. This is an attractive system for many researchers due to its photoconductive and photo-thermal applications (Koffyberg & Benko, 1982) and for studies of the transport mechanism in high-temperature CuO-based superconductors (Zheng *et al.*, 2001). Although the formation of these two types of oxide is still considered the principal obstacle in using thin copper films in nano-electronics, they have promising applications in large-area electronics, especially when the oxides are high purity and epitaxially grown. For example, for solar-cell applications, the literature reports different techniques for the fabrication of crystalline thin copper oxide films. Among them, molecular beam epitaxy (Muthe *et al.*, 1998), spray-pyrolysis deposition (Kosugi & Kaneko, 1998), anodic oxidation (Roos *et al.*, 1983), electrochemical deposition (Mukhopadhyay *et al.*, 1992; Wang & Tao, 2007), reactive sputtering (Drobny & Pulfrey, 1979; Izhizuka *et al.*, 2001; Ogale *et al.*, 1992) and chemical oxidation (Fujinaka & Berezin, 1983) are expensive techniques, which require special conditions and usually result in mixed phases. The simplest and cheapest technique to achieve single-phase copper oxide films is thermal oxidation (Akkari *et al.*, 2007; Figueiredo *et al.*, 2008, 2009). In this technique, thin copper oxide films are easily obtained by ex-situ annealing of thin copper films. The desired type of oxide can be controlled by the annealing temperature. In this chapter, the oxidation evolution of thin copper films by thermal oxidation is studied. Specifically, the phase formation, crystallization and electrical resistivity of the different types of oxide formed on Cu/SiO_2 thin films following annealing at different temperatures up to 1000 °C are investigated.

4.2 Experimental

Copper was evaporated on polished SiO_2/Si substrates using an *EDWARDS* 306 evaporator system at a base pressure of 10^{-7} mbar. Commonly, SiO_2(60 nm)/Si substrates are used when depositing copper for micro- and nano-electronics applications. However in this work, SiO_2 (2 μm)/Si were used, because a thick SiO_2 interlayer slows the diffusion of copper into the silicon substrate and it prevents possible current leakage during the electrical characterization. Moreover, with this substrate, the use of adhesion promoters such as chromium or titanium is avoided and thus the formation of alloys during annealing at high temperatures is also avoided. The SiO_2 (2 μm)/Si substrates were uniformly cut into 1×2 cm^2 pieces and cleaned with acetone, isopropyl alcohol (IPA) and ultrasound following a standard procedure. Small Cu pellets (99.999 % purity) were then evaporated from a tungsten crucible and the substrates were located 10 cm above this source. The rate of evaporation was maintained at 0.1 nm/s and the thickness of the deposited copper was measured by a quartz crystal microbalance located next to the sample. During the deposition process the substrates were actively maintained at room temperature in order to characterize post-annealing oxide formation on the samples. The pristine samples consisted of Cu(100 nm)/SiO_2(2 μm)/Si structures. The thermal oxidation was carried out by annealing the samples in a tubular oven (*LENTON LTF-PTF* model 16/610) in air atmosphere, at different temperatures from 150 °C to 1000 °C similar to annealing thin gold films (see Chapter 3 and our previous publications (Valladares *et al.*, 2009a, 2010a)). The heating rate was set to 10 °C/min. Once the maximum desired temperature was reached, it was kept for 3 hours to allow free diffusion of the copper atoms on the surface. Next, the quenching rate was set to 1.4 °C/min so as to minimize possible stresses in the thin films.

Phase formation and surface crystallization were analyzed by X-ray Diffraction (XRD) using a powder universal diffractometer, *Bruker AXS* model *D8 FOCUS* (Cu-$K_{\alpha 1}$ radiation), the step size was 0.02 °(2θ), and the counting time for each point was 4 s. The average sizes of the crystallites were estimated from the main reflections of the XRD using the Debye-Scherrer formula (see Equation 3.1 in page 38) and neglecting peak broadening caused by residual stresses in the thin films. The surface morphology was observed through a scanning electron microscope (SEM) *Philips XL-30.* Before SEM analysis, most of the surfaces were carefully scratched with the help of a needle in order to reveal part of the SiO_2 and to distinguish the thin copper oxide films. The electrical characterization was performed in a probe station *Grail10-205-LV Nagase Techno-Engineering Co., LTD* at room temperature (RT) and in high vacuum 8.6×10^{-3} Pa. Two BeCu electrodes (source (S) and drain (D)) touched directly the surfaces of the samples. The current response was sensed in the drain electrode after applying source-drain bias in the range -5 to +5 V. The electrical resistivities were calculated using the relationship:

$$\rho = R\frac{A}{L} \tag{4.1}$$

where ρ is the resistivity in Ω.cm, A is the cross-section of the film, L is the electrode separation during measurements (1 mm approximately) and R is the resistance obtained from the inverse of the I-V slopes.

4.3 Results and discussion

Figure 4.1 shows the X ray diffraction (XRD) of the samples after annealing at different temperatures up to 1000 °C. Following the deposition, the raw sample shows sharp diffraction peaks at 2 θ around 43.49° and 50° belonging to the Miller indexes of Cu (PDF2 No 2-1225) [111] and [200] respectively. This confirms that during deposition, the Cu atoms reached the substrate with enough thermal energy to form a well-orientated Cu crystalline layer. Following annealing at different temperatures, the formation of Cu_2O (PDF2 No 1-1142) with cubic structure followed by the formation of monoclinic CuO (PDF2 No 2-1040) is detected due to the thermal oxidation. Initially, annealing at 150 °C allows the Cu to improve crystallization in the [111] and [200] directions. However, peaks at 36.4° and 42.4° corresponding to the reflections [111] and [200] of Cu_2O respectively, appear. Therefore, together with the crystallization improvement, annealing at this temperature makes some copper atoms bond to oxygen atoms to form Cu_2O as the first oxide phase. This oxidation could be mediated by the equation (Neumann *et al.*, 1984):

$$2\mathrm{Cu} + \frac{1}{2}\mathrm{O}_2 \rightarrow \mathrm{Cu}_2\mathrm{O} \tag{4.2}$$

At 200 °C, the Cu_2O peaks got better defined and the lack of the Cu reflections reveals that annealing at this temperature is enough for a complete oxidation of the thin copper film. After annealing at 250 °C, the [200] reflection of the Cu_2O is hardly detected which means that most of the Cu_2O phase is crystallized in the [111] direction. Furthermore, the reflections [-111] and [111] belonging to CuO appear, revealing initial transformation of Cu_2O into CuO. This phase transition might be mediated by the following equation (Akkari *et al.*, 2007):

$$\mathrm{Cu}_2\mathrm{O} + \frac{1}{2}\mathrm{O}_2 \rightarrow 2\mathrm{CuO} \tag{4.3}$$

The transition from Cu_2O to CuO is better observed after annealing the samples at 275 °C, in which the XRD reveals sharp Miller indexes [-111] and [111] belonging to the CuO coexisting with Cu_2O. Also, at this annealing temperature, the Cu_2O phase is highly crystallized in the [111] direction and it may have effects in the electrical characterization as will be discussed below. At 300 °C, most of the surface is covered by CuO and a very small amount of Cu_2O is detected. The transitions from Cu to Cu_2O and from Cu_2O to CuO in this work are in good agreement with the oxidation behavior of thin Cu films on glass substrates reported by other authors (Figueiredo *et al.*, 2008; Gao *et al.*, 2001; Koffyberg & Benko, 1982). Following further annealing above 300 °C, the CuO stabilizes and formation of other additional type of oxide is not detected (data not shown here).

However, the mean grain size of this oxide increases with annealing temperature as we discuss next. At high temperatures such as 900 and 1000 °C, reflections belonging to the silicon-based substrate appear, predicting uncovered areas of the substrate as shown in the SEM images in Figure 4.2.

In general, from the XRD, the sequence of the oxide phase formation on the thin copper films by thermal oxidation is Cu → Cu + Cu_2O → Cu_2O → Cu_2O + CuO → CuO. Note that the formation of pure Cu_2O occurs at smaller interval of annealing temperature (around 200 °C) than that required to obtain pure thin CuO films (300 - 1000 °C). Moreover, no copper silicides were detected by the XRD even at the highest temperatures, which means that the SiO_2 interface is thick enough to prevent diffusion of copper into the silicon substrate. The annealing temperatures for the formation of each phase are clearly distinguished in the XRD (Figure 4.1) and listed in Table 4.1. The table also lists the mean crystallite sizes obtained from the FWHM of the principal reflections by using Scherrer's formula (see Equation 3.1 on page 38) and other characteristics provided by the XRD. From the table, the mean crystallite size of the pristine Cu sample is around 19 nm, and it slightly increases after annealing at 150 °C. Cu_2O also appears after annealing at this temperature with crystallite average size (c.a.) 6 nm. However, this size increases up to 15 nm at 275 °C. At 250 °C, CuO starts to nucleate with crystallite diameters of (c.a.) 9 nm, and it grows with annealing temperature up to 40 nm at 1000 °C. The growth of CuO crystallites at higher annealing temperatures such as 800 - 1000 °C causes porosity and cracks on the thin film surface as discussed with the SEM micrographs next.

SEM micrographs of the thin copper oxides films obtained by thermal oxidation after annealing the thin copper films at different temperatures are shown in Figure 4.2. As mentioned in the experimental section, some parts of the surfaces were carefully scratched with a needle in order to reveal the SiO_2 substrate and to compare it to the thin copper oxide films. After annealing at 200 °C a grained surface seems to cover the substrate. After annealing at 250 °C, the grains agglomerate to form a dense and rough surface perhaps caused by the transition from Cu_2O to CuO. At 300 °C most of the component is CuO with a small amount of Cu_2O. It also contains small agglomerations making the surface rougher. The sample annealed at 350 °C shows fine grains as the main component

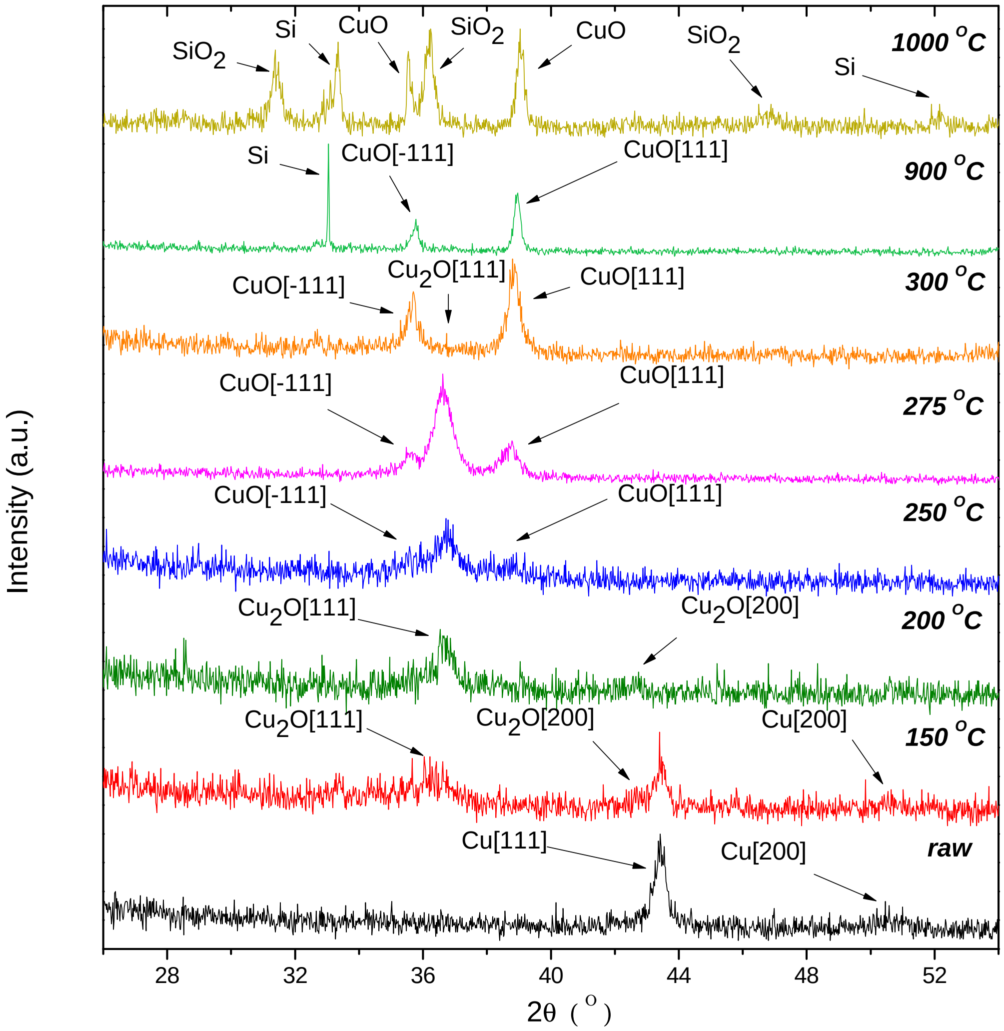

Figure 4.1: XRD patterns of thin copper films after annealing at different temperatures up to 1000 °C

Table 4.1: Summary for the XRD data of thin copper oxide films obtained by thermal oxidation.

Temperature (°C)	**Phase**	**[hkl]**	**2θ (°)**	crystallite size (nm)
RT	Cu	[111]	43.43	19
	Cu	[200]	50.60	
150	Cu	[111]	43.43	21
	Cu	[200]	50.60	
	Cu_2O	[111]	36.35	6
	Cu_2O	[200]	42.70	
200	Cu_2O	[111]	36.35	13
	Cu_2O	[200]	42.70	
250	Cu_2O	[111]	36.74	14
	CuO	[111]	38.63	9
	CuO	[-111]	35.50	
275	Cu_2O	[111]	36.63	15
	CuO	[111]	38.74	17
	CuO	[-111]	35.50	
300	CuO	[111]	38.86	21
	CuO	[-111]	35.70	
900	CuO	[111]	38.95	35
	CuO	[-111]	35.70	
1000	CuO	[111]	38.05	40
	CuO	[-111]	35.56	

of the thin film. At 400 °C, the surface becomes rougher than in the previous cases and the grained nature of the CuO surface is better appreciated. Further annealing at 550 °C and 800 °C makes the grains grow, confirming the results obtained from the XRD. It was reported by Jeong and Aydil that the improvement in grain size and crystallization increase the stress in thin copper oxides films (Jeong & Aydil, 2010). This effect has been deduced from this work by the presence of low porosity and cracks formed after annealing at 800 °C. After annealing at 900 °C, the granular morphology is clearly distinguished. They have edged borders and cover the whole surface, the degree and size of the porosity also increases. Porosity and void formation were also observed by other authors at around this annealing temperature (Musa *et al.*, 1998). Eventually, at 1000 °C, multiple fractures cover most of the CuO surface. These fractures originate due to the growth of the grains and may be orientated parallel or perpendicular to the <111> directions and follow crystal dislocations. It is expected that the porosity and fractures affect the electrical measurements of the thin film as we discuss next.

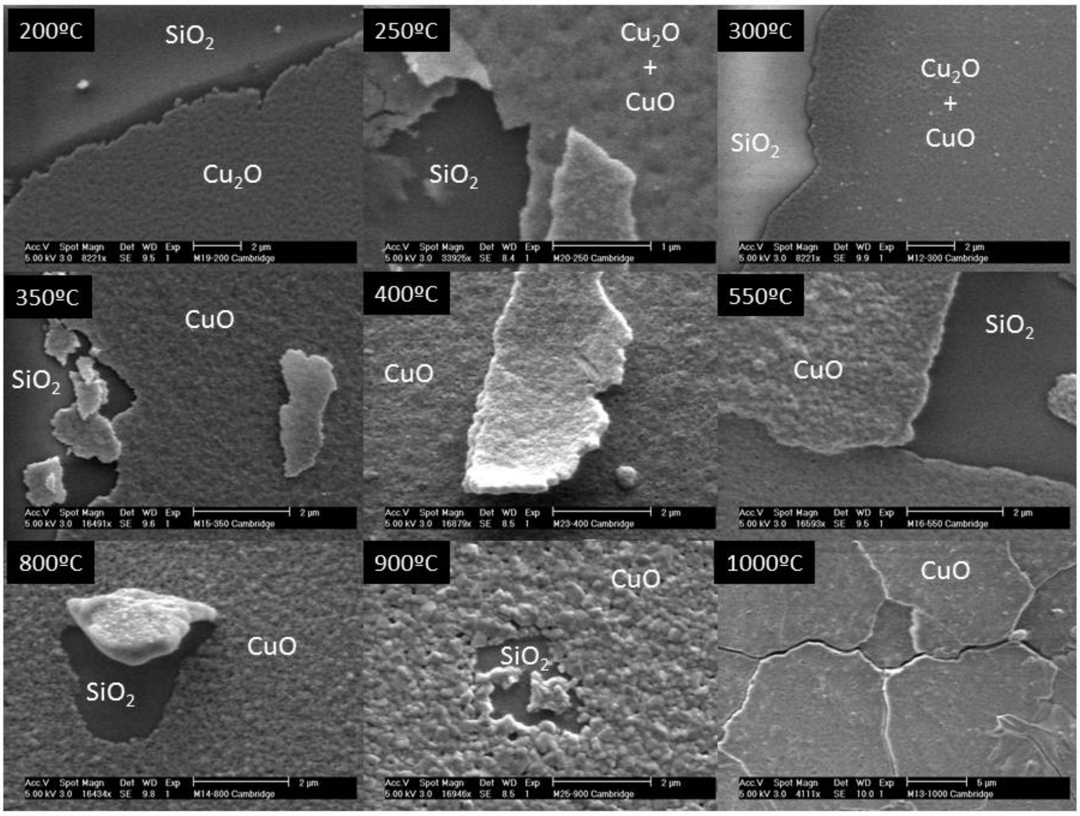

Figure 4.2: SEM micrographs of the oxide formed on thin copper films on SiO_2/Si substrates after annealing at different temperatures. The scratched areas reveal a regular, compact and soft substrate surface.

The electrical characterization is presented in Figure 4.3. In Figure 4.3(a), the I-V measurements are shown, the inset figure is a representation of the measurement configuration with the source and drain electrodes connecting to the sample. The current on the drain (I_D) electrode was recorded as a function of the applied drain-source voltages V_{DS}. As shown in the figure, ohmic responses, which in all cases pass through the zero coordinate point, are observed in the I_D for all annealing temperatures. This behavior implies constant resistances in all the thin copper oxide films fabricated in this work. For clarity only the I-V characteristics of some annealing temperatures are depicted. The highest slope corresponds to the sample annealed at 150 °C, which indicates the lowest resistance of the annealed samples. At higher annealing temperatures, the slopes decrease dramatically indicating higher resistances.

Table 4.2 summarizes the analytical results of the electrical properties of the formed oxides obtained by thermal oxidation. As discussed above, annealing increases oxidation and thus, large decays in the conductivity were expected. However, in the temperature range 250 - 275 °C and 300 - 900 °C anomalous decreases of the resistivity are detected. This effect is better appreciated in Figure 4.3(b), in which the variation of the resistivity as a function of the annealing temperature is depicted to obtain a resistivity phase diagram. This diagram is very similar to those obtained by oxidation of thin copper films on glass substrates reported by other authors (Drobny & Pulfrey, 1979; Figueiredo *et al.*, 2008). The colored areas indicate the dominant phases for each interval of temperature. The main regions are $Cu + Cu_2O$, Cu_2O, $Cu_2O + CuO$ and CuO. It is not possible to determine the exact transition temperature because the oxidation occurs progressively. Therefore, the changes in color contrasts are rough estimations for each transition. Initially, after evaporation, the surface consists of a strained copper layer with resistivity around 6×10^{-5} Ω cm. Note that oxide growth starts on the copper surface immediately after evaporation and exposure of the sample to air. The fair-mustard-colored area indicates the Cu_2O which is the first type of oxide produced by thermal oxidation. The resistivity increases exponentially up to (c.a.) 1.4×10^4 Ω cm when annealing at 200 °C. The rate of increase of the resistivity slows above this temperature up to 250 °C. This is because the amount of pure copper decreases considerably with thermal oxidation, and at 250 °C probably there is no more metal copper to oxidize.

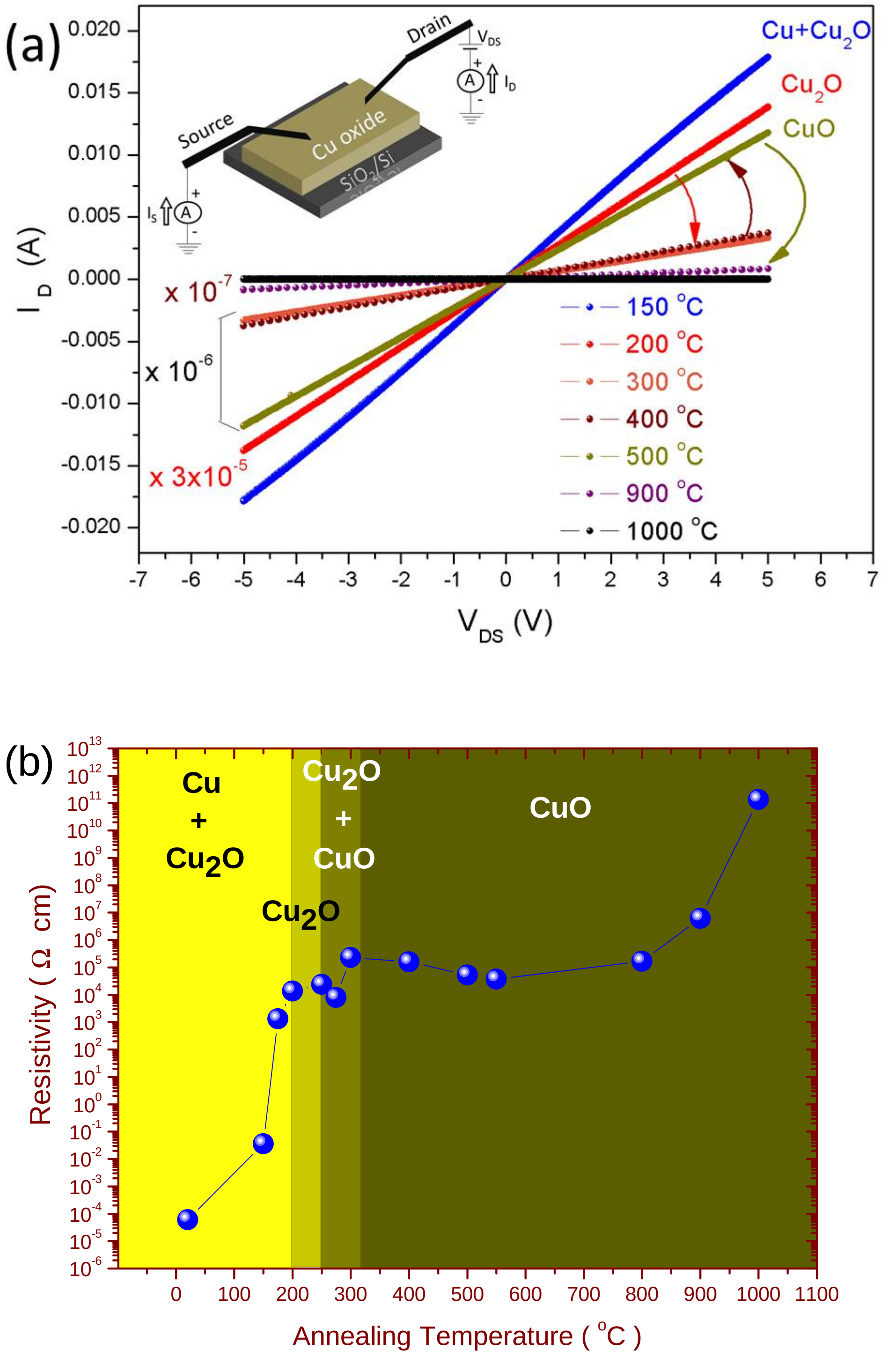

Figure 4.3: a) I-V characteristics of the thin copper-oxide films obtained at different annealing temperatures; b) resistivity phase diagram of the thermally oxidized thin copper films.

Table 4.2: Electrical characteristics of the Cu_2O and CuO obtained by thermal oxidation of thin copper films. R = resistance, ρ = resistivity, σ = conductivity

Temperature (°C)	**Phase**	**R (Ω)**	**ρ (Ω cm)**	σ (S cm^{-1})
RT	Cu	0.6	6.0×10^{-5}	1.7×10^{-4}
150	Cu + Cu_2O	3.6×10^{2}	3.6×10^{-2}	2.8×10^{1}
175	Cu_2O	1.3×10^{7}	1.3×10^{3}	7.6×10^{-4}
200	Cu_2O	1.4×10^{8}	1.4×10^{4}	7.3×10^{-5}
250	Cu_2O + CuO	2.4×10^{8}	2.4×10^{4}	4.2×10^{-5}
275	Cu_2O + CuO	8.0×10^{7}	8.0×10^{3}	1.3×10^{-4}
300	CuO	2.3×10^{9}	2.3×10^{5}	4.4×10^{-6}
400	CuO	1.6×10^{9}	1.6×10^{5}	6.4×10^{-6}
500	CuO	5.2×10^{8}	5.2×10^{4}	1.9×10^{-5}
550	CuO	3.7×10^{8}	3.7×10^{4}	2.7×10^{-5}
800	CuO	1.7×10^{9}	1.7×10^{5}	5.9×10^{-6}
900	CuO	6.1×10^{10}	6.1×10^{6}	1.6×10^{-7}
1000	CuO	1.3×10^{15}	1.3×10^{11}	7.4×10^{-12}

From 250 °C up to approximately 325 °C (mustard-colored area), Cu_2O and CuO coexist. Interestingly, at 275 °C, a decrease in the resistivity is detected. This behavior in the resistivity of Cu_2O has been observed for many years and it is not completely understood. It was initially believed that this effect was exclusively dependent on the excess of oxygen content in the copper oxide (Zhuze & Kurchatov, 1932). However, this assumption was discarded because Cu_2O was found to be a p-type semiconductor and thus the conduction should originate due to the presence of holes in the valence band and it could be improved by doping (Olsen *et al.*, 1982-1983). In this sense, it has been confirmed that in this material the carriers are generated by Cu-vacancies in the crystalline structure (Asbrink & Norrby, 1970; Kikuchi & Tonooka, 2005). Drobny and Pulfrey (Drobny & Pulfrey, 1979) suggest that during the transition from Cu_2O to CuO, the CuO sites probably act as electrically neutral defects and replace the electrically active copper vacancies resulting in the decrease of the resistivity. Whatever the case is, in addition to those proposed mechanisms, assuming that the conductivity in this material is dominated by intra-grain mobility, then it is expected to be enhanced by improvement of crystallization together with the increase of grain size, resulting in a decrease of the resistivity. This was confirmed above: at 275 °C Cu_2O reaches higher crystallization and bigger grain size, and a decrease of the resistivity was observed at this temperature. Nevertheless, further annealing also accelerates the transition of Cu_2O to CuO which eventually results in an excess of the latter and a continued increase of resistivity.

Above the annealing temperature of 300 °C, CuO stabilizes and the resistivity decreases again, especially at the initial stages of the CuO area. This decrease in the resistivity of pure CuO has attracted intense interest of many researchers, especially in the field of superconductivity. To compare, each Cu atom in the CuO monoclinic structure is planar-coordinated by four O atoms and one additional apical O atom forming a distorted tetrahedron (Asbrink & Norrby, 1970). This arrangement of atoms in the crystalline structure resembles those of high-T_C copper oxide superconductors, usually composed by multiple perovskite blocks - such as $YBa-2Cu_3O_7$, in which the planar-coordinated Cu by the four O atoms is believed to be the layer in which super-currents flow. Similar to the case of the Cu_2O, in the present work, we observed that annealing produces better crystallization and bigger sizes of the CuO crystallites leading in a decrease of the resistivity. Therefore, it is reasonable to believe that improvement of the crystallization and bigger crystallite sizes improve conductivity in both types of oxides. Eventually, the increase of the resistivity observed at temperatures higher than 800 °C may be caused by the crystal defects, porosity and dislocations detected above.

Due to the fact that pure Cu_2O and thin CuO films have been found to be formed at 200 °C and above 300 °C respectively by following the thermal oxidation technique described here, hetero structures of thin copper oxide films, such as that shown in Figure 4.4, can be easily fabricated and tested for potential electrical applications. For instance, recently copper oxide hetero junctions have been reported to be good candidates for solar-cell applications (Mimani *et al.*, 2004; Mittiga *et al.*, 2006; Peng *et al.*, 2010). Copper oxide hetero structures Cu_2O/CuO on SiO_2/Si or on other types of substrates could be inexpensively fabricated as follows. A deposited thin copper film on SiO_2/Si can be transformed into CuO/SiO2/Si by annealing above 300 °C. In a subsequent step, copper could be deposited on this system and annealed at 200 °C to form the next Cu_2O layer. Alternatively, a Schottky barrier can be formed on the latest by direct deposition (e.g. by evaporation) of copper or other metal on top. Thus the top layer can be used as an electrode for electrical connections. Eventually, since both Cu_2O and CuO are p-type semiconductors, by n-doping either of them, p-n copper oxide hetero junctions similar to those reported by other authors can be more easily fabricated and tested for solar cell applications (Han & Tao, 2009b). Moreover, investigations of these materials which present various electrical behaviours are promising for a better understanding of the conductivity mechanism in semiconductor hetero-junctions.

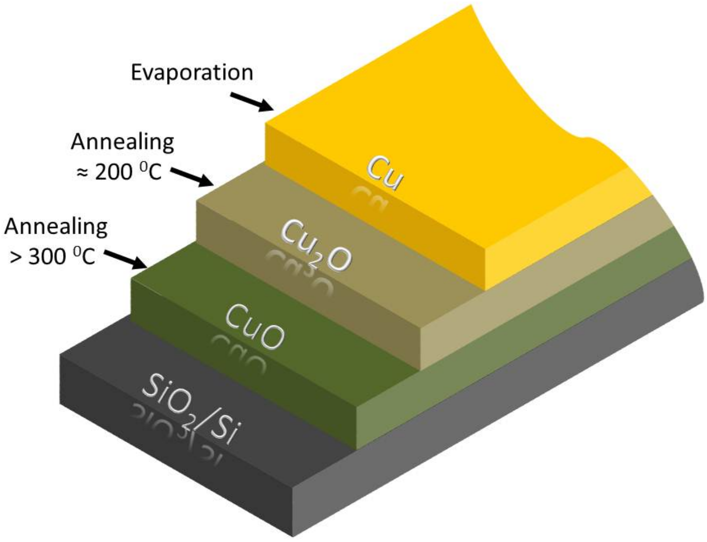

Figure 4.4: Design of a copper oxide hetero structure which can be fabricated by following the thermal oxidation described in this work.

4.4 Conclusions

Thin films of Cu_2O (cubic structure) and CuO (monoclinic structure) were obtained by thermal oxidation following annealing Cu thin films at different temperatures. At low annealing temperatures some copper atoms bond oxygen atoms to form Cu_2O as the first oxide phase. It is not possible to determine the exact temperature transition because oxidation occurs progressively. However, the phase transition upon increasing the annealing temperature is Cu $\rightarrow$ Cu + Cu_2O $\rightarrow$ Cu_2O $\rightarrow$ Cu_2O + CuO $\rightarrow$ CuO. Following the technique presented here, pure thin Cu_2O films are obtained at 200 °C, whereas, thin CuO films are obtained above the annealing temperature 300 °C. Annealing also improves crystallization and increases the crystallite sizes of both copper oxides. The resistivity phase diagram obtained by I-V characterization, presents anomalous decrease of the resistivity at the annealing temperature ranges 250 - 275 °C and 300 - 600 °C. Together with hole doping “effect”, this behavior in the resistivity may be related to the good crystallization and bigger crystallite sizes produced by annealing. Although oxide formation still limits the use of copper in nanoelectronics, the thermal oxidation technique described here can be used to fabricate copper oxide hetero structures which are very useful for their potential applications in large-area electrical devices.

Chapter 5

Thin nickel films: Nanogap electrode fabrication

In this chapter the fabrication of nickel nano-spaced electrodes for electronic nanodevices by electroplating is discussed. The necessary reagents, conditions and processes required to obtain nano and atomic gaps between soft and clean electrodes are described. In the electroplating method, the sample is immersed in a solution which contains the metal ions to be deposited, these metal ions of the electrolyte move towards the sample under an applied voltage. The technique is described by electrodepositing nickel ions from an electrolyte on to nickel electrodes in a conventional electrochemical cell. Current-voltage characteristics are also presented to evaluate possible applications of the nanogap electrodes in electronic nanodevices.

5.1 Introduction

Nano and molecular electronics devices require the fabrication of symmetrical metal electrodes separated by a nanogap ("nanogap electrodes") in which a specific molecule or crystal can be placed in order to connect them to the macroscopic world. In the last two decades, vertical structures in which a self-assembled monolayer (SAM) of molecules is electrically connected on one side with a scanning tunneling microscope (STM) (Datta *et al.*, 1997; Emberly & Kirczenow, 2003) or conductive probe atomic force microscope (C-AFM) (Wold & Frisbie,

2001) and on the other side by a metallic surface have been demonstrated. Even though this approach has yielded many important results, it suffers from limitations such as the enormous asymmetry of the electrodes, the requirement of a high vacuum environment, difficulties in mass production and difficulty to maintain a stable chemical bond between the molecule and the microscope tip due to mechanical vibration. To solve these problems, more recently, new coplanar metal/molecule/metal devices have been proposed. Nanogap electrodes are fabricated before the molecular components, and they are subsequently inserted. This methodology has the advantage that the junction can be characterized with and without the presence of the molecule thus allowing the characterization of the molecule. Among others, three are the most remarkable new approaches for making in plane nanogaps: (i) controlling a break junction mechanically, (ii) electrical breakdown of thin metal wire via electromigration and (iii) electroless and electrochemical plating. These techniques are schematically represented in Figure 5.1. The first technique was first developed by Moreland & Ekin (1985). A Nb-Sn wire mounted on a flexible glass beam can be broken to form an electron tunneling junction between the fracture elements. The method was later improved by other researchers. Notched wires of different metals are obtained first with lithography, by bending the substrate with a piezoelectric transducer connected to a pushing rod and the gap is then formed after breaking the neck (Figure 5.1(a)) (Kergueris *et al.*, 1999; Krans *et al.*, 1995; Muller *et al.*, 1996; Parks *et al.*, 2007; Reed *et al.*, 1997; Ruitenbeek *et al.*, 1996; Smit *et al.*, 2002; Zhou *et al.*, 1995). Using this method, the gap between the electrodes can be flexibly and precisely adjusted to fit different molecules, but it cannot be removed from the apparatus and thus is unsuitable for solid-state device applications. In contrast, in the electromigration-induced break junction technique (EIBJ technique - Figure 5.1(b)), the nanogap is produced by applying large current densities to the wire. At high current densities, momentum transfer from the electrons to the ions in the lattice causes some ions to drift gradually in the direction of the electron flow (Bolotin *et al.*, 2004; Durkan, 2007; Khondaker, 2002, 2004; Liang *et al.*, 2002; Mahadevan & Bradley, 1999, 2000; Park *et al.*, 1999; Taychatanapat *et al.*, 2007). This mass flux can lead to the growth of voids in the wire, finally causing the formation of the gap (Mahadevan & Bradley, 1999). This process is useful to obtain nanogaps up to 1 nm with high efficiency (Park *et al.*, 1999) and it can be controlled by observing the current-voltage characteristics until a tunneling signal is sensed (Park *et al.*, 1999, 2002). However, to date, massive fabrication of multiple nanogaps in an array of electrodes is still difficult to achieve by this technique. In the electrochemical technique, common lithographically-obtained electrodes are grown to reduce their initial separation. The process takes place by submerging the electrodes in an electrolyte usually containing different types of metal ions (Figure 5.1(c)). The metal ions can be selectively deposited onto the electrode surfaces assisted by reductive agents. The gap distance depends on the reaction time, reactant concentration and applied voltage between the electrodes (Céspedes *et al.*, 2002; Deshmukh *et al.*, 2003; Kashimura *et al.*, 2003; Kervennic *et al.*, 2002, 2003; Li *et al.*, 2000; Morpugo *et al.*, 1999; Sahoo *et al.*, 2006; Sokolov *et al.*, 2007; Yang *et al.*, 2002). Furthermore, by using a feedback system, the process can be reversed in the dissolution mode for controlled etching of atoms from the electrode surfaces to the solution and thus the gap dimension can be monitored. To date, the electrochemical plating technique is one of the most used technique for the fabrication of metal electrodes separated by a nanogap. Next, we discuss more about the electrodeposition technique.

Table 5.1 summarizes some of the most noticeable results and conditions for the fabrication of metal nanogaps using the electrochemical technique. When surveying the literature, we found that, with some exceptions, e-beam lithography (EBL) or focused ion-beam milling (FIB) techniques are mostly used to obtain the initial electrode separation in the range 40-400 nm. Most authors use lock-in amplifiers to control the deposition and to study the quantum conductance in situ. Little consideration has been given to the tunneling current enhancement caused by the electrochemical potential relative to the reference electrode (Shu *et al.*, 2000) or by the presence of the ions in the electrolyte (Garcia *et al.*, 2003; Hua & Chopra, 2003; Kervennic *et al.*, 2002; Morpugo *et al.*, 1999). Moreover, although most of the experiments listed in the table provide general views about the electrodeposition process, they do not provide enough information about the reactions that take place or details on the electrolyte characterization, which are also necessary in order to prevent the formation of passivation or oxidation layers on the surface. It is also seen from the table that gold electrodes are preferred by

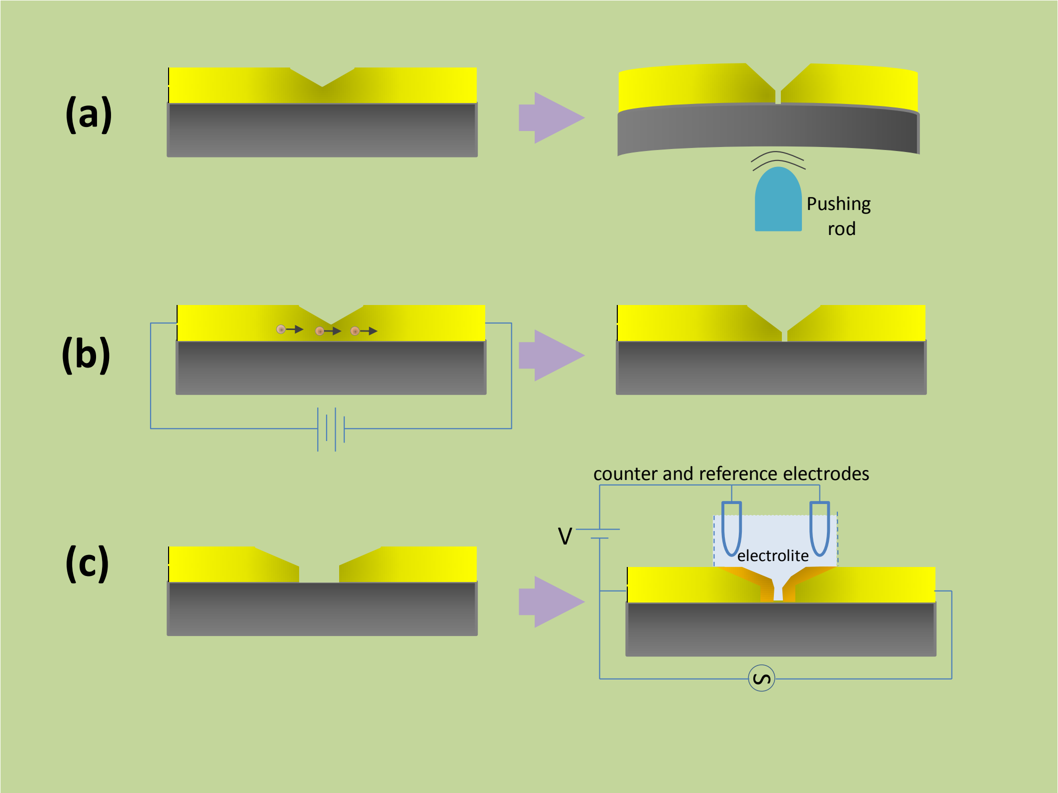

Figure 5.1: In-plane techniques for the fabrication of nanogaps: in the break-junction technique (a) the gap is formed after bending the flexible substrate; in the EIBJ technique (b) high density currents allow the electromigration of atoms to form the gap; and in the electroless and electrochemical technique (c) electrodes forming an initial wide gap are plated to reduce the gap separation

most authors; in fact, as mentioned above, gold is a good conductor and prevents oxidation. However, magnetic deposition on magnetic metal electrodes can be more attractive since they allow the study of single charge and spin transfer. For instance, ferromagnetic electrodes forming a point contact could be very helpful for studying the controversial ballistic magnetoresistance (BMR) effect (Egelhoff *et al.*, 2004; Elhoussine *et al.*, 2002; Gabureac *et al.*, 2004; Mallett *et al.*, 2004; Ozatay *et al.*, 2004; Svedberg *et al.*, 2004; Yang *et al.*, 2002). In the next section we describe the fabrication of nickel nanogaps by the electrodeposition technique.

5.2 Experimental

In this section, we describe the fabrication of nickel nanogap electrodes using a standard electrochemical cell. We characterize the electrolyte, describe the electrochemical conditions and study the time evolution of the electrode growth up to the point of contact. During the plating process the separation width between the electrodes decreases exponentially with time and the nanogap is achieved by stopping the electroplating just before the electrodes touch. In addition, we demonstrate that even if the electrodes are completely bridged during the electroplating technique, the EIBJ technique mentioned above can be successfully applied to re-open the nanogaps.

5.2.1 Fabrication of the initial electrodes

The initial working electrodes were fabricated by lithography technique and lift-off process, the process is explained in detail in Section 2.3 in page 21. In brief; first, Small Ni pellets (99.999% purity) were evaporated from a ceramic boat on the tips of gold wires previously deposited on polished SiO_2 (2 μm)/Si(100) substrates using an Edwards 306 evaporator system with a base pressure of 10^{-7} mbar. The samples were cleaned with acetone, isopropyl alcohol and ultrasound following a standard procedure before deposition. The rate of evaporation was maintained at 0.1 nm s^{-1} and the thickness of nickel (70 nm) was controlled by a quartz crystal microbalance located next to the sample. Two configurations were designed; one containing four non-uniform electrode arrows in which the initial

Table 5.1: Electroplating conditions and results for the fabrication of nanogaps and nanocontacts reported in the literature. In all cases, lock-in amplifiers were used to measure the quantum conductance in-situ. EBL: Electron (e)-beam lithography, FIB: Focus Ion Beam milling, NM: No measurement has been performed.

Electrode metal	Deposition metal	Initial method	Electrolyte	Initial gap width	Final gap width	*Exsitu* data	Reference
Gold	Gold	EBL	0.01 M $KAu(CN)_2$	50-400 nm	5 nm	NM	Morpugo *et al.*
Gold	Gold	EBL	0.1 mM KAu	100 nm	<1 nm	$I-V$	Kervennic *et al.*
Gold	Gold	EBL	0.01 M $KAu(CN)_2$	50-200 nm	10 nm	NM	Kashimura *et al.*
Gold	Copper	EBL	0.02 M $CuSO_4$	250 nm	2 nm	$I-V$	Deshmukh *et al.*
Gold	Nickel	FIB	1.5 M $Ni(SO_3NH_2)_2$	100 nm	Contact	NM	Sahoo *et al.*
Gold	Nickel	EBL	0.01-0.02 M $NiSO_4$	100 nm	Contact	$I-V$	Kashimura *et al.*
Gold	Nickel	Porous	0.50 M $NiSO_4$	60-120 nm	Contact	NM	Elhoussine *et al.*
Gold	Cobalt	FIB	$CoSO_4$	100 nm	Contact	NM	Sokolov *et al.*
Gold	Cobalt	FIB	0.22 M $CoSO_4$	250 nm	2 nm	$I-V$	Deshmukh *et al.*
Platinum	Gold	EBL	0.01 M $KAu(CN)_2$	50-200 nm	8 nm	NM	Kashimura *et al.*
Platinum	Platinum	EBL	0.10 M K_2PtCl_4	40-80 nm	20-3.5 nm	$I-V$	Kervennic *et al.*
Nickel	Nickel	FIB	H_3NiSO_3	100 nm	Contact	NM	Yang *et al.*

gaps of two of them was 2.5 μm width (see Figure 5.2 (a)); and the other with three uniform electrode arrows with initial gaps of 200 nm (see Figure 5.2 (a)). The samples were coated with a layer of Polymethyl Methacrylate (PMMA) to protect their surfaces and to avoid leakage during measurement. To focus the plating only in the tips of the electrodes during the electrodeposition process, rectangular windows of dimensions 28 μm × 100 μm were opened on the PMMA coating, thus exposing the tips of the four electrodes samples. Similarly, circular windows of 6 μm diameter were opened on the PMMA protecting layer on the samples with three electrodes. Figure 5.2 (c) is a representation (not to scale) for the lateral section in both types of samples. In the figure, the gold layers will help the conection to the electrical devices, the nickel layers are the surfaces to be plated and the opened window in the PMMA will ensure deposition only on the region of interest. The four-arrow samples are used to study the gap width evolution with time of electrodeposition, whereas the three-arrows samples were used to study the effects of electromigration after bridging the electrodes.

5.2.2 Electroplating

The electroplating took place in a conventional electrochemical cell described in §2.3 on page 21. The reference electrode (R.E.) consisted of a commercial SCE saturated Calcomel KCl and the counter electrode (C.E.) was a platinum mesh. A potentiostatic control ensured that the real potential E(t) at the working electrode (W.E.) with respect to the R.E. remained almost the same during the applied voltage generated by the function generator. The control also helped to minimize any additional drop in the potential caused by the internal resistance of the electrolyte. The electrolyte was prepared by dissolving nickel sulfate ($NiSO_4$, Sigma Aldrich 13635) and boric acid (H_3BO_3, Sigma Aldrich B9645) in aqueous solution. H_3BO_3 is commonly used in pure nickel and nickel alloys electroplating because it shows some interesting properties such as excellent buffering to maintain a steady pH in the electrolyte, surface activity, resistance to hydrogen evolution reaction and improved current efficiency (Grand & Talbot, 1993; Horkans, 1979; Karwas & Hepel, 1989; Popov *et al.*, 1993; Tilak *et al.*, 1977; Wu *et al.*, 2003). Since we are plating in the nanoscale, the addition of any other additives is not recommended

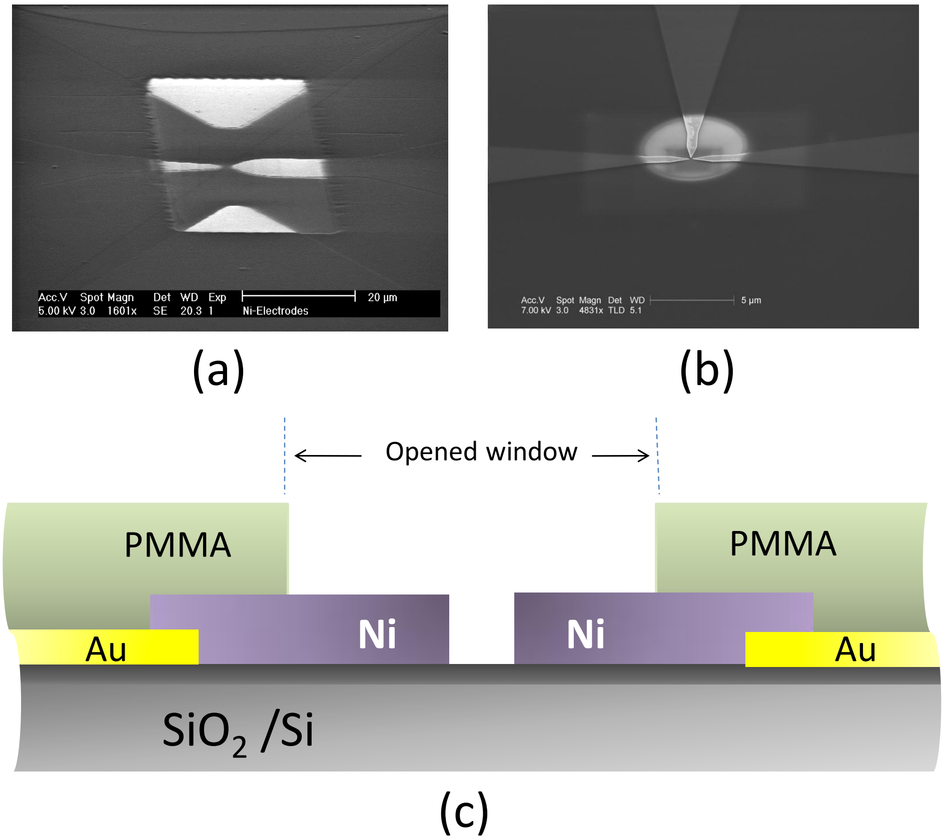

Figure 5.2: Initial nickel electrode configurations protected by a PMMA coat: (a) Four-electrode configuration with a rectangular window opened over the non-uniform arrows, (b) Three-electrode configuration with a circular window opened over the uniform arrows. (c) Representation (not to scale) of the lateral cross-section for both types of samples. The initial samples are obtained by conventional lithography techniques, see §2.1 on page 11 for more detail.

in order to avoid the risk of contamination, passivation-layer formation and a rough surface. After trying with different concentrations of the electrolyte components, we found that the best control of deposition in nano-scale is achieved by combining 50 mM of $NiSO_4$ and 500 mM of H_3BO_3, whereas for micro-sized or larger area characteristics, higher concentration of nickel sulfate is required. The cyclic voltammetry (CV) technique was performed for the electrolyte characterization and it was carried out in the same electrochemical cell. This technique is usually employed to estimate the potential for optimum plating and to study the deposition process and explained in Section 2.3 on page 21. The CV was performed by applying different scan rate potentials, and a nickel surface was chosen during CV in order to study the chemical reactions on this metal. For this purpose, a thin nickel film (100nm thickness) was covered by electroplating tape, except an area of 0.72 cm^2 and placed in the working electrode. The scans were addressed in the cathodic direction (from +0.5 to -0.15 V vs. SCE). All electrochemical experiments were performed at 25 °C, pH 3.67 and using a Potentiast/ Galvanostat (VersaStat TM II - Princenton Applied Research) interfaced with a personal computer (PC) and controlled by the Power Suit program.

5.3 Results and discussion

Figure 5.3(a) shows the cyclic voltammetry curves of the plating bath at different scan rates. As shown in the figure, for most scan rates, when the potential is scanned from +0.5 V to -0.6 V, no significant current flow is observed. According to the CV, the metal deposition starts at around -0.6 V vs. SCE. As the cathodic potential increases from -0.6, the current also increases and reaches a peak at around -1.0 V. This peak corresponds to the reduction of Ni^{2+} to Ni in the working electrode. The exponential trend of I at higher absolute values of V might be associated with capacitive charge currents caused by oxygen evolution in the aqueous solution as proposed by Mimani *et al.*. At a scan rate of 156 mV/s, when the potential is reversed the current follows the same potential dependence up to the irreversibility point of -1.1 V. The irreversibility point increases as the scan rate increases. After the potential reaches back to -0.6 V, negative currents start to flow independently of the scan rate. A new peak continues and its intensity depends on the scan rate potentials. This wide peak corresponds to the oxidation of Ni to Ni^{2+} together with a possible hydrogen evolution reaction in the auxiliary electrode (Mimani *et al.*, 1993). In general, the CV in the figure is quasi-irreversible independently of the scan rate. Different scan rates do not change the shape of the cyclic loop but increase the loop area, the peak current and peak potentials separation, as shown in the inset in the figure. These characteristics in the CV reveal that the Nerst equation is only approximately satisfied (Heinze, 1984). To obtain the diffusion coefficient (D) we use the Randless-Sevcik equation (equation 2.14 in page 26) which gives the value 4×10^{-5} cm^2/s. Based on these results, any applied potential from the region -1.2 V to -1.5 V versus SCE can be selected for a good deposition of Ni. It is obvious that from this interval, the lowest applied potential (-1.2 V) provides the slowest deposition which is preferred for a better control of the micro and nano characteristics. Figure 5.3(b) shows the current and charge transfer variations during electrodeposition at the recommended -1.2 V applied voltage. The current varies exponentially following the Nerst Law (Bard & Faulkner, 2001) and correctly implies that changing the applied potential by several milli-volts modifies drastically the electroplating rate. Typically, an inducing current of 0.2 μA allows an electroplating rate of 1 $Ås^{-1}$ at room temperature (Kashimura *et al.*, 2003). During the experiment, we also observed that a slight increment of the applied potential results in enhanced surface roughness together with a decrease of the density of the deposited metal (data not shown here). From the plot, it is also clear that as time passes, the increase of the surface area allows more charge transfer. The mass transfer obtained by the Faraday law is shown in the inset of the figure, and fitting it with time of the electrodeposition, the following relation is obtained:

$$m = 2.3 \times 10^{-9} t^{3/2} \tag{5.1}$$

where m is the deposition mass during the process and t is the time. In this way, it is possible to control the amount of metal deposition on the electrodes by adjusting the time of electrodeposition.

Figure 5.4 presents micrographs of the growth evolution of the type of electrode configuration with rectangular window described above. As expected, the

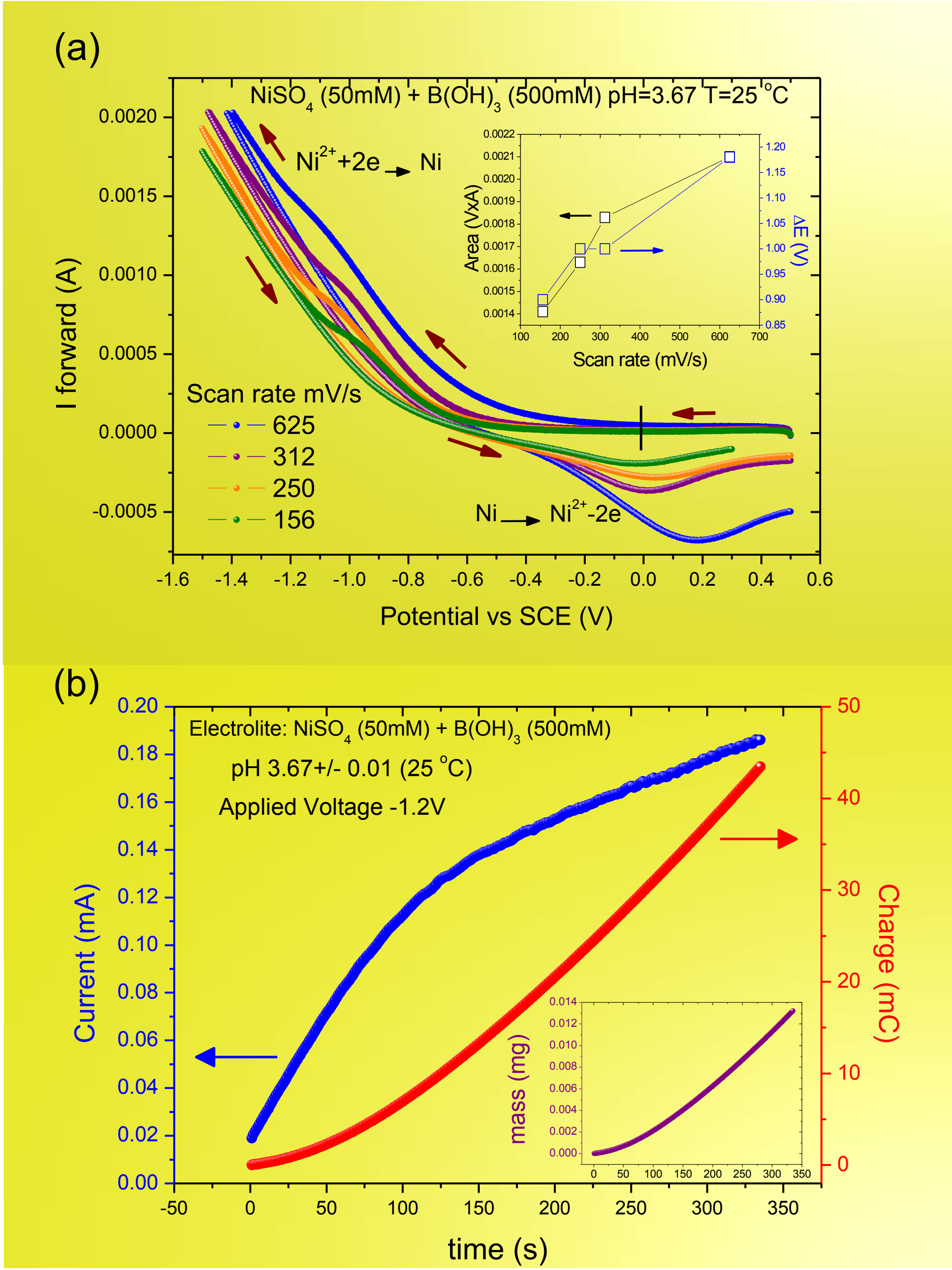

Figure 5.3: (a) Cyclic voltammetry of 50 mM of $NiSO_4$ and 500 mM of H_3BO_3 in aqueous solution at different scan rates. (b) Current and charge variation with time during electrodeposition. Inset (b): deposition mass as function of time.

electrodeposition was focused only on the exposed area of the window. The images reveal typical plated surfaces, in which nickel ions migrate from the electrolyte to the electrodes, making them grow. As described above, in the anode of the cell, the nickel loses two electrons and becomes 2^+, Ni^2+ associate with $(SO_2)^{2-}$ in the solution. In the cathode, the negative charge of the surface attracts the positively charged Ni^{2+} from the solution and repels negative charged ions. The process follows equation 5.1 and stops when the applied voltage is switched off. Therefore, the electrode growth can be controlled with the applied voltage and stopped at different times to achieve a desired width. In the figure, the initial nickel electrodes have a thickness of 50 nm and were separated by about 2.5 μm. Electrodeposition makes the thickness grow up to 50 times and the gap separation decreases with electroplating time until they make contact.

Figure 5.5 shows the nickel electrodes exposed with circular window described above after they were electrodeposited until forming a contact. Note that the vertical electrode which has not been connected to the electrochemical set-up has etched after contact with the electrolyte. Moreover, due to the smaller and more pointed electrode tips than in the previous case, during electroplating, the metal ions of the electrolyte are better guided by the electric field to the sharpest points. Then since the highest gradients of the field are located in the outer corner of each arrow, out of plane growth of the electrodes results. As we will see next, contact electrodes obtained by electrodeposition can be easily reopened by the electromigration-induced breaking junction (EIBJ) technique and then the out-of-plane electrodes would provide some advantages because: (i) there is no residual interlink of metallic adhesion layer over the SiO_2 and preventing the formation of parallel conduction channels on the substrate which can disturb the measurements (Gabrielson, 1993), (ii) there is smaller probability for island formation due to Joule heating (Trouwborts *et al.*, 2006), and (iii) it avoids the use of molecular adhesion layers beneath the metal (Mahapatro *et al.*, 2006). Molecular devices could be obtained by depositing the molecules on the electrodes before breaking and inducing them to migrate into the gap by subsequent heating. In this way undesired contact between molecules and substrate can be avoided.

At an electrodeposition time of 290 s, the formed gap can hardly be seen by the microscope and I-V measurements need to be performed to detect them

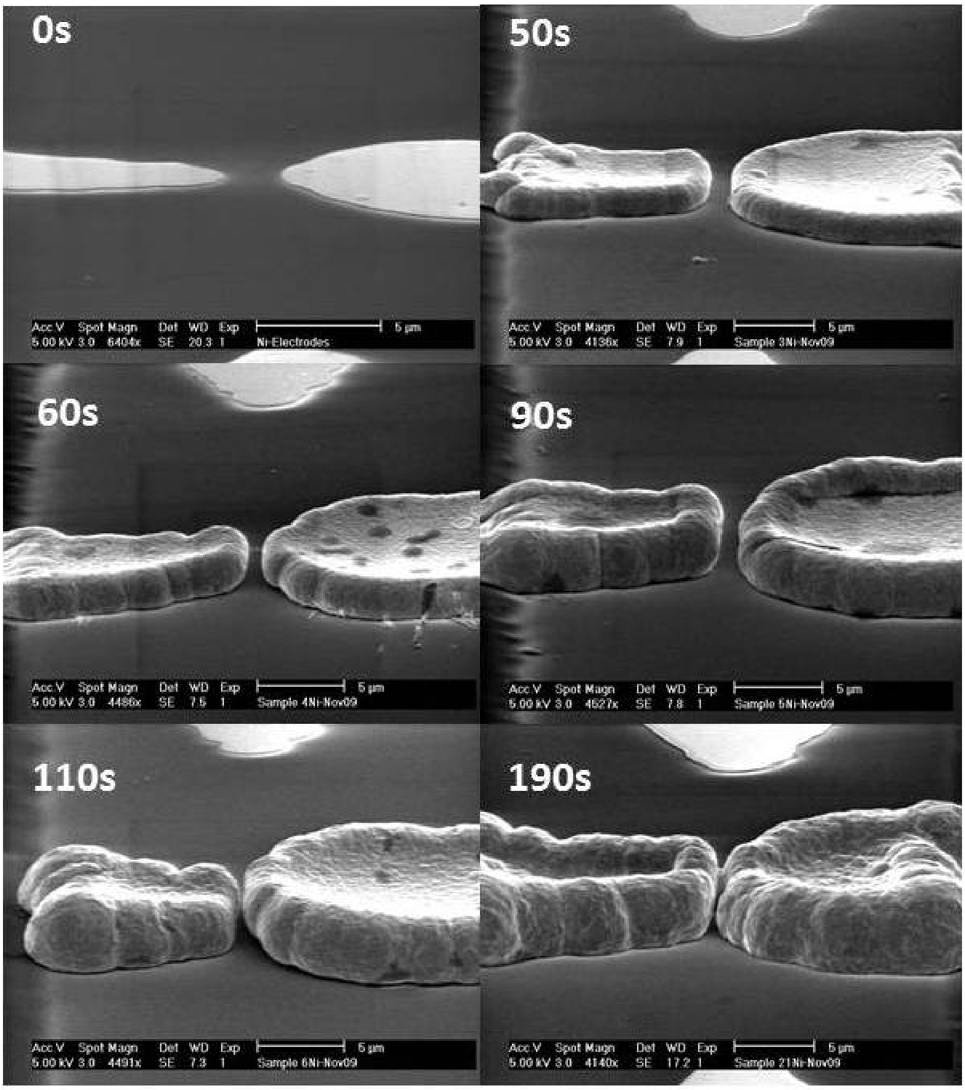

Figure 5.4: Electrode growth during electroplating.

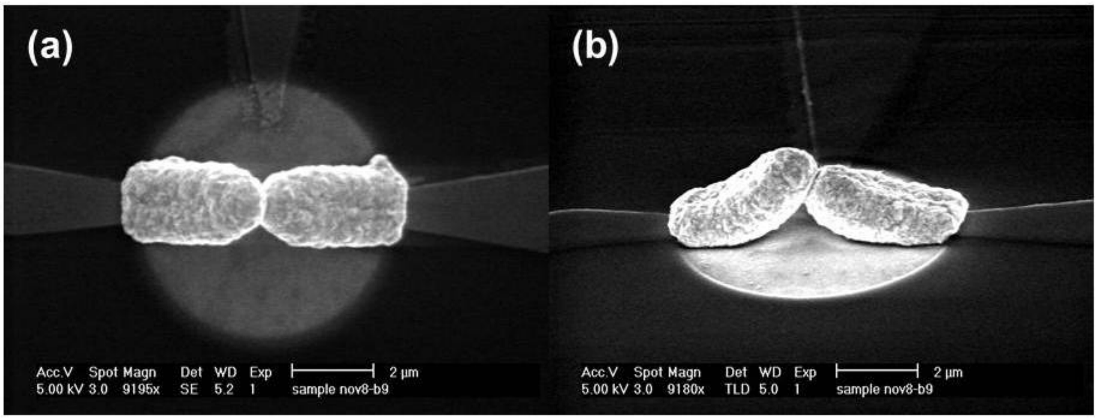

Figure 5.5: Electrochemical plated nickel electrodes after forming contact, (a) top view and (b) lateral view.

as it will be discussed next. The electrodeposition procedure described above means that Equation 5.1 is successfully applicable and allows the control of the gap width between the electrodes by setting the time of electrodeposition alone, but always bearing in mind the other parameters such as electrolyte components, applied voltages, etc. Following this procedure, it is not necessary to average measurements from many samples to find a desired gap width. Figure 5.6 shows the gap width variation with time of electrodeposition. Up to 160 s, the gap width decreases exponentially following the trend:

$$d = 2.44e^{-\frac{t}{100}} \tag{5.2}$$

where d is the gap width (in microns) and t is the plating time (in s). This variation behavior is expected considering that the mass transfer during deposition is not linear with time as discussed above. However, we found that at deposition times higher than 190 s a linear relation dominates the last stages before the electrodes get into contact as shown in the figure inset. In the next section the current-voltage characterization is performed.

Figure 5.7 shows the current-voltage response for the Ni samples electrodeposited during 290, 315 and 350 s. We have observed recordable and reproducible I-V characteristics in the milliampere and microampere range in repeated scans,

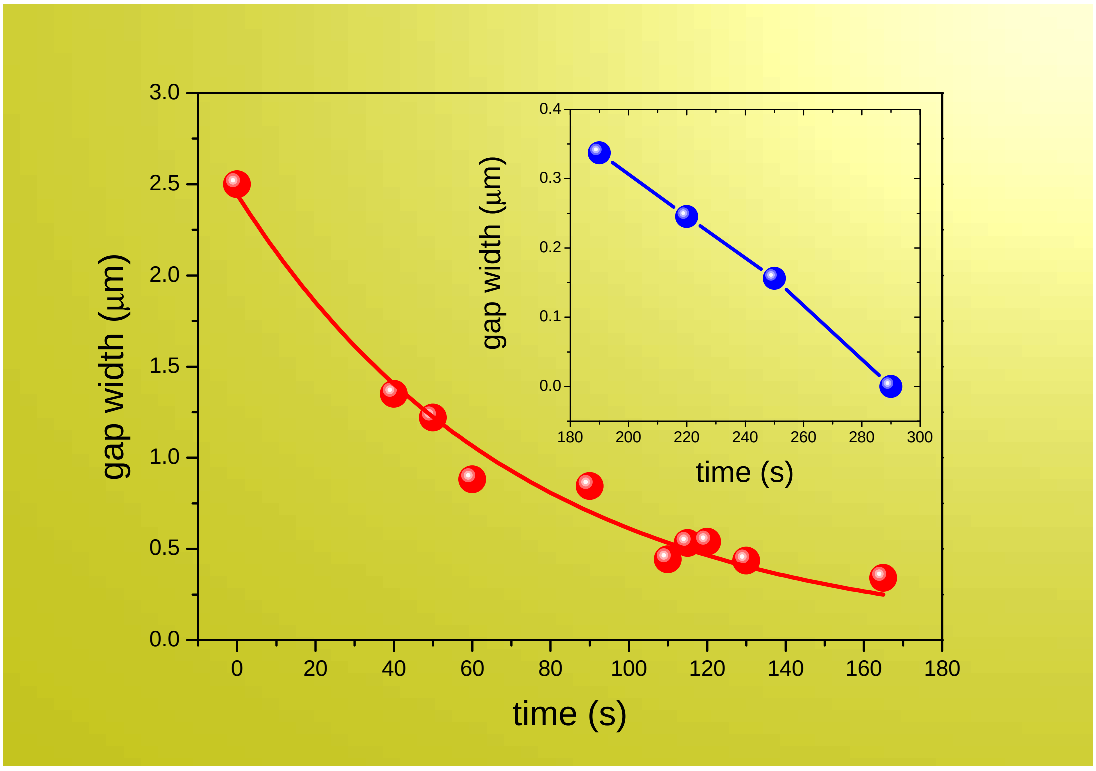

Figure 5.6: Gap width variation (measured by SEM) with electroplating time.

which confirms the stability of the samples. In the figure, three different signals behaviors corresponding to different ranges of electrode separation can be identified. In the first case, the zero dashed line indicates that no current flows which corresponds to a large electrodes separation. The second case related to samples electrodeposited during 290 s and 315 s shows tunneling behavior revealing nanogap formation. In the third case, after 350 s the measurements show ohmic behavior revealing that the electrodes are in contact. In the tunneling signals, after 290 and 315 s of electrodeposition, the samples allow currents of 0.12 μA ($\approx$30 nS conductance) and 8.2 mA ($\approx$2 mS conductance) to tunnel at 4.0 V respectively. Note that the conductance quantum $G_0=2e^2/h$ is $\approx$77.48 μS. In this work the narrower gap widths of the samples were not calculated by using the Simmons' model due to the high asymmetry of the arrow tips of the electrodes. However, it has been reported that a tunneling conductance in the order of the nS is the typical response of gaps with about $\approx$1 nm width (Kergueris *et al.*, 1999; Li *et al.*, 2000; Reichert *et al.*, 2002) which decreases exponentially as the gap width increases (Simmons, 1963). Therefore, the gap width of the sample electrodeposited after 290 s should be around 1 nm whereas the electrodes electrodeposited after 350 s should have atomic separation. These results obviously confirm that at larger deposition times the gap between electrodes decreases and the conductance increases and eventually at 350 s the electrodes make contact. Once the contact is formed, the detected resistance is 157 Ω which implies $\approx$ 80 G_0 conductance; this means that around eighty conducting channels have been formed. The contact allows current densities up to around $4.5 \times 10^-10 \mathrm{A/cm}^2$ and at applied voltages higher than 8.0 V the junction breaks as shown in the stressing curve in figure inset. Once the junction breaks a nanogap is again formed as we discuss next.

Nanogaps can also be reopened after the electrodes contact by inducing the junction to break by means of the electromigration EIBJ technique. For instance, the resistance of the contact shown in Figure 5.7 above was 158 Ω. Applying higher voltages than 1.5 V allows electromigration, the contact breaks at a threshold current (I_{th}) of 11 mA. The nanogap is then reopened due to the physical motion of atoms out of the high-current density areas i.e the contact (Ho & Kwok, 1989; Tu, 2003). Figure 5.8 shows the I-V measurement of the

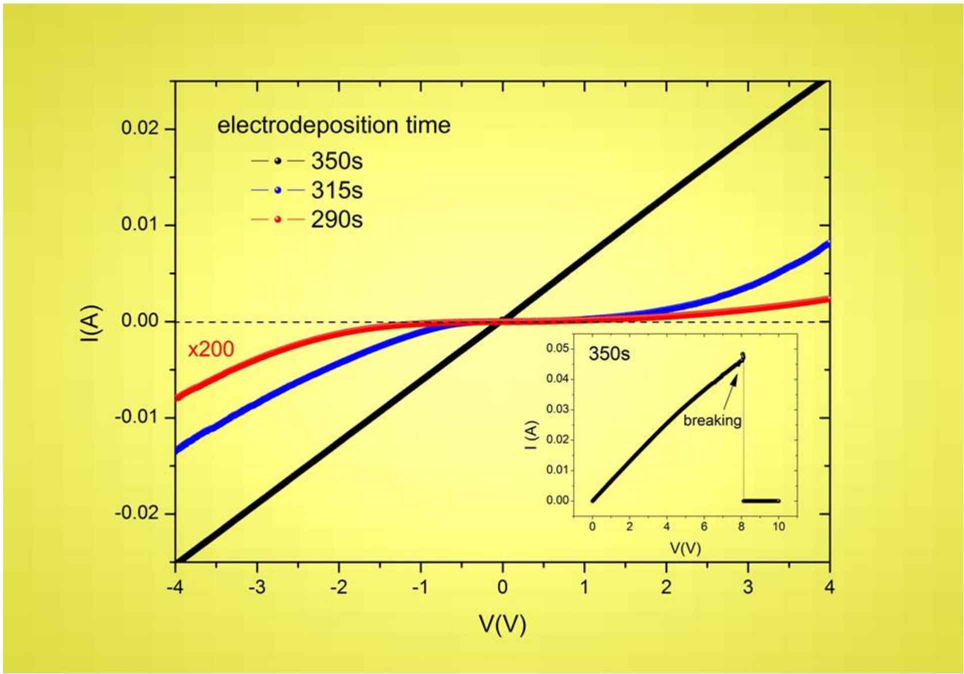

Figure 5.7: Current-voltage responses of the electrodes 290, 315 and 350 s of electrodeposition. The tunneling behavior reveals that nanogaps are formed at 290 s and 315 s, whereas Ohmic behavior indicates that a contact is formed after 350 s of electroplating. Inset: current stressing curve of the sample electrodeposited during 350s.

reopened gap (blue line in the figure) and tunnelling behaviour is detected again. Considering the effective frontal area around A≈7.8x10^{-12} cm^2, the threshold current density (J_{th}=I_{th}/A) for the nanogap formation by electromigration is 1.4 $\times$ 10^{-9}A/cm^2. J_{th} values of about 2.9$\times10^{-8}$ A/cm^2 have been obtained using gold wires (Ho & Kwok, 1989) and this implies that J_{th} values of the order of 10^{-8} - 10^{-9} A/cm^2 are required for the nanogap formation by EIBJ. Moreover, the breaking signal due to the EIBJ technique ensures that the nanogap has reopened and hence the I-V signal shown in the figure results from tunneling through the gap and not through natural oxide layers. To date, there is no exact mechanism for electron transport through nickel nano-electrodes in nanodevices. Nevertheless, it might be interpreted as follows: when no external magnetic field is applied the electrodes have randomly oriented magnetic moments and the gap behaves as a tunnel barrier (as represented inset down in the figure). This disorientation should be responsible for the asymmetric tunneling current when the voltage bias is applied. In contrast, when a magnetic field is applied (e.g. 3.5 kG), the magnetic moments align, the resistance is reduced and this causes the conductance to become symmetrical (red line in the figure). Similar results have been obtained by other authors (Céspedes *et al.*, 2004; Valladares *et al.*, 2010d), and it has also been proposed that under external magnetic fields, the double energy bands of the ferromagnetic electrodes split, increasing the number of sub-bands crossing the Fermi level and thus increasing the conductance in the electrodes (Johnson, 2007; Sokolov *et al.*, 2007).

5.4 Conclusions

We have successfully demonstrated that it is possible to control the production of nickel nanoelectrodes separated by a nanogap by the electroplating technique. The gaps obtained by this technique fall beyond the resolution of e-beam lithography. Careful selection of the electrochemical variables such as the electrolyte concentration, applied potential, cleaning, etc. permit the control of nanogap formation by the time of electrodeposition. Regarding the electrolyte, we showed that that 50mM of $NiSO_4$ combined with 500 mM of H_3BO_3 allow high performance. During the process, the gap width decreases exponentially with time until

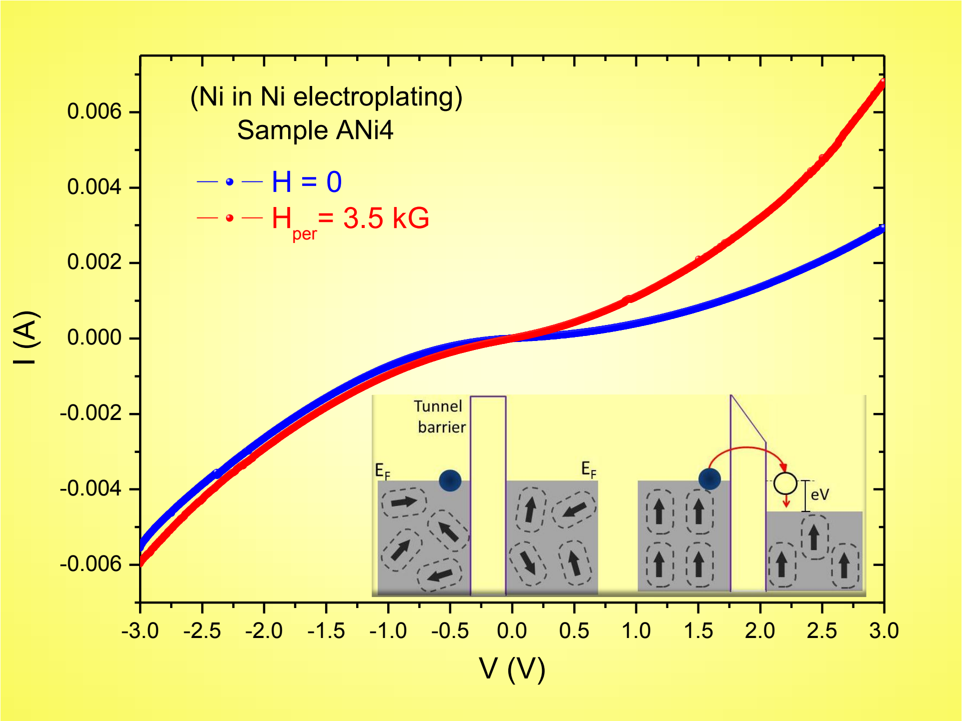

Figure 5.8: I-V tunneling behavior in a reopened nickel nanogap. Inset: Schematic representation of the tunneling effect in the nickel electrodes. Asymmetry is corrected by the application of an external magnetic field suggesting that charge transfer in the nickel electrodes depends on the orientation of the magnetic moments.

the electrodes come into contact. Different nanogap widths can be obtained stopping the process at desired deposition times. The present method offers various benefits such as extremely small gaps, high-yield (≈100%) fabrication and readily available instrumentation. Once the gap is closed, it can be reopened again by the ex-situ EIBJ technique. Applying an external magnetic field corrects the I-V asymmetry; this effect should be related to the orientation of the magnetic moments in the nickel electrodes.

Chapter 6

Oxide superconductor $LaCaBaCu_3O_7$: Attaching grains on gold surfaces

$LaCaBaCu_3O_7$ (La1113) is a high-critical-temperature superconductor (HTS) with $T_{C(onset)} = 80$ K and its structure is similar to the tetragonal YBCO. In this chapter we explore the attachment of La1113 nanograins on Au(111) surfaces through self-assembled monolayers (SAMs) of HS-C_8H_{16}-HS [octane (di)thiol] for their potential application in nanotransistors. We show that La1113 particles (100 nm mean diameter) can be functionalized by octane (di)thiol without affecting their superconducting critical temperature ($T_C = 80$ K). X-ray photoemission spectroscopy (XPS) analysis reveals that the thiol functional heads link the superconducting grain surfaces creating sulfonates and we deduce that bonding between the S atoms and Cu(1) atoms of the La1113 structure would occur. We suggest a design for a superconducting transistor fabricated by immobilized La1113 nanograins in between two gold electrodes which could be controlled by an external magnetic field gate.

6.1 Introduction

Despite current efforts, the replacement of semiconductor technologies by single-molecule electronic devices (SMEDs) is still many years away. Several challenges and problems persist, including, the lack of direct microscopy to confirm the presence of a particular molecule on the junction of the devices, variations in the microscopic configuration from device to device and the necessity of great care and many control experiments. These ensure that silicon devices continue to dominate electronics technologies (Natelson, 2009). Nevertheless, it is widely believed that the present semiconductor-based microelectronics cannot achieve circuit density sufficient to maintain Moore's law (Birnbaum & Williams, 2000; Moore, 1965; Reed & Tour, 2000) and that future electronics will require suitably sized functional elements for the development and design of new architectures and devices. Nanograins could be such elements as they exhibit both small size and size-tunable physical properties which can be customized to meet the requirements of nanoelectronic devices in the near future (Li *et al.*, 2009; Shipway *et al.*, 2000). Within this group, superconducting nanograins are particularly attractive. The benefits of superconducting electronics over semiconductor electronics are the high carriers mobility which allows ultrafast switching speed (for digital applications) and high sensitivity/response to electromagnetic phenomena over a very wide frequency spectrum (for analogue applications) (Booth *et al.*, 1999). Some attempts to fabricate superconducting transistors based on thin-film superconductors attached to metal electrodes have been reported (Mikoushkin *et al.*, 2003; Morán *et al.*, 2003). Nevertheless, the drawbacks of such superconducting-film devices are the intense interdiffusion between layers obtained during growth and the wide area of contact with metal electrodes ($> 1\ \mu m^2$). On the other hand, a recent publication reports superconductivity in a single-C_{60} molecule trapped between two aluminum electrodes (Winkelmann *et al.*, 2009). This promising approach annuls the use of superconductors as thin films. However, it falls in the category of SMEDs working at very low temperatures (< 1 K). To overcome problems such as interdiffusion, size and working temperature, pre-prepared high T_C cuprate superconductor (HTS) nanograins can be utilized by attaching them between metal electrodes. For this purpose it is required that the HTS nanograins are able to attach functional molecules which can then be used to bind the metal electrodes. There are few literature reports about these structures, mainly reports on the attachment of organic molecules (such as alkyl-amines and alkane-thiols) on “large” surface areas (tens of square microns) of ceramic pellets and film substrates of $YBa_2Cu_3O_7$ (YBCO, T_C= 90 K) (Mirkin *et al.*, 1998, 1997). Mirkin *et al.* propose a mechanism for the self-assembly of alkyl-amines on YBCO thin films (Mirkin *et al.*, 1998; Zhu *et al.*, 1998). In that mechanism, alkyl-amine reagents become oxidized to alkyl-imines upon their exposure to HTS's and the superconductor is reduced. The resulting oxygen-deficient region supports the formation of the self-assembled monolayers specifically attacking the Cu^{2+} atoms. However, the lack of reports on nanometer-scale structures raises the question whether nano-sized HTS particles are able to attach functional groups without destroying their superconducting properties as HTS thin films do. In this chapter we report that HTS $LaCaBaCu_3O_7$ (La1113, T_C = 80 K) grains (100 nm mean diameter) can be functionalized with octane (di)thiol molecules and be attached on gold surfaces. From X-ray photoemission spectroscopy (XPS) analysis, we suggest that the binding of the thiol functional heads to the La1113 grains is dominated by sulfonate formation where the S atoms of the thiols bond with the Cu(1) atoms of the La1113. In addition, we found that the superconductivity of the grains survives the functionalization and then we calculate their magnetic phase diagram in order to explore their application in electronical devices. Finally we present a metal-insulator-superconductor transistor design using these thiolated-HTS grains that can be controlled by an external magnetic field gate.

6.1.1 The superconductor $LaCaBaCu_3O_7$

The compound $CaLaBaCu_3O_7$ (La1113) is a superconductor with critical temperature T_{Conset} =80 K. Its crystalline structure is tetragonal, similar to the $YBa_2Cu_3O_7$ (YBCO). The two main characteristics which make La1113 attractive are that its T_C is above the boiling temperature of the liquid nitrogen (T_C = 80 K [10-14]) (Gunasekaran & J.V. Yakhmi, 1993; Gunasekaran *et al.*, 1992; Leeuw *et al.*, 1988; Peng *et al.*, 1989; Yagi *et al.*, 1991) and the low applied magnetic fields that it can support without losing its superconductivity (Valladares *et al.*, 2010b,c). The cell parameters of La1113 are a = b = 3.88 Å and c = 11.60 Å whereas for YBCO superconductor are a = 3.83 Å, b = 3.89 Å and c = 11.70 Å. Figure 6.1 shows schematically a structural comparison of La1113 with YBCO. YBCO has an orthorhombic Pmmm structure and becomes superconductor below $T_{C(onset)}$ of around 90 K (left in the figure), whereas La1113 is superconductor and has tetragonal structure (right in the figure). Moreover, other important differences between both structures are: (i) While the rare earth Y in the YBCO structure is sandwiched between two oxygen-deficient Ba-Cu perovskites, the (1/2, 1/2, 1/2) position in the La1113 structure is shared by La and Ca atoms. (ii) The O(1)(0,1/2,0) of the CuO chains is fully occupied in the superconducting YBCO, whereas O(1) is partially occupied (occupancy ≈ 0.5) in the La1113 structure. The literature reports indicate that La1113 superconductor does not present structural variation after single atom substitution. For instance, its tetragonal structure does not change under different oxygen content (Awana & Narlokar, 2001; Yamaya *et al.*, 1993) or when the Cu(1) site ((0,0,0) site in Figure 6.1) is doped with Zn content (Awana & Narlokar, 2001; Rajvir, 1997). However La1113 structure becomes orthorhombic (Pmmm) when polyhedrons formed by a cation and oxygen atoms such as oxyanions $(BO_3)^{3-}$ or $(PO_4)^{3-}$ are located in the Cu(1) site (Dominguez *et al.*, 2006; Valladares *et al.*, 2004, 2006). Whatever is the case, the T_C of the system depends on the doping concentration. Regarding its magnetic properties, in contrast to the YBCO-7, the La1113 presents interesting properties such as (Valladares *et al.*, 2010b): (i) A magnetic flux can penetrate easily the bulk in its vortex region ($H_{C1} < H < H_{C2}$), (ii) fewer magnetic fields can be trapped in the L1113 than in YBCO and (iii) small currents are able to flow in the bulk. Thus possible applications of La1113 are restricted to applied fields lower than 10 kOe ($\approx$ 1 T) and in the range of 41 K - 76 K. In addition, the “peak effect”is observed during current-density calculation and it is probably caused by secondary phases or from clusters of oxygen vacancies acting as field-induced pins. In this chapter we study these characteristics and calculate the magnetic phase diagram for La1113 showing the irreversibility line in order to find the magnitudes of applied magnetic fields which allow potential application of this superconductor in nanoelectronic devices.

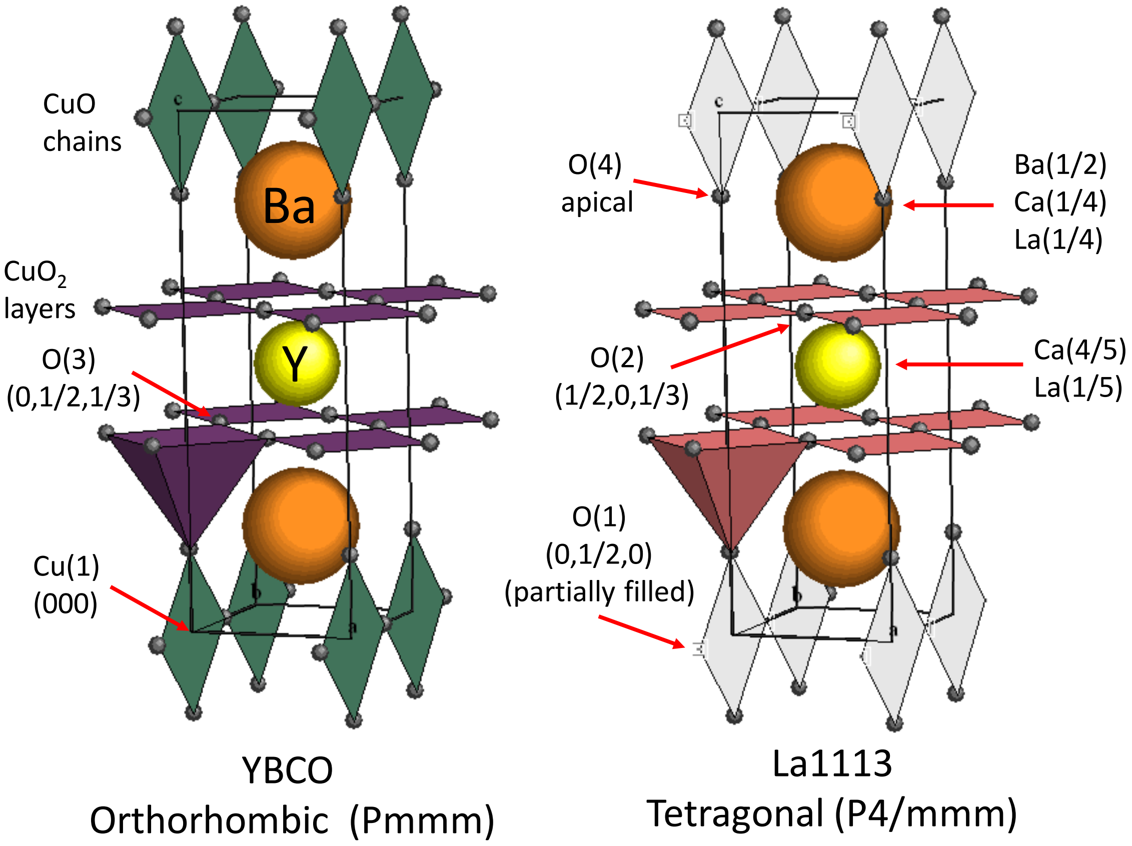

Figure 6.1: Comparison between YBCO (left) and La1113 (right) structures.

6.2 Experimental

La1113 superconductor grains were prepared by conventional solid state reaction (SSR) method in collaboration with Prof. Angel Bustamante (University of San Marcos, Peru), using the same procedure reported elsewere (Valladares *et al.*, 2004, 2006). Appropriate amounts of La_2O_3, $BaCO_3$, and CuO were mixed and ground in an agate mortar. A La1113 pellet of 1 cm^2 diameter was formed by pressing the powders at 4 tonne/cm^2 for 6 min. It followed three heat treatments (represented in Figure 6.2 (a)) in a tubular oven (LENTON LTF-PTF Model 16/610). First, a calcination at 950 °C for 24 h allowed the ingredients to stick toguether. The sample was then reground and sintered at 975 °C in air for 12 h before furnace cooling to room temperature (RT). After grinding for a third time to obtain uniform grains, the sample was annealed at 575 °C in oxygen flow for 24 h and furnace cooled to RT in the same gas atmosphere. Figure 6.2(b) shows the scanning electron micrograph of the grains obtained by this technique. As shown in the picture, the grains are different border shapes and sizes with small amount of nanograins. In order to improve the grain sizes in the nanoscale, the precursors before heat treatment were prepared by a co-precipitation method, following the same procedure reported more recently (Valladares *et al.*, 2010b) and in collaboration with Prof. Bustamante and his group. In brief, a solvent was obtained by dissolving stoichiometric amounts of $Ca(OOCCH_3)_2 1.4H_2O$, $La(OOCCH_3)_3 1.5H_2O$, $Ba(OOCCH_3)_2$ and $Cu(OOCCH_3)_2H_2O$ acetates in aqueous solution of ethanol (1:1) at room temperature. At the same time, a mixture of oxalic acid HCOO-COOH (2 gr) of aqueous solution and ethanol (200 ml) was prepared as a solute. Next, the solvent was dripped in the solute with continuous stirring, agitation and with control of the pH for 12 h at room temperature. After filtering for 3 h with the help of conical filter-paper No. 40, the sediment was dried at 40 °C for 48 h. The La1113 precursor obtained by this procedure was ground in an agate mortar and followed the heat treatments described above. A scanning electron micrograph of the sample obtained by this co-precipitation technique is presented in 6.2 (c). The grain sizes are in the nanometer scale and they are more uniform than those obtained by the solid state reaction method. The mean crystallite

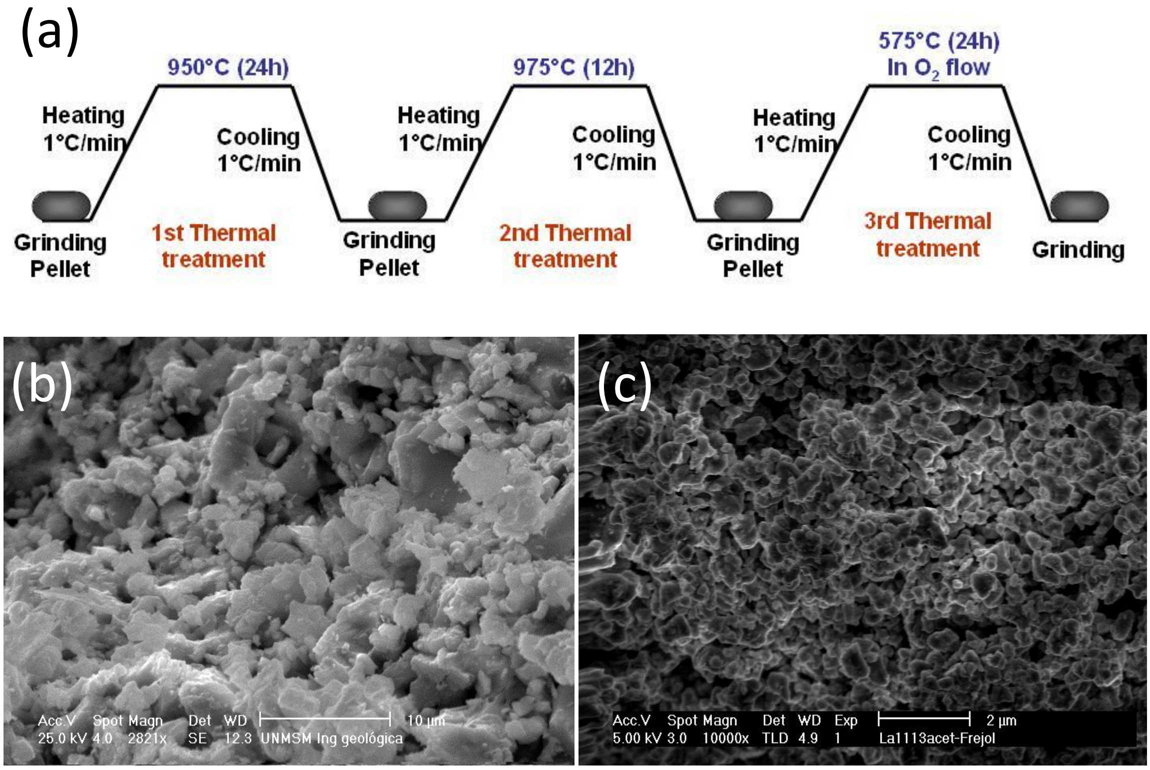

Figure 6.2: (a) Heat treatment for the preparation of the La1113 superconductor grains, (b) SEM micrograph of grains obtained by conventional solid state reaction method and (c) SEM micrograph of grains obtained by precipitation of precursors.

diameter obtained from XRD analysis (not shown here) by using Scherrer's formula is 73nm. The fact that nearly uniform grain sizes have been obtained after the preparation is important for potential electronic applications and magnetic analysis, since irregular grains imply grain boundaries with different areas and thus less-uniform Josephson junctions between superconducting grains, as we will see below.

In order to check if the superconductor La1113 grains can be immobilised on gold surfaces, which is required for potential electronic applications, a gold film was fabricated following the steps described in Chapter 3. In brief, gold was evaporated on a polished SiO_2 (2 μm)/Si(100) substrate using an Edwards 306 evaporator system with a base pressure of 10^{-7} mbar. The substrates (1×2 cm^2) were degreased in acetone and cleaned ultrasonically in isopropyl alcohol following a standard procedure before deposition. Small Au pellets (99.999% purity) were evaporated from a tungsten boat with the substrates located 10 cm above the source. The rate of evaporation was maintained at 0.1 nm/s and the thickness of gold (70 nm) was measured by a quartz crystal microbalance located next to the sample. A thin layer of Ti (3 nm) was used as adhesion promoter between Au and the substrates. In order to improve the crystallization of the gold in the [111] direction, post-deposition thermal treatment of the gold film was carried out by flame annealing as described in Chapter 3 and reported in our previous works (Valladares *et al.*, 2009a, 2010a). The gold film was placed horizontally over the conical blue zone of a flame generated by a propane torch for 25 s which is enough to obtain a Au(111) film with improved crystallinity. The film was then rapidly quenched by immersing it into a beaker of methanol and drying it in a stream of nitrogen. The substrate was then immediately immersed in 10 ml of 1 mM HS-C_8H_{16}-HS (Alfa Aesar B24693, octane (di)thiol) in ethanol for 72 h as shown in Figure 6.3 (top left). At the same time the La1113 grains (100 nm mean diameter) were functionalized by dispersing and mixing them in 0.5 ml of 4 mM of octane (di)thiol in ethanol for the same duration (Figure 6.3 (top right)). During this process, some particles stuck together forming groups and we observed that the number of groups increases with time and molarity. After 72 h part of the functionalized particles were dried at 45 °C for 30 min for its magnetic and electronic characterization, the remaining part was poured into a beaker containing 5 ml of ethanol and the washed gold substrate (as shown at the bottom in Figure 6.3). The system was left for 72 h at RT and finally rinsed with large amounts of ethanol to remove the unlinked particles from the substrate.

For the characterization, magnetic measurements of the dried samples were performed with a DC magnetic property measurement system (DC-MPMS-SQUID) of Quantum Design. External DC magnetic field in the range of -55 kOe to 55 kOe were applied to 21 mg of the functionalized La1113 at different temperatures (from 10 K to 290 K), in both zero-field cooling (ZFC) and field-cooling

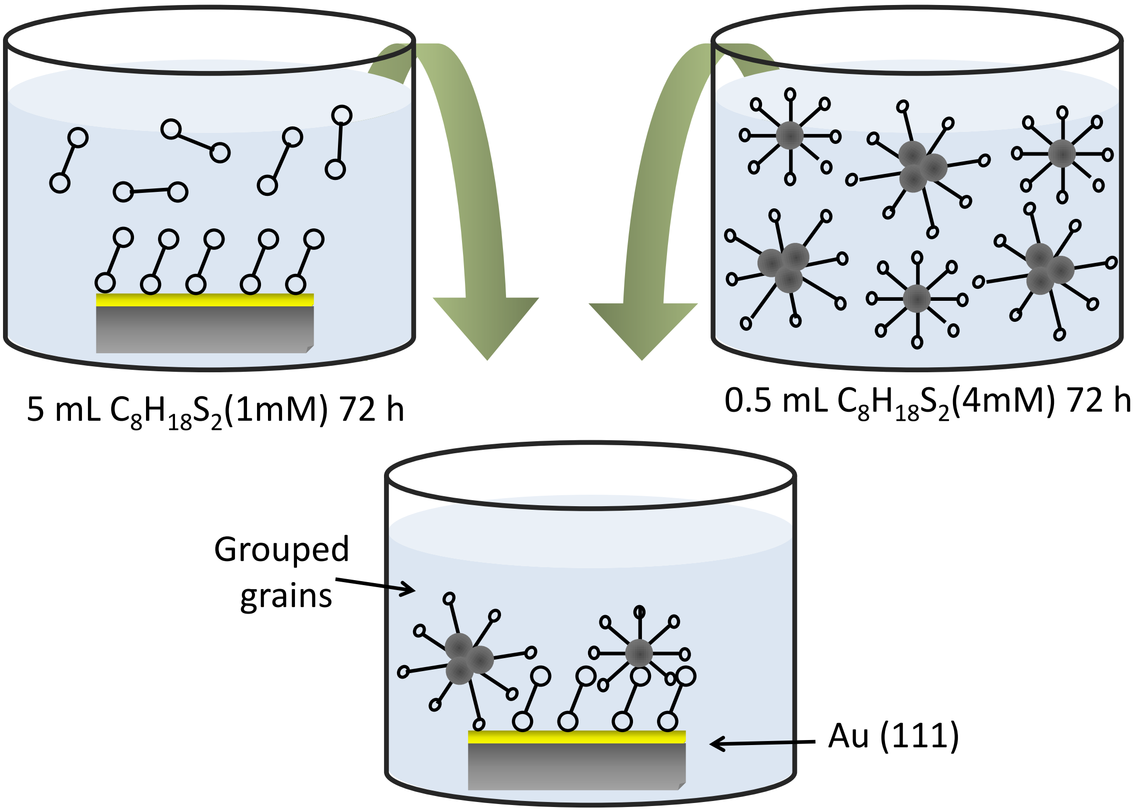

Figure 6.3: Self-assembled monolayers of octane (di)thiol (HS-C_8H_{16}-HS) on Au (111) surfaces (top left), functionalization of the La1113 particles with octane (di)thiol (top right), and La1113 particles attachment on the gold surface (bottom).

(FC) modes to obtain the magnetic phase diagram and thus the magnetic conditions required for potential application of the sample. The XPS was performed at SUPERESCA beam line, Elettra Sincrotrone, Trieste, Italy. Different photon energies were applied to obtain the core-level spectra (up to 650 eV) and the valence-level spectra (up to 200 eV), the data were collected at RT and 30 K in ultrahigh-vacuum environment (pressure $< 2\times10^{-9}$ mbar). The micrographs were taken using a scanning electron microscope (SEM; SFEG XL30).

6.3 Results and discussion

Following the procedure described above, it was possible to prepare, functionalize and attach La1113 superconductor grains on gold surfaces through a self-assembled monolayer (SAM) of alkane (di)thiols. Figure 6.4(a) shows an SEM micrograph of two linked La1113 grains of 100 nm diameter attached to the gold surface by SAMs of HS-C_8H_{16}-HS. In contrast to unlinked grains which are easily removed from the substrate by rinsing the sample with ethanol or propanol, the linked particles remain on the substrate after several washings and nitrogen streams. To facilitate the modeling between the superconducting particles and the gold substrate interfaces let us consider only one monolayer of HS-C_8H_{16}-HS. It is well known that the molecular axis is tilted only a few degrees with respect to the normal of the Au(111) surface (Chen & Li, 2006; Love *et al.*, 2005). Although no ionic, dipole-dipole, and hydrogen bonding interactions take place, the tethering of the thiol to the gold occurs by a combination of dative bonding (chemisorption) between sulfur and gold. It has been reported that the strong affinity of S for Au plays an important role in the stability of Au-thiols systems, whereas intermolecular van der Waals forces are responsible for the lateral packing of the layer (Hornyak *et al.*, 2008). Thus we can depict the SAM configuration between a particle and the gold surfaces as shown in Figure 6.4(b). However there are several considerations that are necessary to be taken into account with respect to the other end of the SAM, namely, that the La1113 is an oxide superconductor and according to some reports, the S linker cannot react directly with oxide layers (Vericat *et al.*, 2006). Therefore, to allow the thiol group to react with the La1113 crystallites it is necessary to eliminate first the passivation layer (usually CuO,

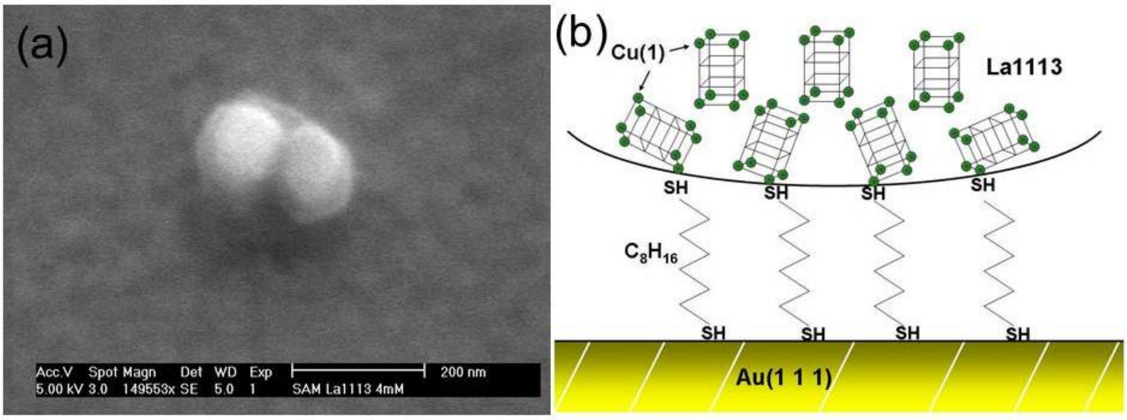

Figure 6.4: (a) SEM micrograph of a gold surface with two linked thiolated-superconducting grains attached, and (b) representation of the SAM linking the grains and gold surfaces.

$BaCO_2$, etc.) which surrounds the particles. This could be achieved by a redox reaction as we will discuss below. Once this is achieved, the thiol head finds the crystallites where the bare crystalline structures of the La1113 are located. As seen above (Figure 6.1) , the La1113 has two Cu atoms, one of them [Cu(1)] is situated in the charge reservoirs forming the CuO chains and the other [Cu(2)] is in the active planes forming the superconducting CuO_2 layers. It is reasonable to deduce that the SH functional heads bond only with those La1113 unit cells that are situated on the surface (Figure 6.4(b)). At this point, the important question is which atom of the La1113 structure binds to the SH head groups.

In order to elucidate better the binding between the SH functional heads and the La1113 superconducting grains, XPS measurements were carried out. Figure 6.5 shows the O 1s, S 2p and the valence-level spectra of the dry functionalized sample compared to the non-functionalized one. The measurements were taken at RT and 30 K in order to compare the behavior of the sample in its normal and superconducting state. In Figure 6.5(a), the O 1s peak belonging the La1113 band level at RT comprises three peaks, similar to that reported for YBCO (Weaver *et al.*, 1988), two of which originate from the oxygen atoms located on the CuO_2 superconducting planes and the other from the oxygen atom located on the CuO chains. After functionalization, the spectra show only one peak shifted by 1.5 eV which belongs to the oxidation of the attached octane (di)thiol; this peak is more intense and covers the previous one. At 30 K the O 1s photoemission peak of the La1113 spectra without functionalization is shifted by about 4 eV with respect to the RT one and shows different peak intensities. These responses are caused by the charge transfer between the charge reservoirs and the active planes in the superconducting state of La1113 which is typical of HTSs (Lynch & Olson, 1999). Similarly to RT, the high intensity peak caused by photoemission of the thiol oxidation screens the peaks of the La1113 oxygen atoms. Since the XPS sensitivity ranges from 1 to 2 nm deep depending on the kinetic energy of the photo-electrons (Briggs & Grant, 2003), the photoemission intensities of the oxygen atoms belonging to the La1113 crystallites inside the grains are mostly screened by the emission intensities of the oxidized octane(di)thiols attached on the surface. Scanning the S 2p band energy before and after functionalization, results in the spectra signals shown in Figure 6.5(b). At that band energy and at RT, the La1113 without functionalization shows two peaks, which are caused by the Ba photoemission which shares the positions with La and/or Ca in the La1113 structure (see Figure 6.1 in page 92). After functionalization, two peaks are notorious at 167 eV and 172 eV. It is obvious that these peaks do not correspond to the spin-orbit doublets S $2p_{3/2}$ and S $2p_{1/2}$ because they always appear together with 1.18 eV separation and 2:1 intensity ratio (Wagner, 1979). In the figure, the peaks indicate a large amount of oxidized sulfur species screening the barium peaks. The peak at 172 eV corresponds to sulfates (Lichtman *et al.*, 1981), whereas the peak at 167 eV corresponds to sulfonate formation (Sung & Kim, 2001). The same situation occurs at 30 K without appreciable variation in the intensities, the Ba, La, and Ca peaks belonging to the La1113 bare structure are screened by the sulfide peaks of the functional thiol groups. The sulfate formation is an indication that corrosion occurred during assembly, thus a redox reaction, in other words, the octane (di)thiol molecules have been oxidized, while probably the surface region of the superconductor was reduced commensurate with this oxidation. In that way some atoms of the exposed superconducting crystallites should have reacted with the thiol heads to form the sulfonates. If that is the case, one must consider that it is unlikely that S bonds La, Ca or Ba cations situated inside the structure and shielded by oxygen atoms (see the structure in Figure 6.1(b) on page 92) to form the sulfonate. Moreover, bonding the Cu(2) would affect the superconducting layers and thus destroy the superconductivity. This leads us to believe that the S atoms of thiols bond to the Cu(1) atoms situated in the vertices of the La1113 structure to form copper sulfonates, as represented in the inset of the Figure 6.5(b) (see also the Figure 6.4(b) on page 98). This could seem reasonable since it has been reported that Cu can chemisorb S atoms from thiols forming copper sulfonates (Ron *et al.*, 1998; Sung & Kim, 2001). To complete the XPS analysis, the spectra near the valence-band energy is presented in Figure 6.5(c). The Fermi energy (EF) level is represented by the O level in the figure and was referenced by a gold strip mounted on the same sample holder (E_F = 5.51 eV). At RT the more pronounced peaks are those belonging to the O 2s and the CuO chains. After functionalization (blue line) the main observed peak corresponds to the S 3p belonging to the attached (di)thiols on the grain surface. Nevertheless the shape of this line near the Fermi level decays faster than in the previous spectra. Such behavior implies that it has a lower density of states and thus it is more insulating. This can be understood taking into account that alkane thiols are insulators and since they cover almost all the surface a like-insulator response is sensed by the photoemission spectra. At 30 K, O 2s and CuO peaks are shifted indicating charge transfer in the superconducting state. However the thiolated spectra show that the sulfur peak of the thiol screens those peaks and confirms that the octane (di)thiol shields almost all the sample.

In order to check the effects of the functionalization on the superconductivity properties, M(T) measurements were performed in a MPMS-SQUID before and after functionalization at low temperatures. Figure 6.6 shows the M(T) dependence in ZFC and FC conditions. According to the figure, the onset critical temperature $T_{C(onset)}$ = 80 K of the La11113 is not affected after functionalization with HS-C_8H_{16}-HS. Nevertheless, the ZFC and FC loops of the La1113 fall to low values faster than when it is functionalized. The fact that the magnetic moment of a HTS at temperatures in the Meissner state turns to higher values (such as in the functionalized case in the figure) is an indication of the presence of impurity or secondary phases in the sample (Poole *et al.*, 2007). In effect, the functionalized sample contains on its surface carbon atoms and oxide which

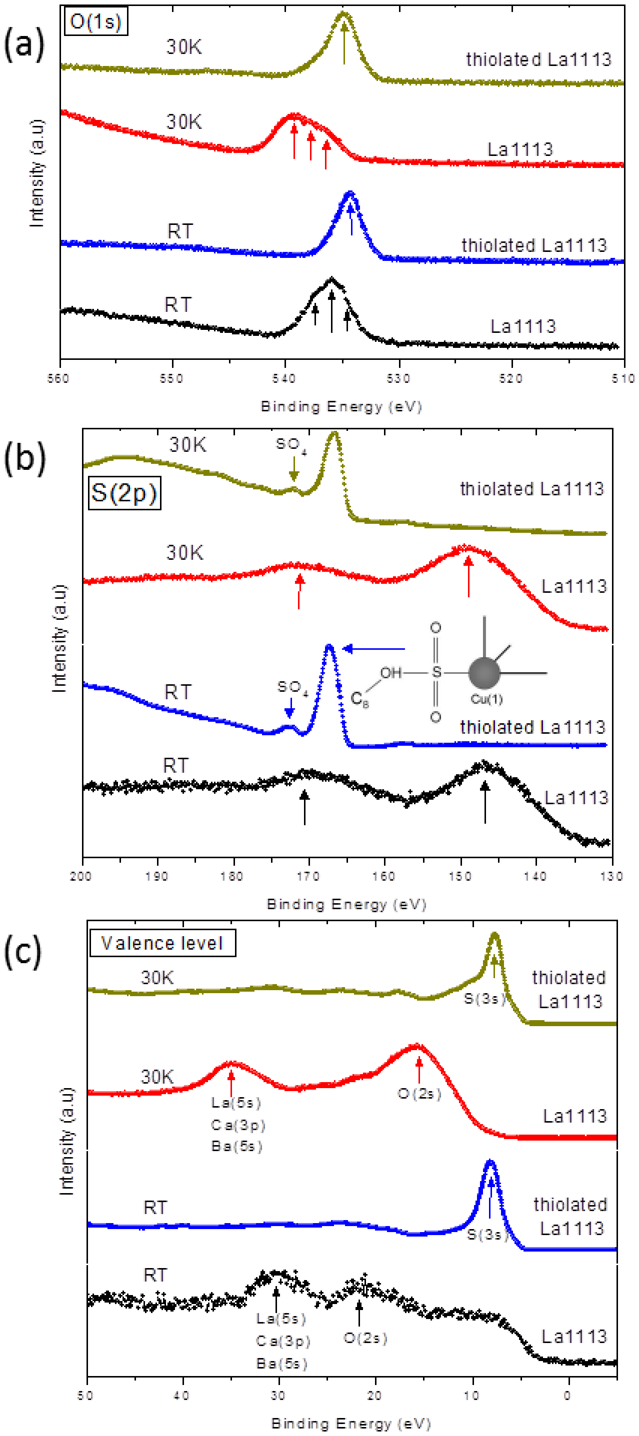

Figure 6.5: O 1s (a), S 2p (b) and valence (c) level XPS spectra for La1113 grains at room temperature and 30 K. The spectra of the sample from bottom to top in each graph: non-functionalized at room temperature (black), functionalized at room temperature (blue), non-functionalized at 30 K (red) and functionalized at 30 K (green).

belongs to the octane (di)thiol, thus its magnetic response behaves as in a "dirty" sample.

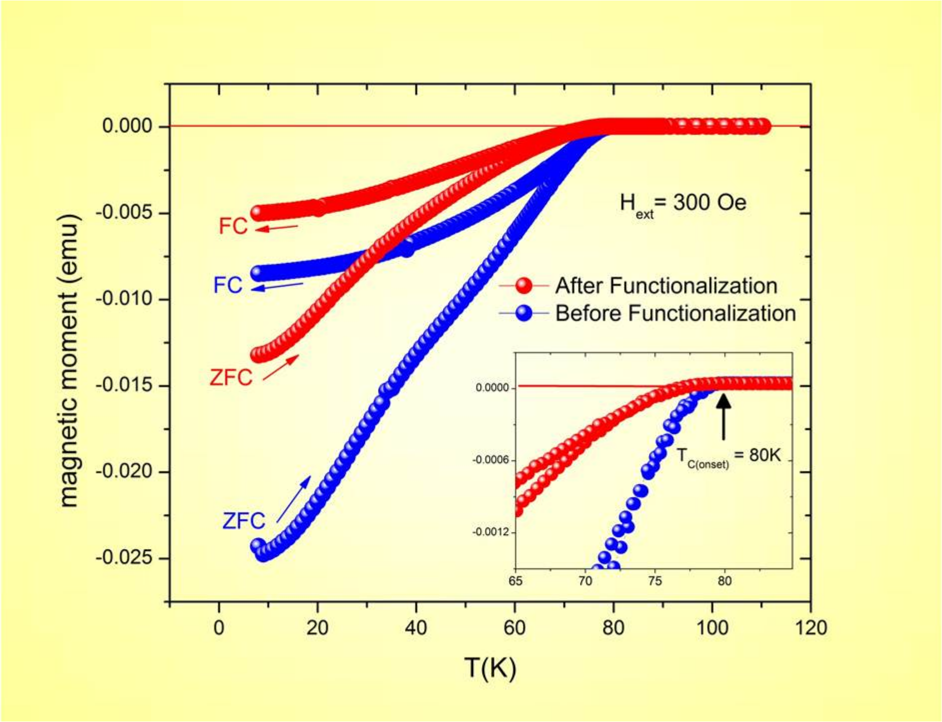

Figure 6.6: M(T) dependences of the La1113 before (blue spheres) and after (red spheres) functionalization with HS-C_8H_{16}-HS.

Now we calculate the magnetic phase diagram of the La1113 grains to obtain information about the magnetic conditions in which this superconductor could be applied. For this purpose, the temperature dependence of the magnetic moment in the superconducting state has been measured under different external magnetic fields. Figure 6.7(a) shows some of these measurements at ZFC and FC conditions, at H_{ext} = 5, 25, 100, 250, 500 and 1000 Oe. According to the figure, La1113 becomes diamagnetic from around the onset temperature 78 K and the diamagnetic saturation is reached at low temperatures. The transition widths for the diamagnetic saturation under H_{ext} = 5 Oe is better appreciated in the inset plot. A wide transition width of around 40 K is found for the sample under the indicated applied magnetic field. Wide transition widths in HTSs are mainly caused by its granular nature together with possible secondary phases, thus the grain boundaries could be considered then as weak Josephson junctions (Krabbes *et al.*, 2006). The irreversibility temperature T_{irr} (temperature which separates reversible and irreversible regions) is found in this work from each point in which the ZFC and FC M(T) loops start separation. For example, under an external applied magnetic field of 5 Oe as shown in the inset figure, $T_{irr} = 60$ K. In general, multiple T_{irr} obtained from different M(T) measurements define the irreversibility line in a magnetic diagram phase as it will be discussed next. Moreover, it is possible to derive the magnetic moment behavior as a function of different applied magnetic fields from multiple M(T) measurements, as shown in Figure 6.7(b) in which, as an example, the plot is derived for four different temperatures below T_C. In the plots, the peaks indicate the lower critical field H_{C1} and the upper critical field H_{C2}. The latter can be obtained from the intercepts with the abscissa (Poole *et al.*, 2007). Similar to the direct-measured hysteresis loops reported in the literature (Valladares *et al.*, 2010b), both critical fields tend to be high as the temperature approaches 0 K and they decrease continuously with increasing temperature until the transition temperature T_C where they become zero. Therefore, M(H) loops contract as temperature increases.

From the collected data and plots described above, we derived a magnetic phase diagram for the La1113 which is presented in Figure 6.8. The various parts of the diagram are explained in the following. As long as the external flux density does not exceed H_{C1}, the bulk La1113 is in a diamagnetic Meissner state, where the magnetic flux is completely expelled from the interior by surface currents. In the area between $H_{C1}(T)$ and $H_{C2}(T)$, the magnetic flux penetrates the bulk La1113 in the form of flux lines (mixed state). Magnetic flux motion has to be prevented by a flux pinning (F_P). As long as the flux lines are pinned, a maximum supercurrent density (J_C) can flow without any loss. This critical current density J_C depends on the applied magnetic field and on the temperature. If the current density exceeds J_C ($H_{irr} < H < H_{C2}$), then the flux line lattice (or parts of it) starts to move. Because of thermal fluctuations, the mobility of the flux line lattice strongly increases with applied magnetic field and temperature. Above the irreversible field H_{irr} the vortex lattice becomes so strong that currents cannot flow without losses although the superconductor La1113 is not yet in the normal

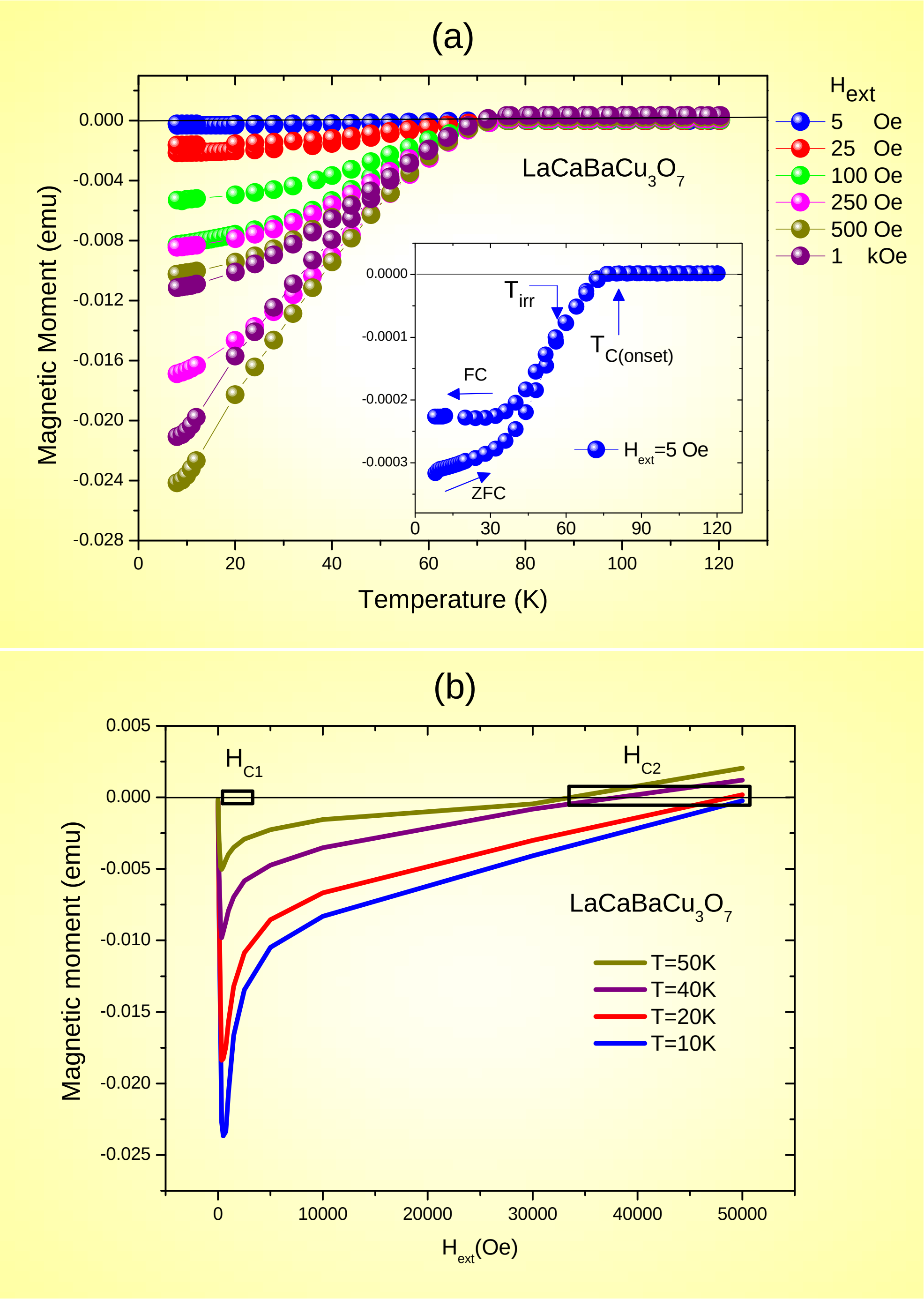

Figure 6.7: Magnetic response of the LaCaBaCu$_3$O$_7$ as (a) a function of temperature under different external magnetic fields, inset: M(T) at $H_{ext} = 5$ Oe (the arrows indicate T_{irr} and $T_{C(onset)}$) (b) function of the applied magnetic field for four different temperatures below TC.

state. This means that possible applications of La1113 are restricted to the field range below H_{irr}. To a first approximation, H_{irr} scales with the applied field following the trend:

$$H_{irr} = H_{irr(0)} \left(1 - \frac{T}{T_C}\right)^n \tag{6.1}$$

Where $H_{irr(0)} = 48$ kOe, $T_C = 76$ K and the exponent n is one of the factors which provides indication of the superconductor applications (it usually varies considerably in different HTSs (Felner *et al.*, 1989; Müller *et al.*, 1987; Yeshurun & Malozemoff, 1988; Yeshurun *et al.*, 1987). The shape of the irreversibility field line obtained here is quite similar to that obtained for YBCO in the range 55 - 90 K (Küpfer *et al.*, 2000). The exponent n in the temperature range 41 - 76 K is 2.8, this value is double that obtained for bulk YBCO ($n \approx 1.4$). Interestingly, Küpfer *et al.* have found that after reducing the oxygen content in the structure of YBCO, H_{irr} shifts to lower values. Although La1113 has a similar structure to YBCO with deficiency of oxygen in the CuO chains (see Figure 6.1 in page 92) and the shape of the irreversibility line similar to YBCO, we cannot assure that n and the low irreversibility line are exclusively originated by the arrangement of oxygen atoms in the structure, because the crystallite boundaries and secondary phases might contribute to this property as well. Eventually, extrapolating H_{C2} and H_{C1} in the figure to T = 0, values of $H_{C2(0)} \approx 53.5$ kOe and $H_{C1(0)} \approx 0.5$ kOe can be estimated.

As discussed above, La1113 is a type II superconductor at the boiling temperature of liquid nitrogen. In contrast to YBCO which at 77 K can support external magnetic fields up to 6×10^4 Oe, or even more depending on its purity (Krabbes *et al.*, 2006); La1113 can support less than 1×10^4 Oe under the same conditions without losing its superconductivity (Valladares *et al.*, 2010b). This characteristic could be useful for the fabrication of superconducting transistors controlled by relatively low applied magnetic fields as a transistor gate. Figure 6.9 shows a design of an external magnetic field-gated superconducting transistor, in which, with the help of alkane (di)thiols, a superconductor nanograin bridges two gold (or other metal) electrodes, the source (S) and the drain (D). Through change of the amount of the SAMs, one could vary the electron transport injection, i.e.

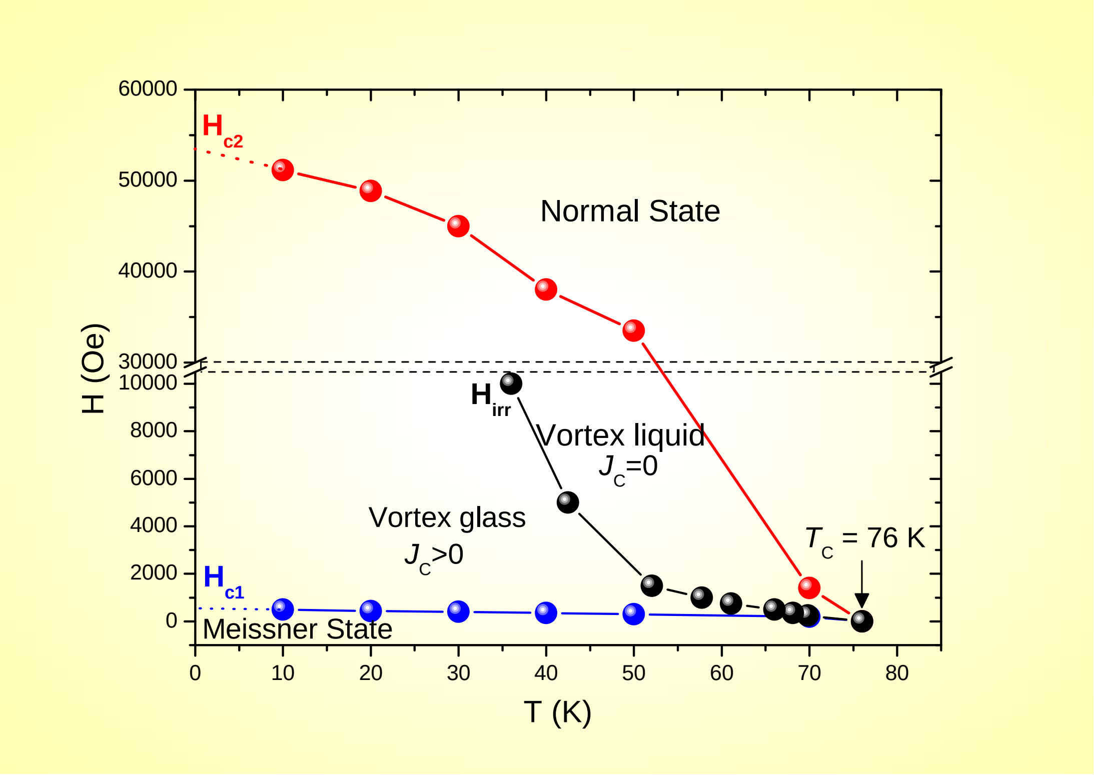

Figure 6.8: Magnetic phase diagram of the $LaCaBaCu_3O_7$.

charge transfer, electron tunneling or the resistances R_1 and R_2. At $T < T_C$, the application or absence of the upper critical magnetic field ($H = H_{C2}$), can be used to control the device. The superconducting or non-superconductor states can be achieved by simply turning “on” or “off” $H = H_{C2}$ in order to allow the current flowing to two corresponding states of block/pass (or off/on). In this way the external H could control the superconducting nano-device like a transistor gate. For instance, taking an applied voltage (at the drain) V_D=1 and the field $H = H_{C2} = 1$ units, and considering the presence/absence of the resulting voltage as 1/0; the result is that if $H = 0$, $V = 1$ and vice versa if $H = 1$, $V = 0$; the proposed transistor thus work as an inverter switch. Logic gates such as AND or NOR could be obtained using two of these inverters in series or in parallel respectively. Further digital circuits can be logically built on combinations of various logic gates. Eventually, partial conduction could be achieved when the external field is set to values $H_{C1} < H < H_{C2}$.

6.4 Conclusions

In summary, it has been proved that the high T_C superconductor $LaCaBaCu_3O_7$ nanograins can be linked to Au(111) surfaces through self-assembled monolayers of HS-C_8H_{16}-HS. These molecules can be adsorbed on the surface of La1113 nanoparticles without destroying its superconducting properties. X-ray photoemission spectroscopy (XPS) analysis suggests that links are mediated by the formation of copper sulfonates originated by the S atoms of the thiol heads and Cu(1) atoms of the La1113 structure. These functionalized particles can be immobilized on gold electrodes and they can be used for the fabrication of electronic nanodevices such as magnetic-field-gated superconducting transistors. The irreversibility line in the magnetic phase diagram of the La1113 grain fits and exponent trend n suggest that this superconductor can support low applied magnetic fields, for example at 70 K, the superconductivity is destroyed by applying 2 kOe magnetic field. Thus La1113 superconducting grains are promising candidates to fabricate nanotransistors controlled by external magnetic fields.

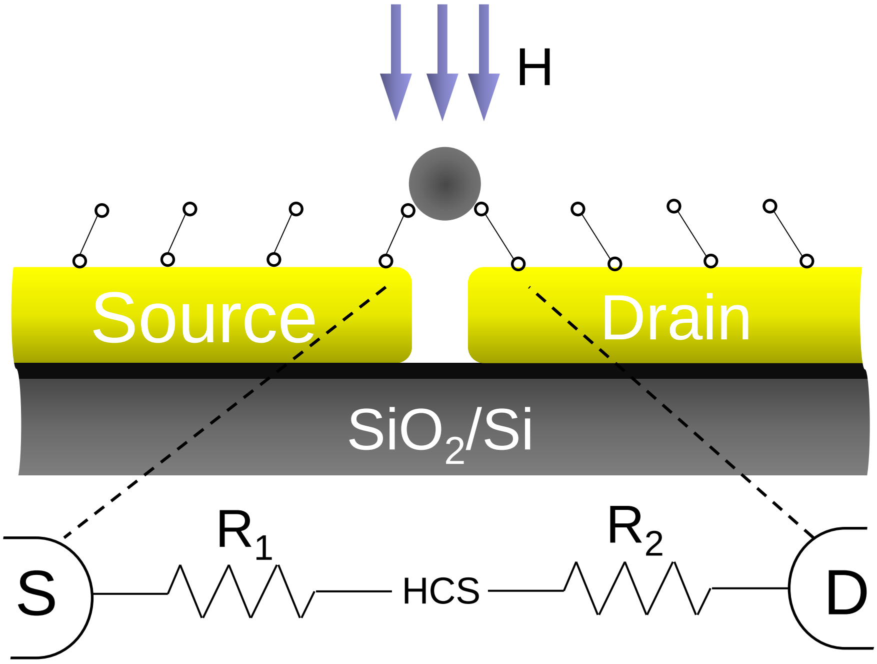

Figure 6.9: Design of a magnetically gated superconduting transistor (top) and its corresponding electrical representation (bottom).

Chapter 7

Carboxyl ferromagnetic microspheres: Reorientation response under an applied magnetic field

In this chapter, the mechanical reorientation of thiolated ferromagnetic microspheres bridging a pair of gold electrodes under an external magnetic field is studied. When an external magnetic field (0.7 T) is applied during the measurement of the current-voltage characteristics of a carboxyl ferromagnetic microsphere (4 μm diameter) attached to two gold electrodes by self-assembled monolayers (SAMs) of octane di-thiol ($C_8H_{18}S_2$), the I-V trace becomes distorted. Instead of magnetoresistance, this effect is caused by a mechanical reorientation of the ferromagnetic sphere, altering the number of SAMs between the sphere and the electrodes and thus modifying the conduction in the system. The physical reorientation of the ferromagnetic particles is studied by measuring their hysteresis loops while suspended in a liquid solution.

7.1 Introduction

As part of the continued drive to shrink electronics circuits in order to maintain Moore's law (Moore, 1965), researchers have managed to attach individual molecules and nanostructures to nanogap electrodes to form single-electron transistors (SETs) and have measured their electrical conductance. However, fabricating reliable SETs is extremely challenging due to the lack of direct observation confirming the presence of a particular molecule on the junction of the device and the great care required during assembly. The experimental results usually differ from the theory and an exact explanation of the characteristics of the structures becomes difficult. For instance, recently, molecular switching has been observed in an endohedral metallofullerene which, following a careful analysis of the current-voltage characteristics, was shown to arise from a reorientation of this molecule caused by the interaction between its electric dipole moment and an external electric field (Yasutake *et al.*, 2005). Nevertheless, the situation becomes more difficult in single molecules or nanostructures carrying a magnetic moment, since only a few experiments have succeed in fabricating SETs based on magnetic structures (Bogani & Wernsdorfer, 2008; Roch *et al.*, 2011; Zyazin *et al.*, 2010). Microstructures are easier to assemble on metal surfaces (Long *et al.*, 2005; Valladares *et al.*, 2010c) and thus a study of these reliable systems with easier-to-interpret characteristics is helpful for a prior understanding of more complex systems. In this work, we report the reorientation of a ferromagnetic microsphere attached to a pair of gold electrodes and its effect on the current-voltage characteristics in the presence of an external magnetic field.

7.2 Experimental

The fabrication of the samples comprised many steps. Photo-lithographically defined arrays of gold electrode pairs, separated by 2 μm gaps, were patterned by a conventional evaporation and lift-off process. Small Au pellets (99.999% purity) were evaporated from a tungsten boat on polished SiO_2(80nm)/Si(100) substrates using an Edwards 306 evaporator system with a base pressure of 10^{-7} mbar. The rate of evaporation was maintained at 0.1 nm s^{-1} and the thickness of gold (40 nm) was controlled by a quartz crystal microbalance located next to the substrate. The gold electrodes were functionalized with $C_8H_{18}S_2$ (octane di-thiol, Alfa Aesar B24693) following standard procedures (Ulman, 1996). In parallel, carboxyl ferromagnetic spheres of mean diameter 4 μm (CFM-40-10, Spherotech Inc.) with polystyrene cores and iron oxide shells were dried, suspended in distilled water or coated with octane di-thiol ($C_8H_{18}S_2$). The latter were obtained by dispersing and mixing the ferromagnetic spheres in 0.5 ml of 2 mM octane di-thiol in ethanol for 48 h. During this process, some spheres stuck together forming groups and we observed that the number of groups increases with time and molarity. The coated spheres were transferred to a beaker containing 5 ml of ethanol and the functionalized electrodes. The system was left for 48 h at room temperature (RT) and finally rinsed with large amounts of ethanol to remove the unlinked spheres from the substrate. The final sample consisted of thiolated ferromagnetic microspheres bridging pairs of gold electrodes by self-assembled monolayers (SAMs) of octane di-thiol. Current-voltage (I-V) measurements of the system were performed in a probe station Grail10-205-LV Nagase Techno-Engineering Co. LTD, at RT and in a high vacuum of 8.6 x 10^{-3} Pa. Two BeCu electrodes (source (S) and drain (D)) were in direct contact with a pair of the gold electrodes and the current response was sensed in the drain electrode after applying a source-drain bias in the range -5 to +5 V (in forward and reverse mode). An external magnetic field of 0.7 T was switched on in-plane to study the physical response of the spheres during the electrical measurements. In order to understand the mechanical motion of the ferromagnetic spheres under external magnetic fields, the samples were suspended in a liquid solution and the magnetic hysteresis loops were measured in a Magnetic Property Measurement System (MPMS-SQUID) from Quantum Design. Since the density of the distilled water is too low to hold the spheres in suspension over long timescales (4-6 h are required to acquire data from the magnetometer), the spheres were suspended in a sucrose liquid solution as better described in our previous work (Valladares *et al.*, 2009b) and in §2.4. In brief, 3 g of sucrose (sigma Ultra 99.55 GC) was diluted in 6 mL of distilled water to suspend the spheres and to avoid sedimentation. Since the standard holder for the MPMS consists of a simple gelatine capsule designed especially for powder and dried samples, a new sample holder consisting of a diamagnetic cone plastic was fabricated to hold the liquid solution (see Valladares *et al.* (2009b) and Figure 2.10 on page 30). A drop of approximately 1 μL of suspended spheres in the solution was measured in the MPMS equipment.

7.3 Results and discussion

Figure 7.1 shows arrays of gold electrodes in which the CFM microspheres are attached through SAMs of octane di-thiol. The linking of the thiols to the gold occurs by a combination of dative bonding (chemisorption) between sulphur and gold as has been reported elsewhere (Ulman, 1996). The immobilization of the spheres at the electrodes is mediated by the strong affinity of the sulphur atoms of the functional group and gold, whereas intermolecular van der Waals forces are responsible for the lateral packing of the layers (Ulman, 1996). Despite the fact that it is not clear that chemisorption or physisorption of thiols occurs on the carboxyl surface of the sphere, strong immobilization of them to the electrodes was indeed tested via several washings of ethanol, propanol and distilled water. The system thus ensures that the spheres do not detach from the electrodes when an external magnetic field is applied. In Figure 7.1(a) the optical microscope image at 50 × magnification shows groups of thiolated microspheres indicating long-time functionalization. In contrast, in Figure 7.1(b), individual microspheres are attached to the gold electrodes. This was achieved by adjusting the functionalization time to 48 h. The less distinct image of the microspheres in Figure 7.1(b) is caused by the diffraction of light through the optical microscope at the chosen magnification (75 ×).

Figure 7.2 shows the I-V response of an arbitrary individual iron-coated polystyrene (CFM) sphere attached to two gold electrodes. Initially, in the absence of the sphere, a tunnelling current is detected and the forward and reverse bias superpose as shown in Figure 7.2(a). This superposition remains after several scans and indicates mechanical and electrical stability of the system. After bridging the electrodes with a thiolated microsphere, a similar tunnelling current and superposition on the forward and reverse bias is observed with increasing magnitude of the current. This increase is generated by the higher conductivity of the SAMs-sphere-SAMs bridging the source and drain electrodes and represents a lower electrical resistance than in the empty case, as expected. However, the situation changes when an external magnetic field is applied. As shown in Figure 7.2(b), as soon an external magnetic field of 7 kG is switched on, the current signal is distorted. The response of the current for forward bias does

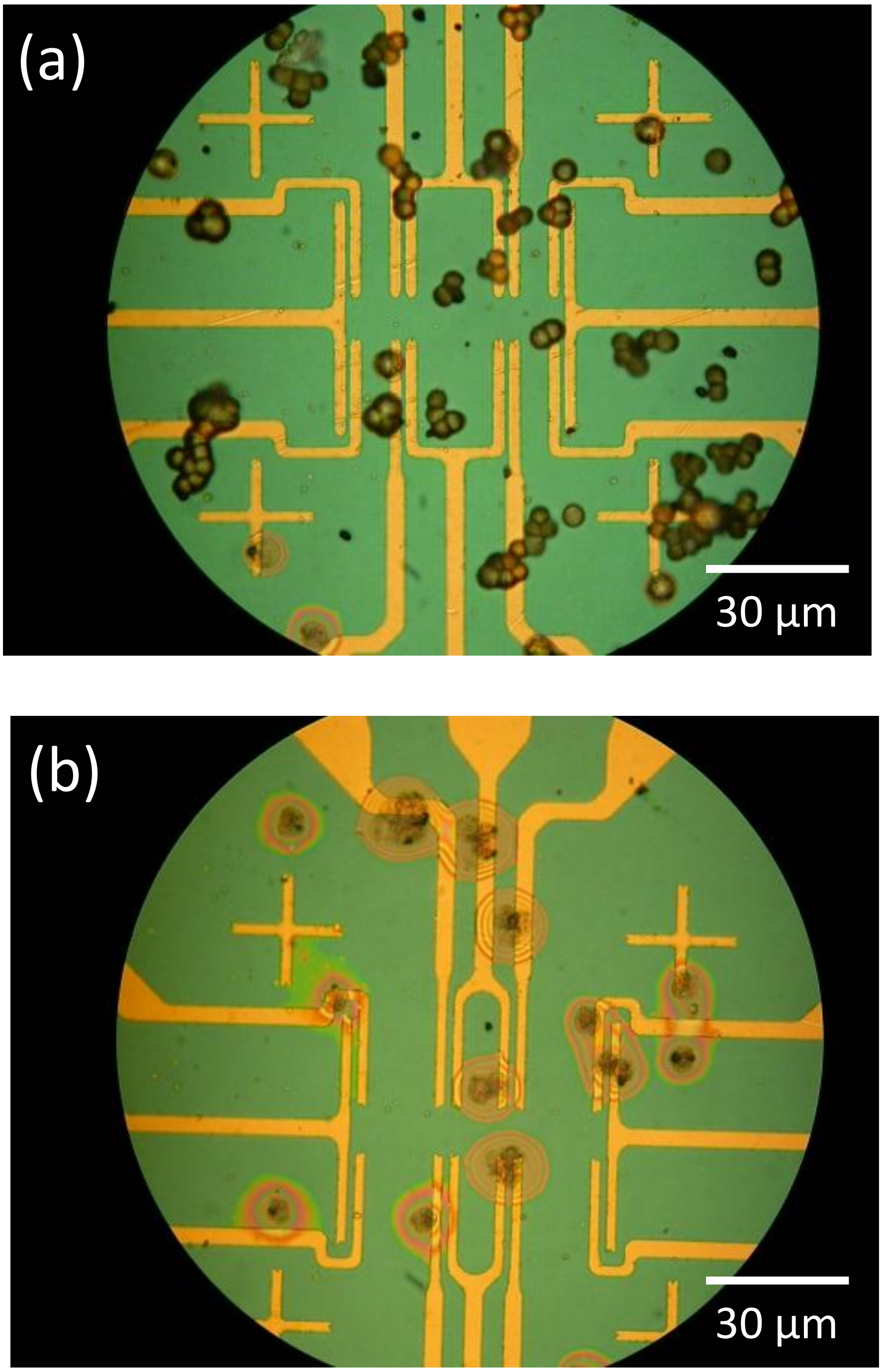

Figure 7.1: Optical microscope images of multiple microspheres (magnification 50× (a)) and individual microspheres of 4 μm mean diameter (magnification 75× (b)) bridging gold electrodes.

not match that of the reverse bias. Change of the resistance in the presence of magnetic fields (magneto resistance) has been widely observed, mainly in charge transport through iron nanostructures directly (Guo *et al.*, 2008; Parkin, 1995). However, the transport mechanism in the microspheres presented in this work is completely different. It is unlikely that the current passes the carboxyl/iron coating and the polystyrene core since the current should flow through the SAMs and carboxyl surface of the sphere. Therefore, the I-V distortion may originate from inertial mechanical vibration of the microsphere in response to the applied magnetic field. The decrease in the magnitude of the current in the reverse bias from -2 to -5 V to lower values should originate from a decrease in the number of self-assembled monolayers (SAMs) between the sphere and the electrodes.

To understand better the mechanical movement of the ferromagnetic microspheres under an external magnetic field, magnetic hysteresis loops of immobilized and suspended microspheres were studied. Immobilized hysteresis loops were obtained from dried and packed microspheres, whereas suspended hysteresis loops were taken after suspending them in a sucrose liquid solution as explained above. Figure 7.3 shows the hysteresis loops of the magnetic microspheres under three conditions: immobilized, in liquid suspension without thiol coating and in liquid suspension after thiol coating. Figure 7.3(a) shows the comparison between the hysteresis loop of the immobilized microspheres and the suspended spheres. It can be noticed that when immobilized, a classic hysteresis loop of a ferromagnetic material is observed. The remnant magnetization point is half of the saturation obtained at around 0.4 T. [1] In the figure, the scattered points in the suspended loop are probably noise caused by the motion of the spheres. When saturation is reached, most of the magnetic moments of the spheres are aligned with the external field and from then the diamagnetic behaviour of the plastic container is observed, giving a downward trend to the plots. In contrast to the immobilized case, the hysteresis loop of the suspended spheres does not display a coercive field. Figure 7.3(b) shows the comparison between the hysteresis loops of the

---

[1] The saturation magnetization is around 0.1 emu, and according to the information in the SPHEROTECH .INC datasheet, there are around 2.3×10^8 microspheres /mL. It means that, 0.5 mL of microspheres/DI water solution contains 1.15×10^8 microspheres. Therefore, the magnetic moment of each individual microsphere is around $0.1/1.15 \times 10^8 = 8.69 \times 10^{-10}$ emu.

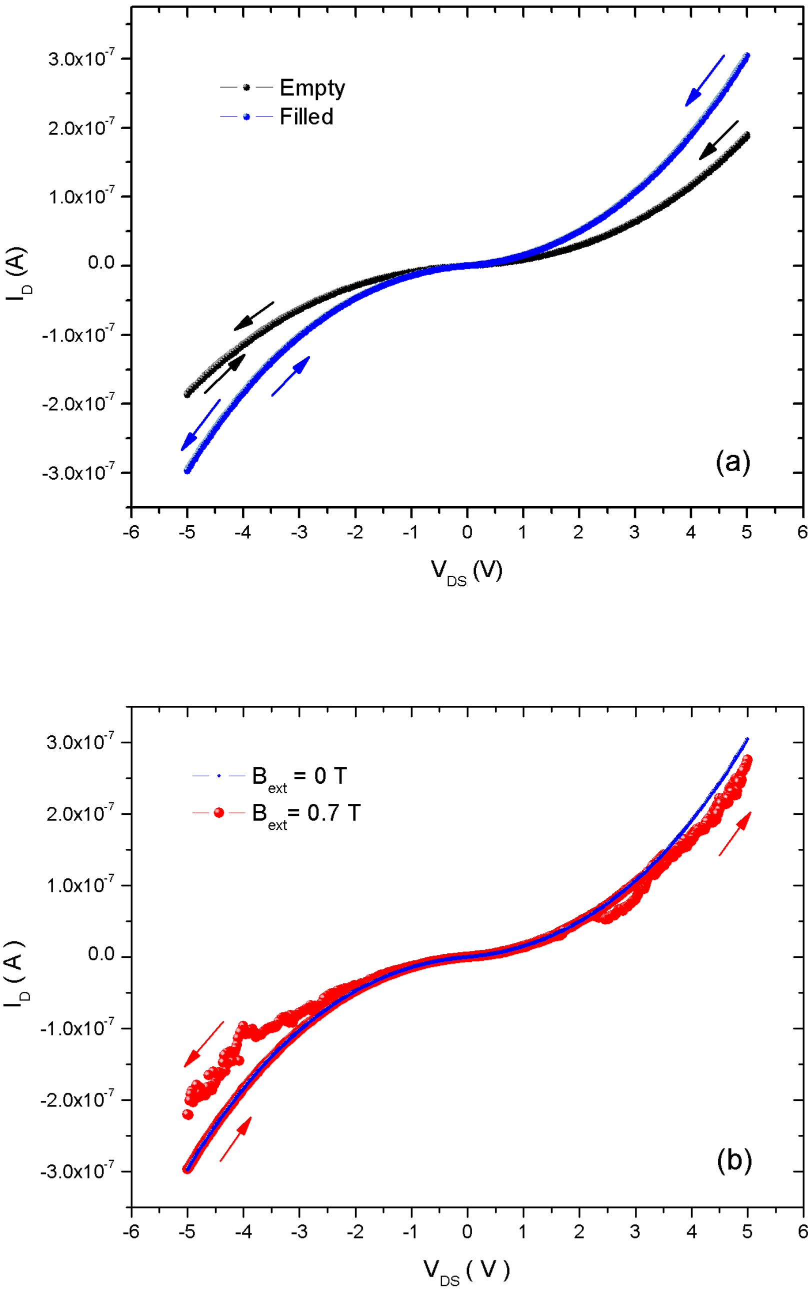

Figure 7.2: I-V responses of a particular CFM microsphere bridging two gold electrodes by SAMs of octane di-thiol: (a) comparison of the I-V signals before and after bridging the electrodes with a microsphere, and (b) comparison of the I-V signals with and without an external magnetic field.

immobilized ferromagnetic spheres and the thiolated spheres in suspension. The behaviour of the magnetization is similar to the previous case. The reason for the absence of coercivity in the hysteresis loops of the suspended ferromagnetic spheres is because the magnetic moments abruptly switch to align with the applied magnetic field when it reverses. Since the spheres are suspended in a liquid medium, they have more degrees of freedom (translation and rotation) than in the immobilized case. When the direction of the external magnetic field reverses, in addition to the magnetic moment orientation, the suspended spheres physically rotate. This is essentially a reversible process and hence the loops exhibit zero coercivity. In the immobilized case, this is not possible; since all the spheres are packed or are stuck together, only reorientation of the magnetic moments occurs. As mentioned above, the noise in the hysteresis loops of the suspended case is caused by motion of the spheres. The spheres are not completely static because the sample holder is in continuous vertical motion during the scanning of data in the MPMS-SQUID equipment and hence the relative position of the spheres varies. However, in equilibrium, the gravitational force, F_G, of a particular sphere is equal to the buoyancy force, F_B (see Figure 2.11 in page 31). The magnetophoretical force, F_M, generated during application of the magnetic field over the sphere is compensated by a drag force (F_D), especially when the external magnetic field changes value (see section 2.4 in page 27). When the applied magnetic field changes value in the MPMS, it is not uniform and F_M appears (Equation 2.19 on page 32) and the microsphere moves slightly over the applied field direction, resulting in a change of the exact position of the sphere detected by the SQUID and hence the noise is produced. The vertical movement of the sphere due to this change causes F_D (see Equation 2.20 on page 32). This force tries to minimize the sphere displacement (Valladares *et al.*, 2009b). As the spheres accelerate, the drag force increases, causing a decrease in the acceleration. Eventually a force balance is achieved when the acceleration is zero and the maximum or terminal relative velocity is reached or when applied field becomes constant in the MPMS equipment. At this point not all the spheres return to their original position.

From the discussion above, an external magnetic field tends to displace and rotate the CFM microspheres. A representation of a microsphere attached to the

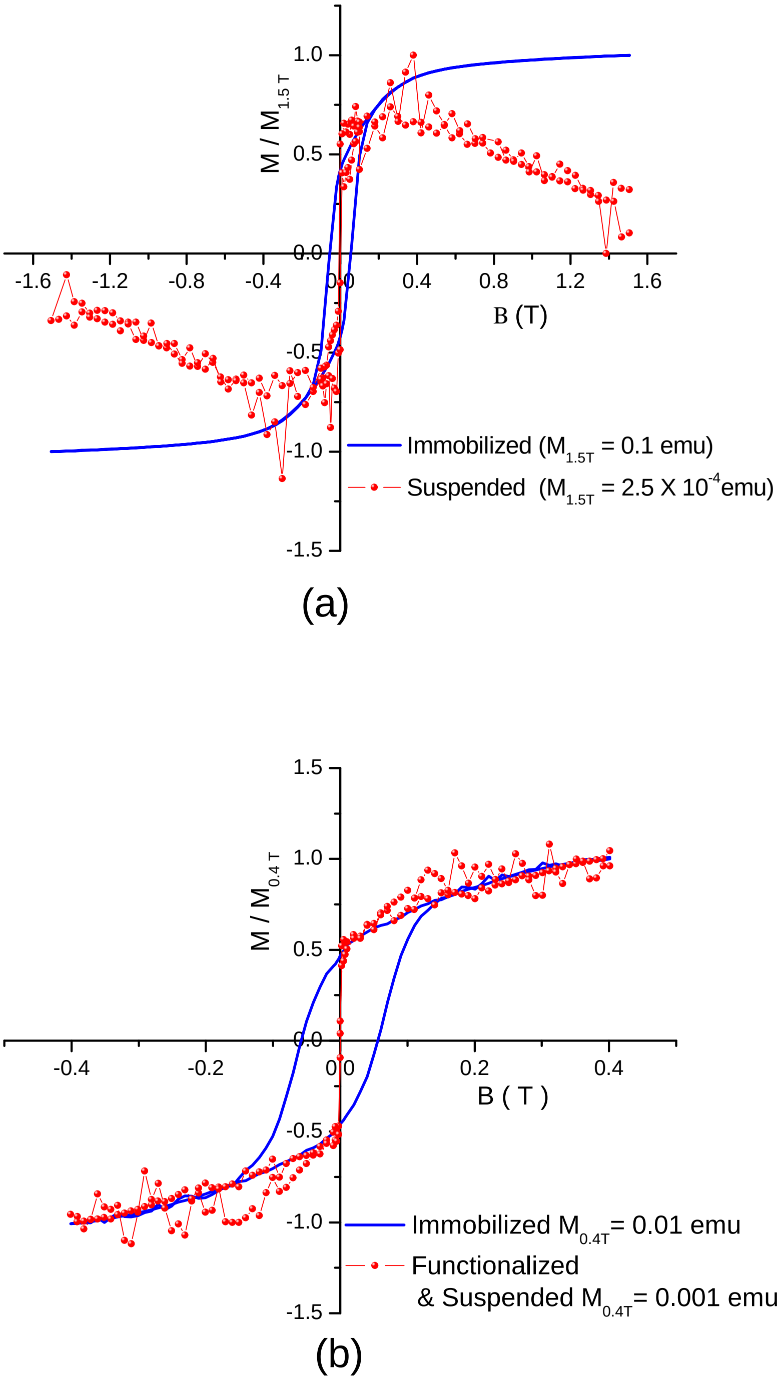

Figure 7.3: Hysteresis loops of ferromagnetic microspheres in three conditions: dried, suspended and functionalized suspended: (a) Comparison between dried and suspended and (b) comparison between dried and functionalized and suspended.

gold electrodes is presented in Figure 7.4. The sphere is immobilized between the gold electrodes by the SAMs of octane di-thiol which are not shown in the figure. When the applied magnetic field is switched on, the sphere tends to move towards the direction of field. However, the sphere cannot be completely detached from the electrodes. Translation and rotation inertia promote a slight vibration of the sphere. This may to the number of SAMs in some areas of contact to decrease, thus altering the conductivity, as observed in Figure 7.2. The fact that the microspheres respond under external magnetic fields when attached to the electrodes could be helpful when characterizing SETs fabricated with magnetic nanostructures which up to now have been only studied theoretically (Waintal & Brouwer, 2003).

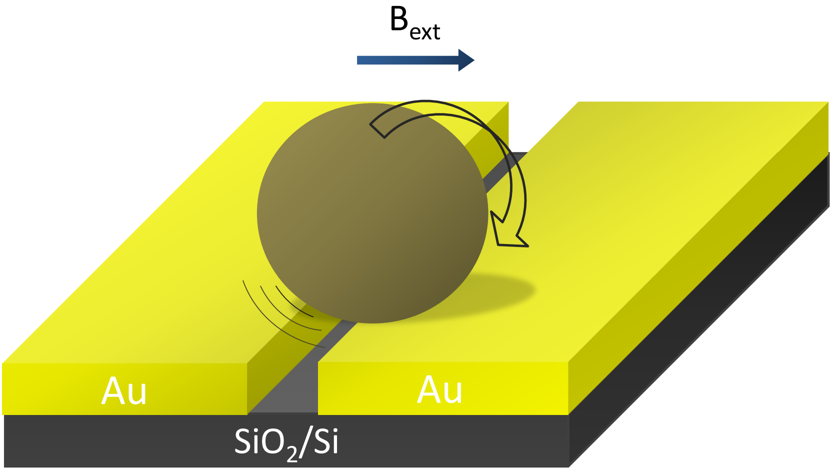

Figure 7.4: Representation of the reorientation response of a carboxyl ferromagnetic microsphere (CFM) attached to two gold electrodes by self-assembled monolayers of alkane di-thiol.

7.4 Conclusions

In summary, when an external magnetic field is applied to a system consisting of a ferromagnetic sphere bridging two gold electrodes by self-assembled monolayers of alkane-(di)thiol, the sphere tends to physically move in the direction of the field causing the number of linkers to decrease and resulting in a disturbance in the current-voltage signals.

Chapter 8

Graphene oxide flakes: Preparation and X ray diffraction

In this chapter, I describe the preparation of a flexible film made of graphene oxide flakes and its characterization by X-ray diffraction (XRD). Following chemical oxidation of commercial graphite and subsequent reaction with NaOH, structurally distorted graphene oxide flakes are obtained. X-ray diffraction reveals that the interlayer distance between graphene sheets increases by oxidation due to the formation of chemical groups and results in the delaminated flakes which can form a flexible film of multiple graphene oxides.

8.1 Introduction

Different two-dimensional carbonaceous layers are described in this section in order to understand better the formation and structure of the graphene oxide flakes prepared in this work. Graphene, graphene oxide and graphane are described and their principal characteristics are listed in the table 8.1.

8.1.1 Graphene

Graphene (G) is an allotrope of carbon; its crystalline structure is planar hexagonal based on sp^2-bonded carbon atoms. Many graphene sheets stacked together with interplanar spacing of 3.3 Å form graphite. Graphene is also the basic structural element of some carbon allotropes including charcoal, carbon nanotubes and fullerenes and can be considered as an indefinitely large aromatic molecule. Table 8.1 summarizes some properties of the planar graphitized layers. As indicated in the table, graphene allows a carrier mobility of around 15000 $cm^2V^{-1}s^{-1}$ which is comparable to the best Si metal oxide field-effect transistors (MOSFET) at low temperature. In addition, graphene mobility is relatively temperature-independent, making room-temperature 2D graphene mobilities among the highest of the field effect transistor (FET) devices. However, transport mechanisms in graphene are still not completely understood. Although many characteristics have been reported in the transport experiments, two have been highlighted and particularly discussed in the literature: (i) The low-density "minimum conductivity" σ_0, which is the value of the conductivity at or near the Dirac point ($E_F \approx 0$). And (ii) the high-density conductivity σ_n, which is linear with respect to the carrier density n, giving a constant mobility $=\sigma/ne$. The temperature-independence of the mobility of carriers between 10 K and 100 K (Chen *et al.*, 2008b; Morozov *et al.*, 2008; Novoselov *et al.*, 2005) has been explained in terms of charged impurity scattering (Adam *et al.*, 2007). Furthermore, it has been reported that dopants influence the carrier mobility in graphene, but some initial properties can be recovered after heating the graphene (Chen *et al.*, 2008a; Schedin *et al.*, 2007). For example, potassium ions can reduce the mobility 20-fold, and this mobility reduction is reversible after removing potassium from the graphene by annealing (Adam *et al.*, 2007).

8.1.2 Graphene oxide

When graphene is oxidized, the oxygen atoms are adsorbed on its surface forming epoxy C-(O)-C groups (Lee *et al.*, 2010). Graphene oxide is obtained by oxidation of graphite (Brodie, 1859; Hudson *et al.*, 1997; Hummers & Offeman, 1958; Staudenmaier, 1898). Graphite oxide is very sensitive to humidity (Hofmann *et al.*, 1934), and easily adsorbs HO_2 which increases the interlayer distance (Lerf & Buchsteiner, 2006) and allows other species to intercalate the layers. The extensive presence of saturated sp^3 bonds, the high density of electronegative oxygen atoms bonded to carbon and other “defects” give rise to the energy gap in the electron density of states (Boukhalov & Katnelson, 2008) and makes graphene oxide non-conducting. Some properties of graphene oxide are listed in Table 8.1.

8.1.3 Graphane

Graphane is hydrogenated graphene and it is believed that it has a puckered structure (Savchenke, 2009). It has been found that graphane behaves as an insulator and its resistivity grows by two orders of magnitude when the temperature decreases from 300 to 4 K (Elias *et al.*, 2009). In contrast to graphene, ambipolar field effect with the neutrality point near zero-gate-voltage has not been observed after its hydrogenation (Srinivasan & Saraswathi, 2010). Some properties of graphane are listed in Table 8.1.

8.2 Preparation

The procedure followed for the preparation of graphene oxide flakes is schematically presented in Figure 8.1. The samples were prepared in collaboration with Dr. D.W. Lee. Initially, graphite powders were bought from Sigma Aldrich (product number 496596) and I followed a method which combines the Brodie and the Staudenmaier techniques (Brodie, 1859; Staudenmaier, 1898) for oxidation. A considerable amount of graphite was weighed ($\approx$ 5g) and mixed with 25 mL of nitric acid (HNO_3) and 50 mL of sulfuric acid (H_2SO_4) in a beaker. The process was carried out in a fume bench to avoid inhalation of the toxic acids. 10 g of positive catalyst potassium chlorate ($KClO_3$) was added while slowly stirring the solution with the help of a glass rod. The reaction was kept in an ice bath for some days changing the acids periodically. Graphite is black in color and it is brightened to brown or dark yellow after oxidation. After one week of reaction we observed that the solution became brown. The acids were then removed and the sample was washed three times with distilled water. The sample was then dried overnight at 70 °C (higher temperatures would decompose the material). Thus graphite oxide (GO) is obtained. To obtain the graphene oxide flakes, the GO sample was reacted with sodium hydroxide (NaOH, Sigma Aldrich No. 655104)

Table 8.1: Electrical and chemical characteristics of graphene (G), graphene oxide (GO) and graphane (Ga) reported in the literature.

Graphene (G)

Preparation	**Classification**	**Chemical bondings**	**Ambipolar?**	**Carrier mobility**	**Resistivity**
Exfolating graphite Novoselov *et al.*	Conductor or semi-metal Pierson	sp^3 Pierson	Yes	15000 $cm^2V^{-1}s^{-1}$ at RT Geim & Novoselov	$\approx 10^{-6}\Omega$cm

Graphene oxide (GO)

Preparation	**Classification**	**Functional groups**	**Chemical bondings**
Oxidating graphite Brodie; Hudson *et al.*; Hummers & Offeman; Staudenmaier	Insulator	C-(OH) Hydroxyl; C-(O)-C Epoxy, C=(O) Carbonyl (edge), (OH)-C=(O) Carboxyl (edge) Szabo *et al.*	sp^2, sp^3

Graphane (Ga)

Preparation	**Classification**	**Functional groups**	**Chemical bondings**	**Ambipolar?**	**Carrier mobility**
Cold hydrogen plasma Elias *et al.*	Insulator Elias *et al.*	(H)-C	sp^3 Srinivasan & Saraswathi	No Srinivasan & Saraswathi	14000 (at RT) and 10 $cm^2V^{-1}s^{-1}$ (at liquid He)

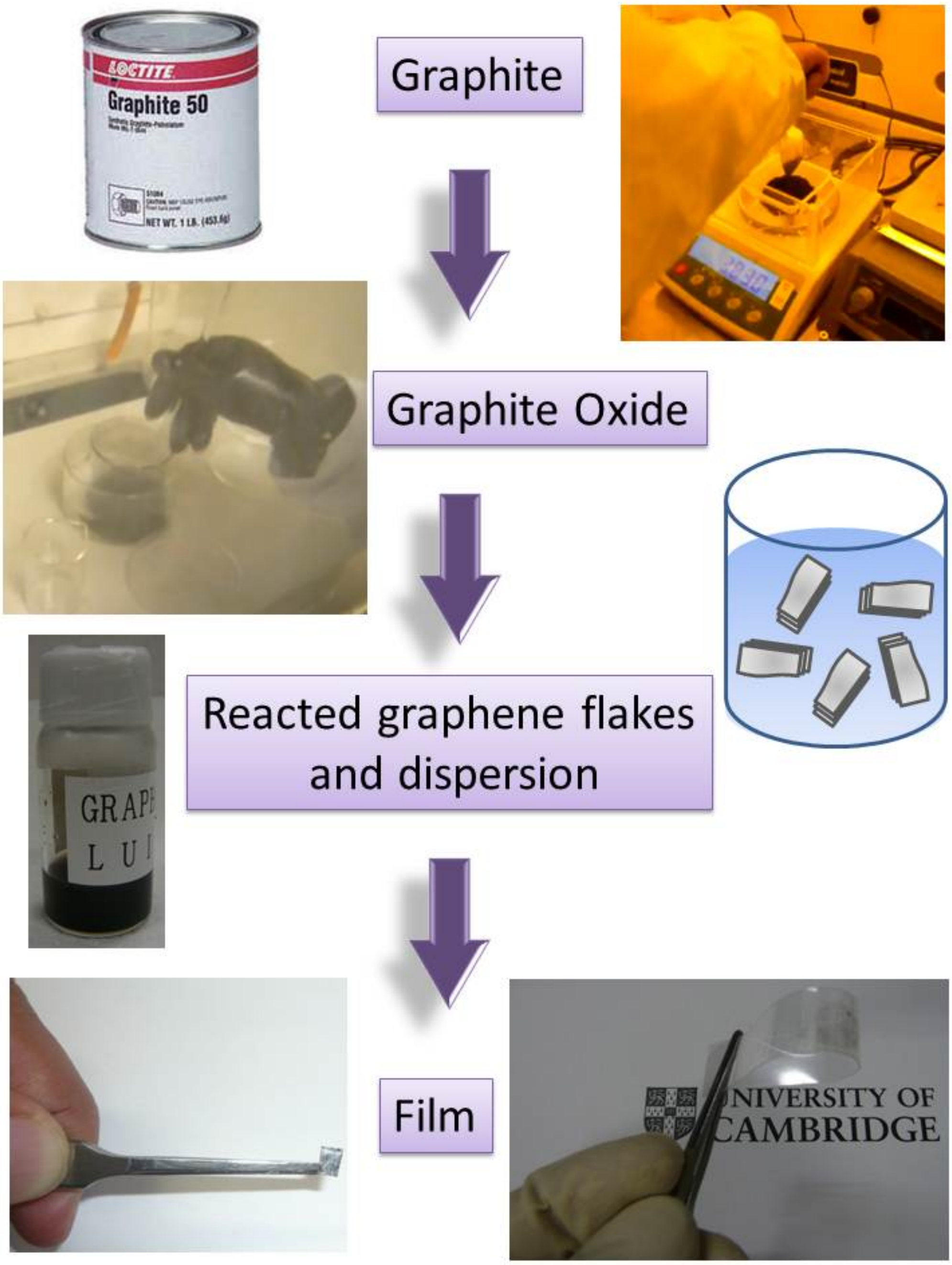

Figure 8.1: Schematic representation of the preparation of GO flakes.

diluted in water (0.5 M) for two weeks. NaOH destroys the epoxy groups of the GO as explained below and the sample turns black again. When the sample is dried the desired product is obtained. The final sample is a film consisting of graphene oxide flakes which can be easily handled or spread on a plastic substrate as shown in the figure.

8.3 Characterization by XRD

Figure 8.2 shows the XRD patterns of samples of graphite, graphite oxide (GO) and NaOH-reacted graphite oxide. Graphite shows its typical peaks at 26.82° and 54.84°. Its structure is hexagonal P63/mmc (spatial group 194) and the reflections correspond to the Miller indexes (002) and (004) respectively. Carbon atoms are arranged in the (0,0,0); (1/3,2/3,0); (0,0,1/2) and (2/3,1/3,1/2) positions of the structure as they are denoted by C1, C2, C3 and C4 respectively in the inset of the figure. As mentioned above, the carbon layers in graphite form graphene, they are not distorted and two adjacent layers are displaced by half of the c-dimension. The principal peak of the GO appears around 12.28° which corresponds to an interlayer distance of about 7.20 Å. However, a small amount of diffuse scattering is observed in the background of the diffraction. This amorphicity is explained from the functional groups epoxy (C-O-C) and hydroxyl (-OH) which are formed in the structure (Hofmann *et al.*, 1934; Lee *et al.*, 2010; Lerf *et al.*, 1998). Table 8.2 lists the full width at half maximun (FWHM), the mean crystallite diameter (D), the interlayer distance (d/2) and the average number of sheets in the mean crystallite (N). Note that following oxidation, the crystallite size, which was obtained by Scherrer's formula (see Equation 3.1 on page 38), increases, implying that the number of distorted sheets decrease. When GO reacts with NaOH, the number of reflections in the XRD pattern increases (Figure 8.2). These additional reflections indicate structural deformation which originate from the decomposition of the epoxy groups to hydroxyl and -ONa groups (the model inside the figure shows the formation of -ONa in the structure without distortion). In general, the interlayer distance increases after oxidation and with reaction with NaOH due to the functional groups formed between layers. Oxygen atoms in the GO structure have an electronegativity of 3.4417 and it is higher than for carbon, hydrogen, and sodium atoms (2.55, 2.20 and 0.93 respectively). The charges in the structure should transfer from carbon, hydrogen, and sodium atoms to oxygen atoms because charge transfer depends on electronegativity. In contrast, in the NaOH-GO structure sodium and hydrogen atoms bonded with oxygen atoms have positive charges (Na^+ and H^+), while oxygen atoms have negative charges (O^{2-}). As more hydroxyl groups and -ONa groups are produced between the layers, more charges are transferred to oxygen atoms and more charges are localized between the layers because GO is an insulator. As a result, N might increase due to the electrostatic interaction among the chemical groups.

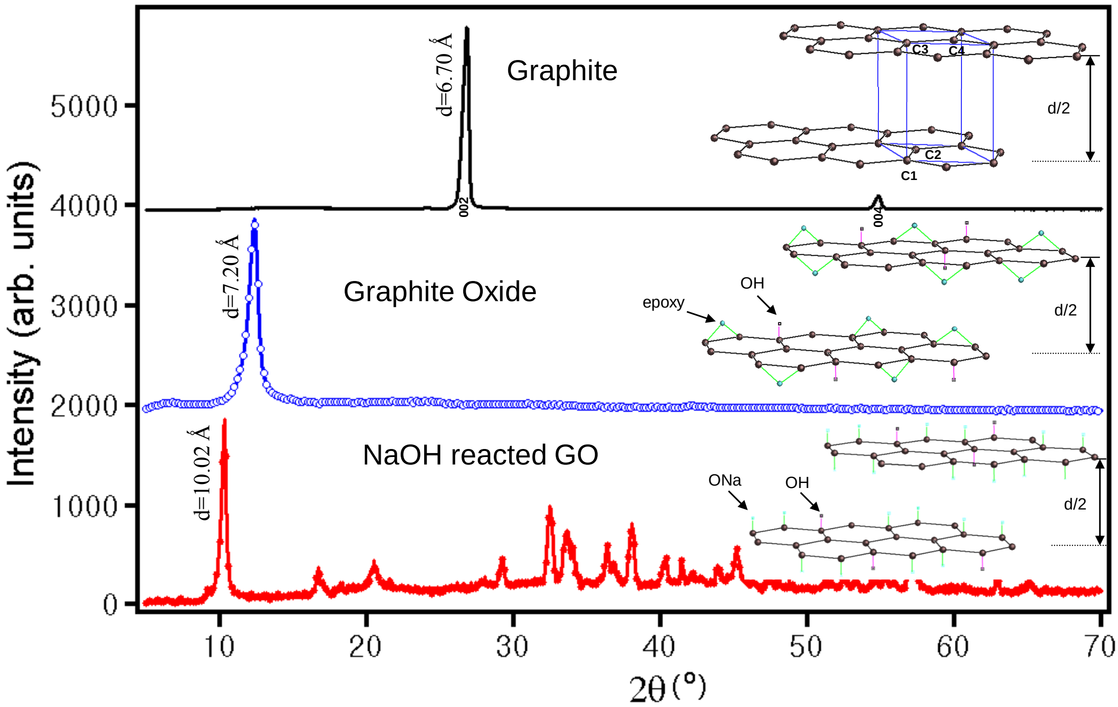

Figure 8.2: X-ray diffraction of graphite (G), graphite oxide (group of graphene oxide, GO) and NaOH-reacted graphite oxide (GO flakes).

Table 8.2: Principal characteristics obtained by XRD of the samples graphite (G), graphite oxide (GO) and NaOH- reacted graphite oxide (NaOH-flakes).

Sample	**zθmax** (°)	**FWHM**	**D(nm)**	**d/2(Å)**	**N**
Graphite	26.82	0.243	34.2	3.3	103
GO	12.31	0.493	16.5	3.6	46
NaOH-GO	10.29	0.257	31.6	4.3	74

8.4 Conclusions

A new method for the preparation of graphene oxide flakes has been achieved by oxidizing comercial graphite and reacting it with NaOH. The product consists of multiple and distorted graphene oxide flakes forming a film which can be easily deposited in flexible substrates. XRD reveals that the interlayer distance between graphene increases by oxidation due to chemical groups formation. These effects make possible the formation of delaminated flakes which can form a flexible film based of multiple graphene oxides.

Chapter 9

Conclusions and future work

9.1 Overall conclusions

Different properties of noble metal films and oxide materials have been studied for their potential use in nanotechnology. In the case of gold and copper films, annealing changes the morphology and crystallization. Gold does not oxidise and thus a high degree of crystallization in the [111] direction can be easily obtained together with changes of the surface morphology. Both slow and rapid annealing give a good background in the XRD spectra indicating clean and complete crystallization, which depends more on the temperature than on the time of annealing. Strain relaxation at high temperatures should be responsible for the initial stages of gold cluster formation. Gold island nucleation sites may be formed in disordered points on the surface such as excess point defects, dislocations, lattice strain, etc.; they become islands when the temperature and duration of annealing increase. Under annealing, gold crystallites reach a maximum mean size of around 90 nm. In contrast, copper easily oxidizes, Cu_2O and CuO were obtained following annealing Cu thin films at different temperatures. At low annealing temperatures some copper atoms bond to oxygen atoms to form Cu_2O as the first oxide phase. It is not possible to determine the exact temperature transition because oxidation occurs progressively. However, the phase transition upon increasing the annealing temperature is $Cu \rightarrow Cu + Cu_2O \rightarrow Cu_2O \rightarrow Cu_2O + CuO \rightarrow CuO$. Following the technique presented in this thesis, pure Cu_2O films are obtained at 200 °C, whereas CuO films are obtained above an annealing temperature of 300 °C. The resistivity phase diagram obtained by I-V characterization presents an anomalous decrease of the resistivity at the annealing temperature ranges 250 - 275 °C and 300 - 600 °C. Together with a hole-doping effect, this behavior in the resistivity may be related to the good crystallization and bigger crystallite sizes produced by annealing. Although oxide formation still limits the use of copper in nanoelectronics, the thermal oxidation technique described here can be used to fabricate copper oxide hetero-structures which are very useful due to their potential applications in large-area-electrical devices.

In the case of nickel, it is possible to fabricate nickel nanoelectrodes separated by a nanogap by the electroplating technique. Gaps obtained by this technique fall beyond the resolution of e-beam lithography. Careful selection of the electrochemical variables such as the electrolyte concentration, applied potential, cleaning, etc., permit the control of nanogap formation by the duration of electrodeposition. During the process, the gap width decreases exponentially with time until the electrodes come into contact. The present method offers various benefits such as extremely small gaps, high yield (≈100%) fabrication and readily available instrumentation to be applied in nanoelectronics.

Furthermore, the oxide materials studied in this thesis present properties that are also promising for use in nanoelectronics. The oxide superconductor $LaCaBaCu_3O_7$ (La1113) can be linked a Au(111) surface through self-assembled monolayers of alkane-thiols. These functional groups are adsorbed on the surface of La1113 nanoparticles without destroying their superconducting properties. The links might be mediated by the formation of copper sulfonates originated by the S atoms of the thiol heads and the Cu(1) atoms of the La1113 structure. Functionalized oxide superconductor particles can be immobilized on gold electrodes and are promising candidates to fabricate nanotransistors controlled by external magnetic fields. To compare, carboxyl ferromagnetic microspheres have been attached to gold electrodes and an external magnetic field has been applied during current-voltage measurement. It has been found that the microspheres tend to physically move in the direction of the field, producing a disturbance in the current-voltage signals.

Finally, a new method for the preparation of graphene oxide flakes has been reported by oxidizing commercial graphite and reacting it with NaOH. The product consists of multiple distorted graphene oxide flakes forming a film which can be easily deposited on flexible substrates. XRD reveals that the interlayer distance between graphene increases by oxidation due to chemical group formation. These effects allow delamination and flexibility of the NaOH-reacted GO flakes which can be eventually used in micro and nanoelectronics.

9.2 Future work

Further work is necessary to assemble the material components studied in this thesis and fabricate nanoelectronic devices such as that shown in Figure 9.1. From the study of thin metal films, it has been demonstrated that gold resists oxidation and self-assembled monolayers can be formed on its surface to attach to other structures. Thin copper films are not a good candidate for nanoelectronic device fabrication due their ease of oxidation. However, heterostructures of copper oxides are promising for use in solar cells. Like copper, nickel also oxidizes, however its magnetic properties make it attractive for use in nano-spintronic devices. Oxide superconductors and magnetic particles could be tested by placing them between the nanogap electrodes and controlling them by an external magnetic field. For instance, the superconducting or non-superconducting states of La1113 grains could be controlled by turning "on" or "off" the critical magnetic field. This would allow the current flowing to two corresponding states of block/pass (or off/on). In this way the external magnetic field could control the nano-device like a transistor gate. Taking an applied voltage (at the drain) V_D=1 and the field H = H_{C2} = 1 units, and considering the presence/absence of the resulting voltage as 1/0; the result is that if H = 0, V = 1 and vice versa; the proposed transistor will thus work as an inverter switch. Logic gates such as AND or NOR could be obtained using two of these inverters in series or in parallel respectively. Further digital circuits can be logically built by a combination of various logic gates. Finally, in the case of graphene oxide flakes, there are currently extensive research efforts in this area and the preparation technique described in this thesis, together with controlled delamination, could be used for the mass production of flexible graphene oxide devices and electronic circuits.

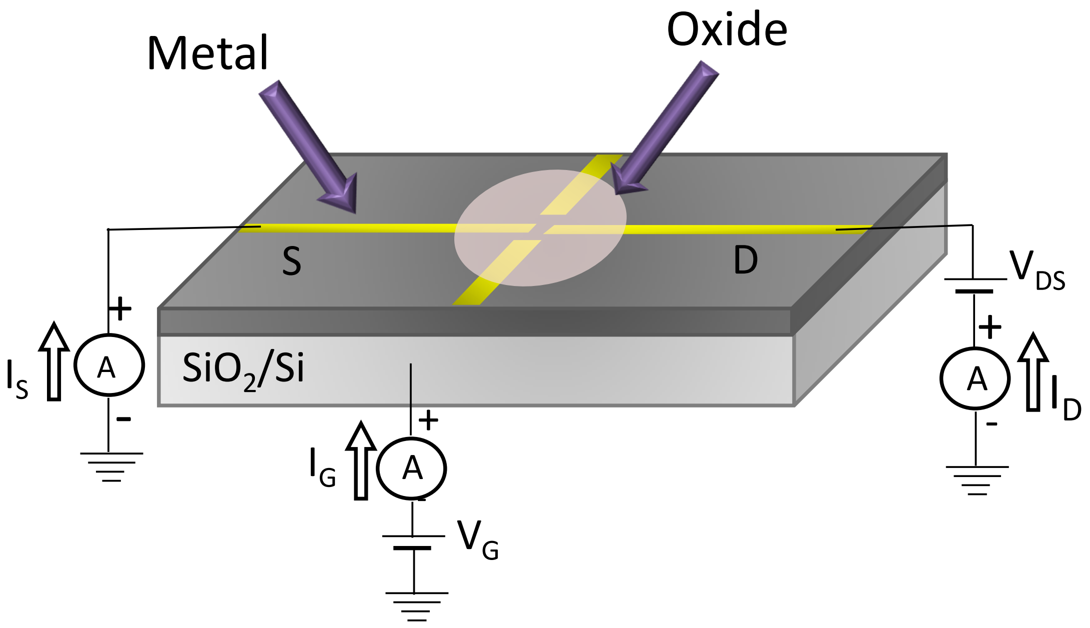

Figure 9.1: General representation of a nanoelectronic device which can be fabricated by using the different components described in this thesis.

Appendix A
Cover article and alert

During the work for this thesis, several articles have been published. Some of them have been chosen as the cover of some journals or appeared as web alerts.
For instance, in the following figures, the cover of Nanotechnology, Vol. 21, Nov 2010 and its corresponding web alert is presented.

Note : These images have been removed from this version for publisher copyright reasons.

References

Adam, S., Hwang, E., Galitski, V. & Sarma, S. (2007). *Procc. Nat. Ac. Sci. USA*, **104**, 18392–18397. 121

Akkari, F.C., Kanzari, M. & Rezig, B. (2007). *Eur. Phys. J. Appl. Phys.*, **40**, 49. 55, 57

Alharbi, F., bass, J.D., Salhi, A., Alyamani, A., Kim, H.C. & Miller, R.D. (2011). *Renewable Energy*, **36**, 2753–2758. 3

Amelinckx, S. & Dekeyser, W. (1969). *Solid State Phys.*, **8**, 476. 51

Asbrink, S. & Norrby, L. (1970). *Acta Crystallogra. B*, **26**, 8–15. 64, 65

Awana, V. & Narlokar, A. (2001). *Mod. Phys. Lett.*, **15**, 415–453. 91

Baldini, M., Struzhkin, V., Goncharov, A., Postorino, P. & Mao, W. (2011). *Phys. Rev. Lett.*, **106**, 066402. 7

Bard, A. & Faulkner, L. (2001). *Electrochemical Methods, Fundamentals and Applications*. John Wiley and Sons Inc., New York, USA. 77

Benouattas, N., Mosser, A., Raiser, D., Faerber, J. & Bouabellou, A. (2000). *App. Surf. Sci.*, **153**, 79–84. 6, 18, 54

Birnbaum, J. & Williams, R. (2000). *Phys. Today*, **53**, 38–42. 89

Bishop, H. & Riviére, J. (1969). *J. Phys. D*, **2**, 1635. 35, 47

Bogani, L. & Wernsdorfer, W. (2008). *Nature Mater.*, **7**, 179–186. 110

Bolotin, K., Kuemmeth, F., Pasupathy, A. & Ralph, D. (2004). *App. Phys. Lett.*, **84**, 3154–3156. 69

Booth, N., Fisher, P., Nahum, M. & Ullom, J.N. (1999). *Supercond. Sci. Technol.*, **12**, 538–554. 89

Boukhalov, D.W. & Katnelson, M. (2008). *J. Am. Chem. Soc.*, **130**, 10697. 122

Briggs, D. & Grant, J. (2003). *Surface analysis by Auger and X-ray photoelectron spectroscopy*. IM publications, London, UK. 99

Brodie, B. (1859). *Philos. Trans. R. Soc.*, **149**, 249. 121, 122, 123

Brück, L. (1936). *Ann. Phys. Leipzig*, **26**, 233. 35

Buchholz, S., Fuchs, H. & Rabe, J.P. (1991). *J. Vac. Sci. Technol. B*, **9**, 857. 35, 36

Caune, S., Marfaing, J. & Marine, W. (1991). *Phase Trans.*, **31**, 287–289. 34

Céspedes, O., Bari, M., Dennis, C., Versluijs, J., Jan, G., Sullivan, J., Gregg, J. & Coey, J. (2002). *J. Mag. Mag. Mat.*, **242-245**, 492–494. 70

Céspedes, O., Rocha, A., Lioret, S., Viret, M., Dennis, C., Gregg, J., van Dijken, S., Sanvito, S. & Coey, J. (2004). *J. Mag. Mag. Mat.*, **272-276**, 15711572. 85

Chang, J., Young, T., Yang, Y., Ueng, H. & Chang, T. (2004). *Mat. Chem. Phys.*, **83**, 199–203. 36, 37, 39, 47

Chen, C. & Chen, L. (1996). *App. Surf. Sci.*, **92**, 507–512. 45

Chen, D. & Li, J. (2006). *Surf. Sci. Rep.*, **61**, 445–463. 97

Chen, J.H., Jang, C., Adam, S., Fuhrer, M., Williams, E. & Ishigami, M. (2008a). *Nat. Phys.*, **4**, 377–381. 121

Chen, J.H., Jang, C., Xiao, S., Ishigami, M. & Fuhrer, M. (2008b). *Nat. Nanotech.*, **3**, 206–209. 121

Chidsey, C., Loiacono, D., Sleator, T. & Nakahara, S. (1988). *Surf. Sci.*, **200**, 45. 35

Cooper, J. (2011). Ph.D. thesis, University of Cambridge, Cavendish Laboratory. 22

Cullity, B.D. (2001). *Elements of X-ray diffraction*. Prentice-Hall International, London. 38

Cung, S., Hoffman, A., Bader, S., Liu, C., Kay, B., Makowski, L. & Chen, L. (2004). *Appl. Phys. Lett*, **95**, 2971. 32

Datta, S., Tian, W., Hong, S., Reifenberger, R., Henderson, J. & Kubiak, C. (1997). *Phys. Rev. Lett.*, **79**, 2530 – 2533. 68

Deshmukh, M., Prieto, A., Gu, Q. & Park, H. (2003). *Nano Lett.*, **3**, 1383–1385. 70, 73

Dishner, M.H., Ivey, M.M., Gorer, S., Hemminger, J.C. & Feher, F.J. (1998). *J. Vac. Sci. Technol. A*, **16**, 3295–3300. 35

Dobkin, D.M. & Zuraw, M.K. (2010). *Principles of chemical vapor deposition*. Kluwer Academic Publishers, The Netherlands. 4

Dominguez, A.B., Valladares, L.D.L.S., Willems, B., Call-Cardenas, V.B., González, J.G. & Obradors, X. (2006). *J. Phys. Chem. Solids*, **67**, 594–596. 91

Drobny, V.F. & Pulfrey, D.L. (1979). *Thin Solid Films*, **61**, 89–98. 54, 62, 64

Drung, D., Abmann, C., Beyer, J., Kirste, A., Ruede, F. & Schuring, T. (2007). *IEEE Trans. Appl. Supercond.*, **17**, 699–704. 29

Dubois, C. & Stellacci, F. (2008). *J. Phys. Chem. C*, **112**, 7431. 34

DURKAN, C. (2007). *Current at the Nanoscale: An Introduction to Nanoelectronics*. Imperial College Press, UK. 69

EASON, R. (2007). *Pulsed laser deposition of thin films: Applications-led growth of functional materials*. John wiley and Sons, Inc., New Jersey, USA. 6

EGELHOFF, W., GAN, L., ETTEDGUI, H., KADMON, Y., POWELL, C., CHEN, P., SHAPIRO, A., MCMICHAEL, R., MALLETT, J., MOFFAT, T., STILES, M. & SVEDGERG, E. (2004). *J. Appl. Phys.*, **95**, 7554–7559. 72

ELHOUSSINE, F., MÁTEFI-TEMPFLI, S., ENCINAS, A. & PIRAUX, L. (2002). *App. Phys. Lett.*, **81**, 1681–1683. 72, 73

ELIAS, D., NAIR, R., MOHIUDDIN, T., MOROZOV, S., BLAKE, P., HALSALL, M., FERRARI, A., BOUKHVALOV, D., KATSNELSON, M., GEIM, A. & NOVOSELOV, K. (2009). *Science*, **323**, 611–613. 122, 123

EMBERLY, E. & KIRCZENOW, G. (2003). *Phys. Rev. Lett.*, **91**, 188301 – 188304. 68

FANNIN, P. (1986). *J. Phys. E: Sci. Intrum.*, **19**, 238. 32

FANNIN, P. & CHARLES, S. (1999). *J. Magn. Magn. Mat.*, **196-197**, 586. 32

FANNIN, P., KINSELLA, L. & CHARLES, S. (1999). *J. Magn. Magn. Mat.*, **201**, 91–94. 32

FANNIN, P., L.COHEN-TANNOUDJI, BERTRAND, E., GIANNITSIS, A., OIREACHTAIGH, C.M. & BIBETTE, J. (2006). *J. Magn. Magn. Mat.*, **303**, 147–152. 30

FELNER, I., WOLFUS, Y., HILSCHER, G. & PILLMAYR, N. (1989). *Phys. Rev. B*, **39**, 225. 105

FERNANDO, C. & WETTHASINGHE, S. (2000). *Sol. Energy Mater. Sol. Cells*, **63**, 299. 54

FERULLO, R., GARDA, G., BELELLI, P., BRANDA, M. & CASTELLANI, N. (2006). *J. Mol. Struct. THEOCHEM*, **769**, 217–223. 6, 18, 54

Figueiredo, V., Elangovan, E., Goncalves, G., Barqunha, P., Pereira, L., Franco, N., Alves, E., Martins, R. & Fortunato, E. (2008). *Appl. Surf. Sci.*, **254**, 3949. 55, 57, 62

Figueiredo, V., Elangovan, E., Goncalves, G., Franco, N., Alves, E., Park, S., Martins, R. & Fortunato, E. (2009). *Phys. Status. Solidi A*, **9**, 2143. 55

Fujinaka, A. & Berezin, A. (1983). *J. Appl. Phys.*, **54**, 3582. 54

Gabrielson, T. (1993). *IEEE Trans. Elec. Dev.*, **40**, 903–909. 79

Gabureac, M., Viret, M., Ott, F. & Fermon, C. (2004). *Phys. Rev. B*, **69**, 100401. 72

Gao, J.W., Gong, H., He, J., Thomas, A., Chan, L. & Li, S. (2001). *Mat. Lett.*, **51**, 78–84. 57

Garcia, N., Wang, H., Cheng, H. & Nikolic, N. (2003). *IEEE Trans. Mag.*, **39**, 2776–2781. 70

Geim, A. & Novoselov, K. (2007). *Nat. Mat.*, **6**, 183–191. 123

Gibbs, D., Ocko, B., Zehner, D. & Mochire, S. (1988). *Phys. Rev. B*, **38**, 7303. 34

Golan, Y., Margulis, L. & Rubinstein, I. (1992). *Surf. Sci.*, **264**, 312–326. 35, 36

Grand, W. & Talbot, J. (1993). *J. Electrochem. Soc.*, **140**, 675–681. 74

Gunasekaran, R. & J.V. Yakhmi, R.I. (1993). *Physica C*, **208**, 143. 90

Gunasekaran, R., Gopalakrishnan, I., Sastry, P., Yakhmi, J. & Iyer, R. (1992). *Physica C*, **199**, 240. 90

Guo, Z., Hahn, H., Lin, H., Karki, A. & Young, D. (2008). *J. Appl. Phys.*, **104**, 014314. 114

Hähner, G., Kinzler, M., Thümmler, C., Wöll, C. & Gruzne, M. (1992). *J. Vac. Sci. Technol. A*, **10**, 2758. 34

Hamann, C., Hamnett, A. & Vielstich, W. (2007). *Electrochemistry*. Willey-VCH, Weinheim, Germany. 26

Hamelin, A., Sottomayor, M., Silva, F., Chang, S. & Weaver, M. (1990). *J. Electroanal. Chem.*, **295**, 291. 35

Han, J.H., Ahn, H.T., hyun Kim, T. & Jee, K.K. (2010). *Mat. Sci. Forum*, **654-656**, 2107–2110. 3

Han, K. & Tao, M. (2009a). *Sol. Energy Mater. Sol. Cells*, **93**, 153. 54

Han, K. & Tao, M. (2009b). *Sol. Energy Mater. Sol. Cells*, **93**, 153–157. 66

Hansen, C., Leung, K. & Mousavi, P. (2007). *Phys. World*, **20**, 24. 32

Harder, P., Grunze, M., Dahnit, R., Whitesides, G. & Laibibis, P. (1998). *J. Phys. Chem. B*, **102**, 426. 34

Heinze, J. (1984). *Angew. Chem. Int.*, **23**, 831–847. 77

Herrwerth, S., Rosendahl, C., Feng, J., Fick, J., Eck, W., Himmelhaus, M., Dahnit, R. & Grunze, M. (2003). *Langmuir*, **19**, 1880. 34

Ho, P. & Kwok, T. (1989). *Rep. Prog. Phys.*, **54**, 301–348. 83, 85

Hofmann, U., Frenzel, A. & E.Csalan (1934). *Liebigs Ann. Chem.*, **1**, 510. 121, 125

Horkans, J. (1979). *J. Electrochem. Soc.*, **126**, 1861–1867. 74

Hornyak, G.L., Dutta, J., Tibbals, H.F. & Rao, A.K. (2008). *Introduction to nanoscience*. Taylor and Francis Group, London, UK. 97

Hua, S. & Chopra, H. (2003). *Phys. Rev. B*, **67**, 060401. 70

Hudson, M., Hunter-Fujita, F., Pecket, J. & Smith, P. (1997). *J. Mater. Chem.*, **7**, 301. 121, 123

HUMMERS, W. & OFFEMAN, R. (1958). *J. Am. Chem. Soc.*, **80**, 1339. 121, 123

IZHIZUKA, S., KATO, S., MARUYAMA, T. & AKIMOTO, K. (2001). *Jpn. J. Appl. Phys.*, **40**, 2765. 54

JEONG, S. & AYDIL, E. (2010). *J. Vac. Sci. Technol. A*, **28**, 1338–1343. 60

JING, H., YU, Z. & LI, L. (2008). *J. Biomed. Mater. Res. Part A*, **87**, 33–37. 53

JOHNSON, M. (2007). *Nat. Nanotechn.*, **2**, 143–144. 85

KARWAS, C. & HEPEL, T. (1989). *J. Electrochem. Soc.*, **136**, 1672–1678. 74

KASHIMURA, Y., NAKASHIMA, H., FURUKAWA, K. & TORIMITSU, K. (2003). *Thin Solid Films*, **438-439**, 317–321. 70, 73, 77

KEPLEY, L., CROOKS, R. & RICCO, A. (1985). *Anal. Chem.*, **64**, 3191. 34

KERGUERIS, C., BOURGOIN, J., PALACIN, S., ESTEVE, S., URBINA, C., MAGOGA, M. & JOACHIM, C. (1999). *Phys. Rev. B*, **59**, 12505–12513. 69, 83

KERVENNIC, Y., DER ZANT, H.V., MORPURGO, A., GUREVICH, L. & KOUWENHOVEN, L. (2002). *Appl. Phys. Lett.*, **80**, 321–323. 70, 73

KERVENNIC, Y., VANMAEKELBERGH, D., KOUWENHOVEN, L. & DER ZANT, H.V. (2003). *Appl. Phys. Lett.*, **83**, 3782–3784. 70, 73

KHONDAKER, S.I. (2002). *App. Phys. Lett.*, **81**, 4613–4615. 69

KHONDAKER, S.I. (2004). *IEE. Proc. Circ. Dev. Syst.*, **151**, 457–460. 69

KIKUCHI, N. & TONOOKA, K. (2005). *Thin Solid Films*, **486**, 33–37. 64

KOFFYBERG, F. & BENKO, F. (1982). *J. Appl. Phys.*, **53**, 1173–1177. 54, 57

KOLB, D. & SCHNEIDER, J. (1985). *Surf. Sci.*, **162**, 764. 35

KOSUGI, T. & KANEKO, S. (1998). *J. Am. Ceram. Soc.*, **81**, 3117–3124. 54

Kötzitz, R., Weitschies, W., Trahms, L., Brewer, W. & Semmler, W. (1999). *J. Magn. Magn. Mat.*, **194**, 62. 32

Krabbes, G., Fuchs, G., Cander, W.R., May, H. & Palka, R. (2006). *High temperature superconductors bulk materials*. Wiley-VCH Verlag, Weinheim. 103, 105

Krans, J., van Ruitenbeek, J., Fisun, V., Yanson, I. & de Jongh, L. (1995). *Nature*, **375**, 767–769. 69

Küpfer, H., Wolf, T., Meier-Hirmer, R. & Zhukov, A. (2000). *Physica C*, **80**, 332. 105

Lee, D., Valladares, L.D.L.S., Seo, J., Felix, L.L., Dominguez, A.B., Cole, J. & Barnes, C. (2010). *J. Phys. Chem. B*, **114**, 5723–5728. 121, 125

Leeuw, D.M.D., Mutsaers, C., van Hall, H., Verweij, H., Carim, A. & Smoorenberg, H. (1988). *Physica C*, **156**, 126. 90

Lerf, A. & Buchsteiner, A. (2006). *J. Phys. Chem. Solids*, **67**, 1106. 121

Lerf, A., He, H., Foster, M. & Klinowski, J. (1998). *J. Phys. Chem. B*, **102**, 4477–4482. 125

Levinson, H.J. (2010). *Principles of Lithography*. SPIE - The international Society for Optical Engineering, Washington, USA. 12

Li, C., He, H. & Tao, J. (2000). *Appl. Phys. Lett.*, **77**, 3995–3997. 70, 83

Li, X., Yasutake, Y., Kono, K., Kanehara, M., Teranishi, T. & Majima, Y. (2009). *Jpn. J. Appl. Phys.*, **48**, 04C180. 89

Liang, W., Shores, M., Bockrath, M., Long, J. & Park, H. (2002). *Nature*, **417**, 725–729. 69

Lichtman, D., Craig, J., Sailer, V. & Drinkwine, M. (1981). *Appl. Surf. Sci.*, **7**, 325–331. 99

Liew, Y. & Wang, G. (1990). *Surf. Sci.*, **227**, 190. 34

Long, D., Patterson, C., Moore, M., Seferos, D., Bazan, G. & kushmerick, J. (2005). *Appl. Phys. Lett.*, **86**, 153105. 110

Love, J.C., Estroff, L.A., Kriebel, J.K., Nuzzo, R.G. & Whitesides, G.M. (2005). *Chem. Rev.*, **105**, 1103–1169. 97

Lynch, D.W. & Olson, C. (1999). *Photoemission studies of high-temperature superconductors*. Cambridge University Press, UK. 99

Ma, Z. & Allen, L. (1993). *Phys. Rev. B*, **48**, 15484. 36

Mahadevan, M. & Bradley, R. (1999). *Phys. Rev. B*, **59**, 11037. 69

Mahadevan, M. & Bradley, R. (2000). *Nature*, **407**, 57–60. 69

Mahapatro, A.K., Ghosh, S. & Janes, D. (2006). *IEEE Trans. Nanotech.*, **5**, 232–236. 79

Mallett, J., Svedberg, E., Ettedgui, H., Moffat, T. & Egelhoff, W. (2004). *Phys. Rev. B*, **70**, 172406. 72

Mancini, N. & Rimini, E. (1970). *Surf. Sci.*, **22**, 357–364. 34, 36, 48, 50

Marabelli, F., Parraviciny, G. & Drioli, F. (1995). *Phys. Rev. B*, **52**, 1433. 54

Marchal, G., Mangin, P. & Janot, C. (1980). *Phil. Mag. B*, **42**, 81. 36

Massalski, T.B. (1987). *Binary Phase Diagrams*. American Society for Metals, Ohio. 36

Mathieu, G., Contini, R., Layet, J., Mathiez, P. & Giorgio, S. (1988). *J. Vac. Sci. Techn. A*, **6**, 2904. 35

Mikoushkin, V., Mamutin, V., Sysoev, S., Shnitov, V. & Gordeev, Y. (2003). *Microelec. Eng.*, **69**, 480–484. 89

Mimani, T., Mayanna, S. & Munichandraiah, N. (1993). *J. App. Electrochem.*, **23**, 339–345. 76, 77

Mimani, T., Tanaka, H., Shimakawa, T., Miyata, T. & Sato, H. (2004). *Jpn. J. Appl. Phys.*, **43**, L917–L919. 65

Mirkin, C., Chen, K., Piner, R., Xu, F., Ritchie, J., McDevitt, J., Cannon, M. & Kanis, D. (1998). *Langmuir*, **14**, 6505–6511. 90

Mirkin, C.A., Xu, F. & Zhu, J. (1997). *Adv. Matter.*, **9**, 167–173. 90

Mittiga, A., Salza, E., Sarto, F., Tucci, M. & Vasanthi, R. (2006). *Appl. Phys. Lett.*, **88**, 163502. 65

Moore, G. (1965). *Electronics*, **38**, 114–117. 1, 89, 109

Morán, O., Hott, R., Schneider, R., Wühl, H. & Halbritter, J. (2003). *J. Appl. Phys.*, **94**, 6667–6672. 89

Moreland, J. & Ekin, J. (1985). *J. App. Phys.*, **58**, 3888 – 3895. 69

Morozov, S., Novoselov, K., Katsnelson, M., Schedin, F., Elias, D., Jaszczak, J. & Geim, A. (2008). *Phys. Rev. Lett.*, **100**, 016602. 121

Morpugo, A., Marcus, C. & Robinson, D. (1999). *App. Phys. Lett.*, **74**, 2084–2086. 70, 73

Mukhopadhyay, A., Chakraborty, A., Chatterjee, A. & Lahiri, S. (1992). *Thin Solid Films*, **209**, 92. 54

Muller, C., Krans, J., Todorv, T. & Reed, M. (1996). *Phys. Rev. B*, **53**, 1022–1025. 69

Müller, K., Takashige, M. & Bednorz, J. (1987). *Phys. Rev. Lett.*, **58**, 1143. 105

Musa, A., Akomolafe, T. & Carter, M. (1998). *Sol. Energy Mat. Sol. Cells*, **51**, 305–316. 61

Muthe, K., Vyas, J., Narang, S., Aswal, D., Gupta, S., Pinto, R., Kothiyal, G. & Sabharwal, S. (1998). *Thin Solids Films*, **324**, 37–43. 54

Nagao, K., Neaton, J. & Ashcroft, N. (2003). *Phys. Rev. B*, **68**, 125403. 54

Natelson, D. (2009). *Phys. World*, **22**, 27–31. 89

Neumann, J., Zhong, T. & Chang, Y. (1984). *Bull. Alloy Phase Diagrams*, **5**, 136–140. 54, 57

Novoselov, K., Geim, A., Morozov, S., Jiang, D., Zhang, Y., Dubonos, S., Grigorieva, I. & Firsov, A. (2004). *Science*, **306**, 666–669. 123

Novoselov, K., Geim, A., Morozov, S., Jiang, D., Katsnelson, M., Grigorieva, I., Dubonos, S. & Firsov, A. (2005). *Nature*, **438**, 197–200. 121

Nuzzo, R., Korenic, E. & Dubois, L. (1989). *J. Chem. Phys.*, **93**, 767. 34

Ocko, B., Wang, J., Davenport, A. & Issac, H. (1990). *Phys. Rev. Lett.*, **65**, 1466. 34

Ogale, S., Bilurkar, P., Mate, N., Kanetkar, S., Parikh, N. & Patnaik, B. (1992). *J. App. Phys.*, **72**, 3765. 54

Olsen, L., Addis, F. & Miller, W. (1982-1983). *Solar Cells*, **7**, 247–279. 64

Ozatay, O., Chalsani, P., Emley, N., Krivorotov, I. & Burhman, R. (2004). *J. App. Phys.*, **95**, 7315–7317. 72

Palfreyman, J. (2009). *Fabrication and Functionalisation of Multibit Magnetic Tags*. Ph.D. thesis, University of Cambridge, Cavendish Laboratory, Department of Physics. 22

Park, H., Lim, A., Alivisatos, A., Park, J. & McEuen, P. (1999). *App. Phys. Lett.*, **75**, 301–303. 69, 70

Park, J., Pasupathy, A., Goldsmith, J., Chang, C., Yaish, Y., Petta, J., Rinkoski, M., Sethna, J., Abruna, H., McEuen, P. & Ralph, D. (2002). *Nature*, **417**, 722–725. 70

Parkin, S. (1995). *Annu. Rev. Mater. Sci.*, **25**, 357–388. 114

Parks, J., Champagne, A., Hutchison, G., S. Flores-Torres, H.A. & Ralph, D. (2007). *Phys. Rev. Lett.*, **99**, 026601. 69

Pashley, D. (1956). *Adv. Phys.*, **5**, 173. 35, 39

Pearton, S., Heo, W., Ivill, M., Norton, D. & Steiner, T. (2004). *Semicond. Sci. Technol.*, **19**, R59. 54

Peng, J., Klavis, P., Shelton, R., Radousky, H., Hahn, P., Bernardez, L. & Costantino, M. (1989). *Phys. Rev. B*, **39**, 9074. 90

Peng, T., Shen, K., Wu, H. & Liu, C. (2010). *J. Phys. D: Appl. Phys.*, **43**, 315101 (4pp). 65

Pierson, H.O. (1993). *Handbook of carbon, graphite, diamonds and fullerenes: Properties, processing and applications*. Noyes Publications, New Jersey, USA. 123

Poole, C., Farach, H., Creswick, R. & Prozorov, R. (2007). *Superconductivity*. Academic Press, New York, USA. 7, 100, 103

Popescu-Pogrion, N., Johnson, J., Wouters, D., Norga, G. & der Biest, O.V. (2004). *J. Optoelect. Adv. Mat.*, **6**, 1055–1058. 7

Popov, B., Tin, K.M. & White, R. (1993). *J. Electrochem. Soc.*, **140**, 1321–1330. 74

Prieto-Astalan, A., Ahrentop, F., Johanson, C., Larson, K. & Krozer, A. (2004). *Biosens. Bioelecron.*, **19**, 945. 32

Rajvir, S. (1997). *Phys. Rev. B*, **55**, 1216–1222. 91

Ramírez-Ortíz, J., Ogurab, T., Medina-Valtierra, J., Acosta-Ortíz, S., Bosch, P., de los Reyes, J. & Lara, V. (2001). *Appl. Surf. Sci.*, **174**, 177–184. 54

R.Castanet, Chastel, R. & Bergman, C. (1978). *Mat. Sci. Eng.*, **32**, 93. 36

Reed, M. & Tour, J. (2000). *Sci. Am.*, **282**, 86–96. 89

Reed, M., Zhou, C., Muller, C., T.P, T.B. & Tour, J. (1997). *Science*, **278**, 252–254. 69

Reichert, J., Ochs, R., Beckmann, D., Weber, H., Mayor, M. & Löhneysen, H. (2002). *Phys. Rev. Lett.*, **88**, 176804. 83

Roch, N., Vincent, R., Elste, F., Harneit, W., Wernsdorfer, W., Timm, C. & Balestro, F. (2011). *Phys. Rev. B*, **83**, 081407. 110

Ron, H., Cohen, H., Matlis, S., Rapparport, M. & Rubinstein, I. (1998). *J. Phys. Chem. B*, **102**, 9861. 100

Roos, A., Chibuye, T. & Karlson, B. (1983). *Sol. Energy Mater.*, **7**, 453–465. 54

Ross, P. (2003). *IEEE Spectrum*, **40**, 30–35. 1

Ruitenbeek, J.V., Allvarez, A., Pineyro, I., Grahmann, C., Joyez, P., Devoret, M., Esteve, E. & Urbina, C. (1996). *Rev. Sci. Inst.*, **67**, 108–111. 69

Rundqvist, J., Hoh, J. & Haviland, D. (2005). *Langmuir*, **21**, 2981. 34

Rundqvist, J., Hoh, J.H. & Haviland, D.B. (2006). *J. Coll. Interf. Sci.*, **301**, 337–341. 51

Rupp, K. & Selberherr, S. (2011). *IEEE Trans. Semicond. Manufac.*, **24**, 1–4. xiii, 2

Sahoo, S., Yang, C.S. & Doudin, B. (2006). *Phys. Lett. A*, **352**, 331–334. 70, 73

Sakka, S. (2010). *Sol-Gel science and technology: Topics in fundamental research and applications*. Kluwer Academic Publishers, The Netherlands. 4

Salmeron, M., Kaufman, D., Marchon, B. & Ferrer, S. (1987). *Appl. Surf. Sci.*, **28**, 279. 35, 36

Savchenke, A. (2009). *Science*, **323**, 589–590. 122

Schedin, F., Geim, A., Morozov, S., Hill, E., Blake, P., Katsnelson, M. & Novoselov, K. (2007). *Nat. Mat.*, **6**, 652–655. 121

Scheibe, H., Gorbunov, A., Baranova, G., Klanssen, N., Konov, V., Kulanov, M., Pompe, W., Prokhorov, A. & Weiis, H. (1990). *Thin Sld. Films*, **189**, 283. 34

Schlesinger, M. & Paunovic, M. (2010). *Modern Electroplating*. John Wiley and Sons Inc., New York, USA. 4, 21

Schramm, L., Behr, G. & W. Löser, K.W. (2005). *J. Phase Equi. Diff.*, **26**, 605–612. 54

Sekar, K., Saytam, P., Kuri, G., Mahapatra, D. & Dev, B. (1992). *Dev, Nucl. Instrum. Methods Phys. Res. Sect. B*, **71**, 308. 39

Sekar, K., Saytam, P., Kuri, G., Mahapatra, D. & Dev, B. (1993). *Dev, Nucl. Instrum. Methods Phys. Res. Sect. B*, **73**, 63. 39

Sellmann, R., Fritzsche, H. & Maletta, H. (2001). *Surf. Sci.*, **495**, 185–194. 34

Shen, J. & Raj, R. (2011). *J. Power Sources*, **196**, 5945–5950. 3

Shipway, A., Katz, E. & Willner, I. (2000). *Chem. Phys. Chem.*, **1**, 15–52. 89

Shu, C., Li, C., He, H., Bogozi, A., Bunch, J. & Tao, N. (2000). *Phys. Rev. Lett.*, **84**, 5196–5199. 70

Simmons, J. (1963). *J. Appl. Phys.*, **34**, 1793–1803. 83

Smit, R., Noat, Y., Untiedt, C., Lang, N., van Hemert, M. & van Ruitenbeek, J. (2002). *Nature*, **419**, 906–909. 69

Smith, D.L. (1995). *Thin-film deposition: Principles and practise*. McGraw-Hill, USA. 3, 5

Sokolov, A., Zhang, C., Tsymbal, E., Redepenning, J. & Doudin, B. (2007). *Nat. Nanotech.*, **2**, 171–175. 70, 73, 85

Srinivasan, C. & Saraswathi, R. (2010). *Current Science*, **97**, 302–303. 122, 123

Staudenmaier, L. (1898). *Ber. Dtsch. Chem. Ges*, **31**, 1481. 121, 122, 123

Sung, M.M. & Kim, Y. (2001). *Bull. Korean Chem. Soc.*, **22**, 748–752. 99, 100

Svedberg, E.B., Mallett, J., Ettedgui, H., Gan, L., Chen, P., Shapiro, A., Moffat, T. & Egelhoff, W. (2004). *App. Phys. Lett.*, **84**, 236–238. 72

Szabo, T., Berkesi, O., Forgo, P., Josepovits, K., Sanakis, Y., Petridis, D. & Dekany, I. (2006). *Chem. Mater.*, **18**, 2740. 123

Taychatanapat, T., Bolotin, K., Kuemmeth, F. & Ralph, D. (2007). *Nano Lett.*, **7**, 652–656. 69

Telieps, W., Mundschau, M. & Bauer, E. (1990). *Surf. Sci.*, **225**, 87. 34

Thomas, Y. & Jones, B. (1995). *Electromechanics of particles*. Cambridge University Press, Cambridge, UK. 30, 31

Tilak, B., Gendron, A. & Mosoiu, M. (1977). *J. App. Electrochem.*, **7**, 495–500. 74

Trouwborts, M., van der Molen, S. & van Wees, J. (2006). *J. App. Phys.*, **99**, 114316. 79

Tsaur, B. & Mayer, J. (1981). *Phil. Mag. A*, **43**, 345. 36

Tu, K. (2003). *J. Appl. Phys.*, **94**, 5451–5473. 83

Ulman, A. (1996). *Chem. Rev.*, **96**, 1533. 34, 110, 112

Ulman, A., Eilers, J.E. & Tillman, N. (1989). *Langmuir*, **5**, 1147. 34

Valiokas, R., Svedhem, S., Svensson, S. & Liedberg, B. (1999). *Langmuir*, **15**, 3390. 34

Valiokas, R., Östblon, M., Svedhem, S., Svensson, S. & Liedberg, B. (2000). *J. Phys. Chem. B*, **104**, 7565. 34

Valladares, L.D.L.S., Dominguez, A.B., nez, J.F.S. & Gonzalez, J.C.G. (2004). *Physica C*, **408-410**, 44–45. 91, 93

Valladares, L.D.L.S., Dominguez, A.B., Gonzalez, J.C.G., nez, J.F.S. & Obradors, X. (2006). *J. Phys. Chem. Sld.*, **67**, 605–609. 91, 93

Valladares, L.D.L.S., Lee, D., Seo, J., Felix, L.L., Dominguez, A.B., suzuki, S., Majima, Y., Mitrelias, T., Ionescu, A. & Barnes, C. (2009a). *Surf. Sci.*, **603**, 2978–2985. 55, 95

Valladares, L.D.L.S., Llandro, J., Lee, D., Mitrelias, T., Palfreyman, J., Hayward, T., Cooper, J., Bland, J., Barnes, C., Arroyo, J. & Lees, M. (2009b). *J. Magn. Magn. Mat.*, **321**, 2129–2134. 111, 116

Valladares, L.D.L.S., Dominguez, A.B., Felix, L.L., Mitrelias, T., Ionescu, A., Marcatoma, J.Q. & Barnes, C.H.W. (2010a). *J. Mat. Sci. Eng.*, **4**, 1–10. 39, 45, 47, 51, 55, 95

Valladares, L.D.L.S., Dominguez, A.B., Gonzalez, J.G., Levano, J.F., Anaya, A.O., Mitrelias, T., Majima, Y. & Barnes, C. (2010b). *Open Supercond. J.*, **2**, 19–27. 90, 91, 93, 103, 105

Valladares, L.D.L.S., Dominguez, A.B., Llandro, J., Suzuki, S., Mitrelias, T., Quispe, R.B., Barnes, C. & Majima, Y. (2010c). *Jpn. J. Appl. Phys.*, **49**, 093102. 90, 110

Valladares, L.D.L.S., Felix, L.L., Dominguez, A.B., Mitrelias, T., Sfigakis, F., Khondaker, S., Barnes, C. & Majima, Y. (2010d). *Nanotechnology*, **21**, 445304. 85

VANCEA, J., REISS, G., SCHNIEDER, F., BAUER, K. & HOFFMAN, H. (1989). *Surf. Sci.*, **218**, 108. 35

VANDERAH, D., PHARM, C., SPRINGER, S., SILIN, V. & MEUSE, C. (2000). *Langmuir*, **16**, 6527. 34

VERICAT, C., VELA, M., BENITEZ, G., GAGO, J.M., TORRELLES, X. & SALVAREZZA, R. (2006). *J. Phys.: Condens. Matter*, **18**, R867–900. 97

VON ALLMEN, M., LAU, S., MAENPAA, M. & TSAUR, B. (1980). *Appl. Phys. Lett.*, **36**, 205. 36

WAGNER, C. (1979). *Handbook of X-ray Phoelectron spectroscopy, a reference book of standard data for use in X-ray photoelectron spectroscopy*. Perkin-Elmer Corporation, Physical Electronics Division, USA. 99

WAINTAL, X. & BROUWER, P. (2003). *Phys. Rev. Lett.*, **91**, 247201. 118

WANG, L. & TAO, M. (2007). *Electrochem. Solid State Lett.*, **10**, H248. 54

WANG, S. (1994). *Mater. Res. Soc. Bull.*, **19**, 30. 54

WASA, K., KITABATAKE, M. & ADACHI, H. (2004). *Thin film materials technology: Sputtering of compound materials*. Springer-Verlag GmbH, Germany. 6

WEAVER, J., MEYER, H., WAGNENER, T.J., HILL, D., GAO, Y., PETERSON, D., FISK, Z. & ARKO, A. (1988). *Phys. Rev. B*, **38**, 4668. 98

WEI, Z., WANG, D., KIM, S., KIM, S.Y., HU, Y., YAKES, M.K., LARACUENTE, A.R., DAI, Z., MARDER, S.R., BERGER, C., KING, W.P., DE HEER, W.A., SHEEHAN, P.E. & RIEDO, E. (2010). *Science*, **11**, 1373–1376. 7

WILLIS, B. & LANG, D. (2004). *Thin Solids Films*, **467**, 284–293. 54

WINKELMANN, C., ROCH, N., WERNSDORFER, W. & BOUCHIAT, V. (2009). *Nat. Phys.*, **5**, 876–879. 89

Wold, D. & Frisbie, C. (2001). *J. Am. Chem. Soc.*, **123**, 5549 – 5556. 68

Wu, Y., Chang, D., Kim, D. & Kwon, S.C. (2003). *Surf. Coat. Tech.*, **173**, 259–264. 74

Xu, X., He, J.W. & Goodman, D.W. (1993). *Surf. Sci.*, **284**, 103–108. 6, 18, 54

Yagi, T., Domon, M., Okajima, Y. & Yamaya, K. (1991). *Physica C*, **173**, 453. 90

Yamaya, K., Yagi, T. & Okajima, Y. (1993). *Solid State Commun.*, **87**, 1113. 91

Yang, C.S., Thiltges, J., Doudin, B. & Johnson, M. (2002). *J. Phys.: Cond. Mat.*, **14**, L765–L771. 70, 72, 73

Yasutake, Y., Shi, Z., Okazaki, T., Shinohara, H. & Majima, Y. (2005). *Nano Lett.*, **5**, 1057–1060. 110

Yeshurun, Y. & Malozemoff, A. (1988). *Phys. Rev. Lett.*, **60**, 2202. 105

Yeshurun, Y., Felner, I. & Sompolinsky, H. (1987). *Phys. Rev. B*, **36**, 840. 105

Zei, M., Lehmpfuhl, G. & Kolb, D. (1989). *Surf. Sci.*, **221**, 23. 34

Zheng, X., Xu, C., Tanaka, E., Tomokiyo, Y., Susuki, M. & Otabe, E. (2001). *Physica C*, **357-360**, 181–185. 54

Zhou, C., Muller, C., Deshpande, M., Sleight, J. & Reed, M. (1995). *App. Phys. Lett.*, **67**, 1160. 69

Zhu, J., Mirkin, C., Braun, R. & Winograd, N. (1998). *J. Am. Chem. Soc.*, **120**, 5126–5127. 90

Zhuze, V. & Kurchatov, B. (1932). *Physik. Z. Sowjetunion*, **2**, 453–467. 64

Zolk, M., Eister, F., Pipper, J., Herrwerth, S., Eck, W., Buck, M. & Grunze, M. (2000). *Langmuir*, **16**, 5849. 34

Zyazin, A.S., van den Berg, J., Osorio, E., van der Zant, H., Konstantinidis, N., Leijnse, M., Wegewijs, M., May, F., Hofstetter, W., Danieli, C. & Cornia, A. (2010). *Nano Lett.*, **10**, 3307. 110